Dissertation

submitted to the

Combined Faculties for the Natural Sciences and for Mathematics

of the Ruperto-Carola University of Heidelberg, Germany

for the degree of

Doctor of Natural Sciences

Put forward by

Master of Science: Bagmeet Behera

born in: Rourkela, India

Oral examination: 9th February, 2010

Effects of EBL extinction
on the VHE spectra of blazars

Referees: Prof. Dr. Stefan J. Wagner

                       Prof. Dr. Werner Hofmann

Abstract

Active Galactic Nuclei (AGN) are the most powerful steady sources of electromagnetic radiation in the cosmos. Blazars are AGN with their jets pointing straight at us, giving us the opportunity to probe deep into the core which generates this tremendous luminosity. The Very High Energy (VHE; $E > 100\,GeV$) photons from blazars while travelling through the intergalactic medium, interact with the low energy photons (in the UV-IR range) constituting the Extragalactic Background Light (EBL), by producing $e^- e^+$ pairs, and get absorbed. More than 25 nearby blazars ($z < 0.3$) have been detected in VHE, but due to EBL extinction it is extremely difficult to detect distant sources. This phenomena gives us the means to measure the EBL level which cannot be directly measured. In this thesis the effects of EBL absorption on the spectra of blazars is studied. Two methods to discover distant VHE blazars were explored. The observations with HESS led to the detection of the blazar PKS 1510-089 at $z = 0.36$, at a 4.8σ level. A cross check analysis with a more advanced analysis tool confirmed this detection at a 8.5σ level. The GeV spectrum obtained by analyzing Fermi GST data, was adopted as the intrinsic source spectrum. Models for the γ-ray spectrum including the EBL absorption was fitted to the γ-ray data and it was shown that all the 4 current EBL models considered here, fit the data well. It is concluded that this is due to the sensitivity limits of the current VHE instruments. Stronger constraints on the EBL would only be possible for sources with much harder spectrum. The outlook for future experiments is discussed.

EBL extinction causes bias in the sample of detected blazars. MonteCarlo simulations were used to generate parent samples for the VHE blazars. These were compared to the true VHE blazar sample and constraints on the parent sample properties were drawn. The lack of a spectral softening with z in the true VHE sample, is found consistent with a parent sample that clearly shows this softening, making it unnecessary to assume any special dependence of the intrinsic spectral index on z. The dependence of the evolution of the EBL on the cosmological model considered, was explored. The uncertainty in cosmology was found to be negligible compared to the uncertainty on the EBL. The dependence of the extinction on the error in the EBL models as well as the effect of neglecting the EBL evolution with z was illustrated.

Kurzfassung

Aktive Galaktisch Kerne (active galactic nuclei, AGN) sind die leistungsstärksten dauerhaft emittierenden Quellen elektromagnetischer Strahlung im Kosmos. Blazare sind AGNs deren Jets direkt auf uns zeigen, ermöglichen uns, mit unseren Untersuchungen tief in den Kern, der diese gewaltige Leuchtkraft erzugt, vorzudringen. Die emittierten hochenergetischen Photonen aus dem VHE-Regime (very high energy, VHE; $E > 100\,GEV$) wechselwirken bei ihrer Reise duch das interstellare Medium mit niederenergetischen (im Bereich UV IR) Photonen , die den extragalaktischen Hintergrund (extragalactic background light, EBL) bilden. Debei erzeigen Sie $e^- e^+$ Paare, und werden absorbiert. Mehr als 25 nahe Blazare ($z < 0.3$) wurden im VHE-Regime detektiert, aber wegen der EBL-Extinktion ist die Detektion weit entfernter Quellen extrem schwierig. Dieses Phänomen gibt uns die Möglichkeit, die Intensität des EBL zu messen, was auf direktem Wege nicht möglich ist. In dieser Arbeit werden die Auswirkungen der EBL Absorption auf die Spektren von Blazaren untersucht. Zwei Methoden zum Entdecken ferner Balzare wurden erforscht. Die Beobachtungen mit HESS führten zum Nachweis des Blazars PKS 1510-089 mit $z = 0.36$ und einer Konfidenzlevel von 4.8σ. Die Gegenprobe mit einer ausgefeilteren Analysemethode bestätigte die Detektion mit einem Level von 8.5σ. Für das intrinsische Spektrum der Quelle wurde das mit einer Analyse von Fermi GST Daten gewonnene GeV-Spektrum angenommen. Modelle für das Gammastrahlenspektrum inklusive der EBL Absorption wurden an die Daten gefittet und es wird gezeigt, daß alle vier EBL Modelle, die hier bercksichtigt wurden, gut zu den Daten passen. Es wird geschlossen, daß dies in der limitierten Empfindlichkeit der gegenwärtigen VHE Instrumente begründet ist. Strengere Bedingungen könnte man nur von Quellen mit viel härterem Spektrum ableiten. Die Aussichten für zukünftige Experimente werden diskutiert. EBL Extinktion verfälscht die Auswahl der gefundenen Blazare. Mögliche Elternverteilungen der VHE Blazare wurden mit Monte Carlo Simulationen generiert; diese wurden mit den echten Blazaren verglichen und daraus Rückschlüsse auf die Eigenschaften der echten Verteilung gezogen. Das Fehlen von spektralem weicher werden mit z zeigt sich konsistent mit einer Elternverteilung die dieses weicher werden deutlich zeigt; es ist nicht nötig, eine spezielle Abhängigkeit des intrischen spektralen Index von z anzunehmen. Weiterhin wurde die Abhängigkeit der Entwicklung des EBL vom kosmologischen Modell untersucht. Es stellte sich heraus, daß im Vergleich zur Unsicherheit des EBL die des kosmologischen Modells vernachlässigt werden kann. Die Auswirkungen der Extinktion auf den Fehler in den EBL Modellen so wie der Effekt durch das Nichtberücksichtigen der Entwicklung des EBL mit z werden illustriert.

Contents

6   Effects of EBL extinction   79

IV   107

7   Summary and Outlook   109

A   HESS *runs* on PKS 1510-089 and 3C 279   117

B   Hillas parameters and shape-cuts   121

Bibliography   132

List of Figures

List of Tables

Part I

Motivation and outline

1.1 Motivation and aims

Blazars are a subclass of AGN, that have their jets aligned along our line of sight. These are unique objects providing a direct view into the central engines of AGN. The central engines are thought to be accreting black-holes, which act as accelerators of very high energy particles and emit the highest energy photons in nature. The emission mechanism of Very High Energy (VHE; defined as $E_\gamma > 100\,\text{GeV}$) γ-rays is not clearly understood, as the intrinsic spectra[1] cannot be directly measured. The observed VHE spectra of blazars, is the convolution of the intrinsic blazar spectra and the absorption-imprint of the inter-galactic extinction. Intergalactic extinction happens due to photon-photon pair production interactions of the VHE γ-rays and the Extragalactic Background Light (EBL) in the optical to infrared frequencies. Therefore a clear understanding of the blazar VHE emission requires untangling the effect of EBL absorption. Since this extinction is a function of the source distance and γ-ray energy, measuring its effect necessitates VHE spectral measurements of a number of blazars over a range of redshifts. The current blazar sample is only a few tens of sources and the most distant, persistent VHE source (as of October, 2009) with a secure redshift is the BL Lac object 1ES 1011+496 which has z=0.212[2].

On the other hand measuring the EBL in the optical to infrared wavelength is the key to a solve a completely different astronomical puzzle. As the EBL is the integrated starlight from the very first stars till the present epoch, it contains the imprint of the structure formation and galaxy evolution over the entire history of the universe. Measuring the EBL extinction of VHE sources at various redshifts is thus an indirect way of measuring the redshift evolution of the EBL photon density, and hence tracing the star formation history of the universe.

The measurement of EBL extinction is not a straightforward exercise since the EBL density is not known precisely. The strong foreground from the zodiacal light excludes

---

[1] Here, intrinsic spectra refers to the photons escaping the emission region, subsequent to any internal absorption in the emission region that might occur due to the local photon fields.

[2] In November, 2009 the discovery of two new sources were announced - 1ES 0502+675, with z=0.341(Ong & the VERITAS Collaboration 2009a), and 1ES 0414+009 with z=0.287 (Hofmann, W. on behalf of the HESS collaboration & Fegan, S. on behalf of the Fermi-LAT collaboration 2009). 3C 279 has a z=0.536, however it is not a persistent VHE source, and was detected only during a single night period in 2006 (Teshima *et al.* 2007; Albert *et al.* 2008).

this possibility at present. The approach one can then follow is to constrain the intrinsic VHE blazar spectra via multiwavelength observations of VHE blazars, and to estimate the EBL extinction for a range of redshifts. Comparing the EBL photon density estimated from the extinction to theoretical EBL models and getting convergence between these can then solve this problem.

The major goals of this thesis were -
(1) To device strategies to discover distant VHE-blazars at the same time constrain their intrinsic VHE spectrum,
(2) To use the measured γ-ray (GeV-TeV) spectrum to constrain EBL models, and
(3) To quantify the effect of EBL extinction on the observed spectra of individual sources, as well as on the observables of a sample of blazars.

1.2 Outline of the thesis

After giving this statement of motivation behind this work, chapter 2 summarizes the observational aspects of blazars and the relevant non-thermal emission mechanisms in these sources, section 2.1. Section 2.2 of this chapter gives the status of EBL measurements as well as the various observational and theoretical EBL models. Followed by section 2.3, an introduction to the High Energy Stereoscopic System, an array of imaging Cherenkov telescope, used for obtaining the VHE observations for this work. It concludes by laying out the details of the calculation of the optical depth encountered by VHE γ-rays due to the interaction with the EBL photon field in section 2.4. This is described in detail, since it is used at multiple instances throughout this work.

Chapter 3 and 4 report on two methods used during the course of this work to detect new VHE sources by using flares in the optical and GeV energies respectively, to trigger VHE observations with HESS. These methods also provided interesting scientific results on multiwavelength correlation studies in blazars, and estimates for the redshift of VHE blazars. These are reported here as well.

Chapter 5 reports on the HESS observations of two blazars, PKS 1510-089 and 3C 279, triggered from flares at lower energies. A VHE spectrum is obtained for PKS 1510-089, a quasar at redshift of 0.36. The MeV-GeV data from the Fermi Gamma-ray Space Telescope (FGST) is analyzed here to get the corresponding GeV spectrum. Both the HESS and FGST spectrum for this source are combined to discriminate between the various EBL models in literature. The upperlimits obtained from the VHE observations on 3C 279, another well known GeV bright quasar, are also presented.

In chapter 6.1 MonteCarlo simulations of parent samples of VHE-blazar is done to study the effect of EBL extinction on the resulting VHE detected sub sample. The results of the simulation are compared with the true VHE blazar sample to test if any of the

simulated parent sample properties could be constrained (section 6). The rest of this chapter looks at the uncertainty in the EBL extinction. This uncertainty is dependent on the uncertainty in the cosmology (section 6.2) and the uncertainty on the EBL density (section 6.2 and section 6.4). These factors contributing to the uncertainty on the EBL extinction are estimated and compared.

Chapter 7 summarizes this work and presents an outlook.

Introduction

2.1 Active Galactic Nuclei

The compact central regions of some galaxies that are very bright compared to the entire galaxy they are in, are termed as ***A****ctive **G***alactic **N***uclei* (AGN). The host galaxies with such bright nuclei are called *active galaxies*. AGN come in many flavors. While Seyfert galaxies have the nucleus whose luminosity in visible light is comparable to the light emitted by all the stars in their host galaxies, quasars are typically 100 times or more brighter than their host galaxies. While optical spectra were recorded for AGN in early 1900, they were identified as AGN with the discovery of Seyfert galaxies in 1943 (Seyfert 1943). Quasars (short for ***Q****ausi **S***tellar **R***adio sources*) were discovered in the first radio surveys in the late 1950s and 1960s, which gave the 3C, 3CR Cambridge catalogs (Edge *et al.* (1959) and Bennett (1962) respectively) for the northern sky and the Parkes (PKS) catalog (Ekers 1969)) for the southern sky. Quasars were identified as such, in 1963 with the identification of hydrogen Balmer lines in the optical counterpart for the radio source 3C 273 which gave it a cosmological distance with $z = 0.158$ (Schmidt 1963). Later on most AGN were found to be bright X-ray sources, Elvis *et al.* (1978).

AGN are known to emit over the entire electromagnetic spectrum, from radio to TeV energies. The emission is characteristically non-thermal. A fraction of these show jet related activity in multiple wavelengths. There are many classifications based on the observational characteristics that led to their discovery in various wavelengths. A convenient way to observationally classify these is by their radio brightness, conventionally called radio-loud and radio-quiet.

2.1.1 Observational classification

Radio-quiet AGN: These are bright optical sources, and the radio emission from jet related phenomena is negligible.

➤ Seyfert Galaxies: These are usually in spiral or irregular galaxies, show optical nuclear continuum emission. These are subdivided into Seyfert I or Seyfert II, based on the presence or absence respectively, of strong broad emission lines.

➤ QSO (Quasi Stella Objects): These always show strong continuum emission in optical and sometimes in X-ray, in addition to broad as well as narrow optical emission
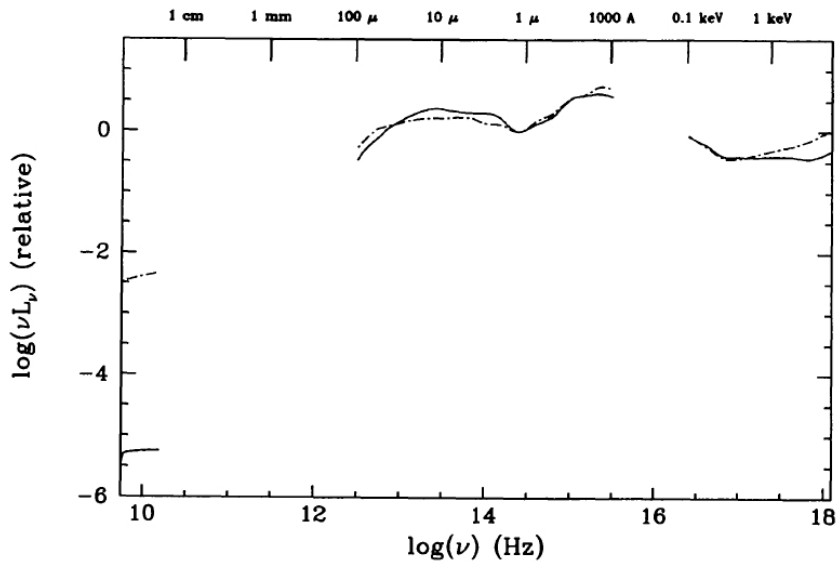
Figure 2.1: The average radio to X-ray continuum shape of quasars, normalized at 1.25μm (Elvis *et al.* 1994). The radio loud (dashed line) and radio quiet (solid line) show a vast difference in radio luminosity. In addition the big blue bump ($0.1 \sim 1\mu$m) dominates this range of frequencies. Radio loud sources show an rising X-ray spectrum in contrast to the radio quiet.

lines. Host galaxies could be spiral, irregulars or ellipticals.
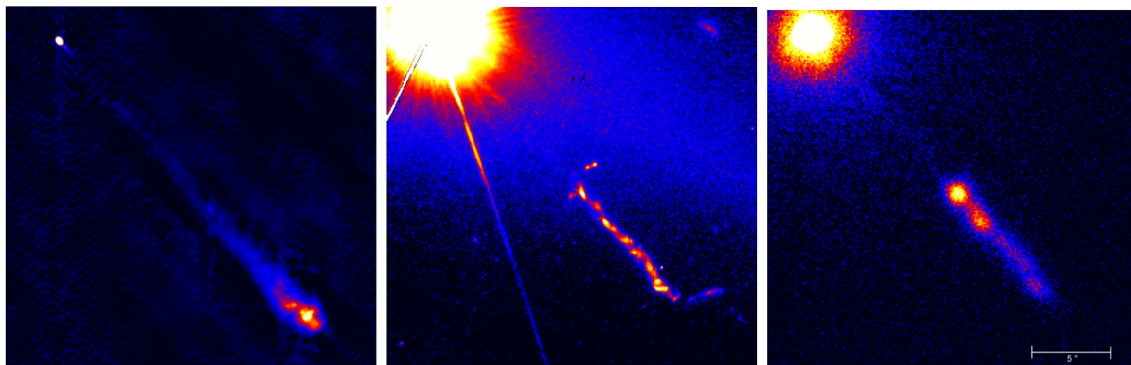
Figure 2.2: The jet of quasar 3C 273, in radio (left) from MERLIN/Jodrell Bank Observatory, optical (middle) from HST and X-ray from Chandra X-ray Observatory.

Radio-loud AGN: These have the radio emission from jets and the radio lobes (where visible) dominating the luminosity of the AGN in radio, and sometimes other frequencies as well. These are mostly hosted in elliptical galaxies.

➤ Radio galaxies: These show nuclear and extended radio emission. Classified as FR I or FR II types, depending on whether the distance between the radio hot spots is less or more than half of the extension of the source. This is thought to be due to jet speeds that are subsonic for FR I or supersonic in case of FR II. Host galaxies are almost always ellipticals.

➤ Quasars: These are similar to QSOs in all aspect except that these are bright in

radio. These could either be flat spectrum radio quasars (FSRQ) or steep spectrum radio quasars (SSRQ). These show strong optical continuum emission, broad and narrow emission lines, and strong X-ray emission, together with nuclear and often extended radio emission.

➤ Blazars: These are characterized by a blue optical continuum, rapidly variable, and polarized optical, radio and X-ray emission. These show no optical emission lines, broad or narrow, thus their redshifts can only be determined the spectral lines of their host galaxies. These consist of BL Lac objects and optically violent variables (OVV). OVV and FSRQs are essentially the same, i.e. FSRQ share the property of rapid variability in optical and other wavelengths, and due to the similarity in their continuum emission, fall into blazar category as well. It is believed that relativistic effects due to the small jet pointing angles to our line of sight boosts both the luminosity of the jet and the amplitude of variability.

The blazar class, is the AGN type consisting of the majority of extragalactic VHE sources, 27 sources as of November 2009[1]. The non-blazar VHE AGN being - the radio galaxies M 87 and Cen A, and the starburst galaxies NGC 253 and M 82.

Energetics of the emission from AGN, with luminosity in the range of $10^{45-49}\, erg/s$, and their long term stability, lifetime $\sim 10^7\, years$ - have led to the widely accepted idea that these are powered by an accretion disks around a super massive black hole (SMBH, with mass $\sim 10^{6-10} M_\odot$). Evidence that observational properties of various classes of AGN are highly dependent on the viewing angle of the jets has led to Unification Models, see for example Urry & Padovani (1995) for a review. Figure 2.3 shows the various constituents of a generic AGN. According to this scheme blazars, i.e. BL Lac objects (BL Lacs) and
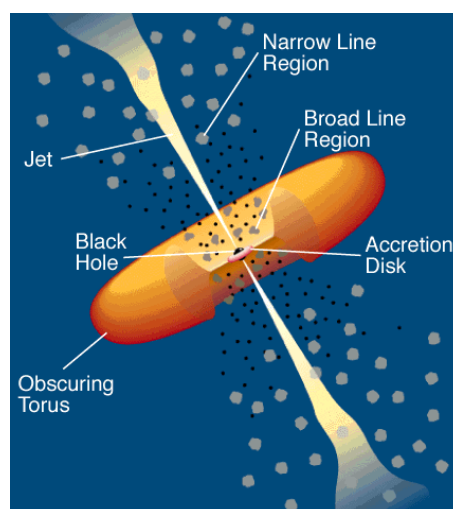
Figure 2.3: The unification model of AGN, Urry & Padovani (1995).

FSRQs have their jets pointing straight in the direction of the earth or nearly so, with

---

[1] http://tevcat.uchicago.edu/

inclination angles $< 15°$, to as low as the order of unity. Both show large bulk Lorentz factors and Doppler boosting effects in their emission. While there is some uncertainty about the connection between BL Lacs and FSRQs, it is true that FSRQs are in general more distant and more luminous of the two. The models of the nonthermal emission mechanism in VHE blazars is discussed next.

2.1.2 Non thermal emission in VHE blazars

Blazars typically show a double humped non thermal continuum from radio to γ-rays. Figure 2.4[2] shows the broad band SED of 2 FSRQs and 2 BL Lac objects. While 3C 279
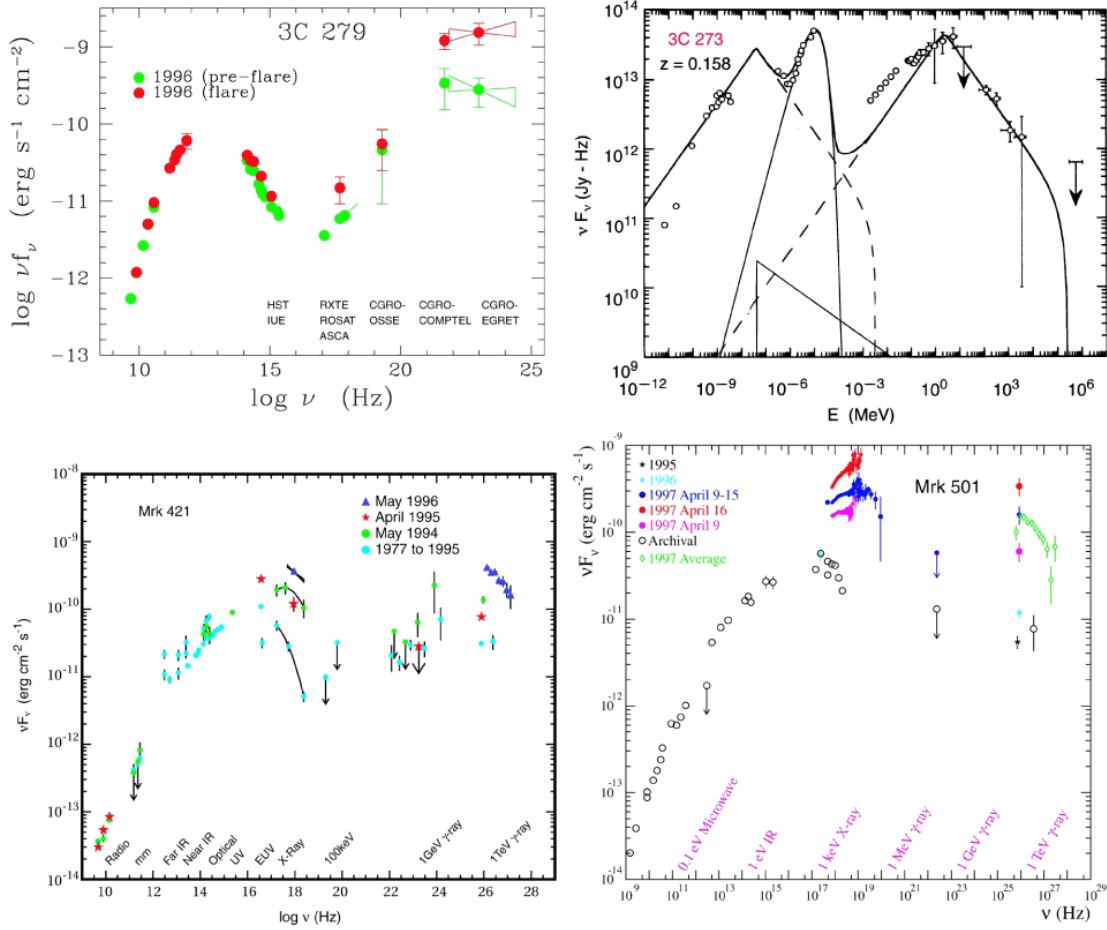
Figure 2.4: The broad band SED of 4 blazars. At the top are two FSRQs 3C 279 ($z = 0.54$), an OVV and bright GeV source in the EGRET era, and 3C 273 ($z = 0.158$) the brightest nearby quasar and also a GeV source. Note that while 3C 279 shows signs that the GeV spectra might extend further into the VHE range, 3C 273 seems to have a steeply decreasing spectra at GeV frequencies. In fact 3C 279 is the only FSRQ which has a claimed VHE detection. The bottom row shows two bright VHE blazars Mrk 421 and Mrk 501 (both at $z \approx 0.03$). These are nearby blazars and were the first extragalactic VHE sources. Notice the double peaked structure of the nonthermal emission in 3C 279, and the Markarians. Also note the high Compton dominance in 3C 279. *Credit: A.E. Wehrle, M.A. Catanese, J.H. Buckley and Whipple Collaboration*

---

[2]this and figure 2.5 are from `http://heasarc.gsfc.nasa.gov/docs/cgro/images/epo/gallery/agns/`

and 3C 273 are quasars, Mrk 421 and Mrk 501 are Bl Lacs. Except for 3C 273 which shows an additional (thermal) component at low energies, the other three show a clear double peak structure. According to the frequency of the low energy peak Giommi & Padovani (1994), BL Lacs are subdivided into low frequency peaked BL Lacs (LBL), intermediate BL Lacs (IBL) and high frequency peaked BL Lacs (HBLs), for the low energy. Both Mrk 421 and Mrk 501 shown here, are examples of HBLs, with their low energy peak in the UV to X-ray energies. Furthermore for BL Lacs, the νF_ν representation shows the peak energy flux in both the components at approximately the same level, in contrast to the spectrum of FSRQs which show a higher energy flux at the high energy peak. This is termed as high Compton dominance, alluding to a dominating inverse Compton component for a leptonic scenario, section 2.1.2.1. The flat nonthermal spectrum over a wide range of frequencies and high polarization strongly hint that the radio to X-ray emission is from synchrotron mechanism. The emission mechanism of the high energy component is how ever not so clear. There are two models which seem to explain most of the observational properties of blazars including the VHE emission. There are however differences. These models are described in this section.

Since it is observationally compelling that the power law emission components from radio to X-rays are due to synchrotron radiation, it is necessary to have a charged particle distribution which is essentially a power law to generate such an SED. Thus the common feature of both these mechanism is that it involves the acceleration of charges particles to VHE. It is believed that this happens via first-order Fermi acceleration in the shocked jets of the blazars, see figure 2.5. In this process a particle gains energy on average while
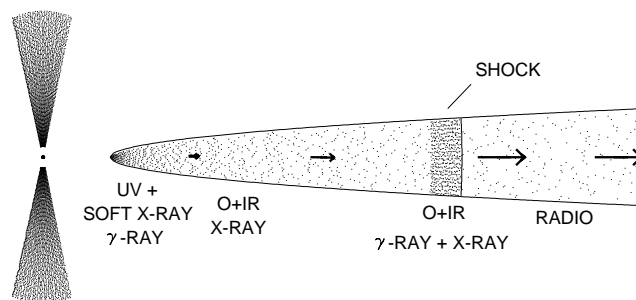
Figure 2.5: The schematic picture of a jet in a radio loud AGN. The shock is produced by matter ejected at supersonic speed from the vicinity of the SMBH, which rams into the ambient medium. Charged particles are then accelerated at this shock front generating the observed bright knots in various wavelengths. When the jet is aligned in the direction of the earth the luminosity is Doppler enhanced. *Credit: A. Marscher (Boston U.)*

diffusing to the down stream medium which has a magnetic field which isotropizes it, making it possible that it might diffuse back into the upstream medium. When this happens the shock which travels at supersonic speed would ultimately catch up with it and it diffuses back to the down stream medium, thereby getting another 'kick' in energy every time it does so. This results in a particle distribution which is a power law. The only way a particle can escape is when it diffuses far into the down stream medium.

Particle acceleration might also happen via second-order Fermi acceleration (Fermi 1949; Rieger *et al.* 2007), sheer acceleration (Rieger & Duffy 2004) or photon breeding (Stern & Poutanen 2008). The fractional contributions of all these mechanisms or a clear dominance by one is not yet well understood.

When charged particles are accelerated to relativistic energies, in the presence of a magnetic field they produce ***synchrotron radiation***, which is a process of magneto-bremsstahlung. This process is well described in textbooks on astrophysical radiation phenomena, e.g. in Shu. (1991) For a powerlaw distribution of charged particles -

$$(2.1) \qquad\qquad n(\gamma) = n_0 \gamma^{-p}$$

where γ is the Lorentz factor of the particles; the net synchrotron emission is the superposition of all the emission at each individual electron energy. The resulting synchrotron power (or in other words spectrum) also follows a powerlaw relation given by -

$$(2.2) \qquad\qquad F_\nu \propto n_0 B^{(p+1)/2} \nu^{-(p-1)/2}$$

where the photon frequency is ν, and the magnetic field is B. Below a certain Lorentz factor, $\gamma_m in$ for the particle distribution the particles will self absorb the synchrotron photons and are therefore optically thick. Below this threshold frequency the photon spectrum is given by $F_\nu \propto B^{-1/2} \nu^{5/2}$, which is dependent only on the magnetic field.

Since the environment of jets is bathed in radiation either self generated by the process above, or thermal radiation from the accretion disk or the broad line region (BLR) or even the cosmic background. These photons can upscatter of the relativistic particles and be boosted to very high energies. This is efficient for light particles, namely electrons (positrons). This mechanism is called ***inverse-Compton*** (IC) emission. The scattering cross section is dependent on the product of the particle energy. For low energies it is approximately the Thomson scattering cross section, σ_T, but for high energies it goes roughly as the inverse of the energy of the particle. The spectrum of the upscattered photons for a charged particle spectrum given in equation 2.1, in terms of the photon energies is -

$$(2.3) \qquad\qquad F_{\epsilon_1} \propto n_0 \left[\int \epsilon^{(p-1)/2} n(\epsilon) d\epsilon \right] \epsilon_1^{-(p-1)/2}$$

where ϵ_1 is the energy of the upscattered photon ($\epsilon_1 = h\nu_1$, with h the Planck's constant) and the soft photon (i.e. before being scattered) has energy, ϵ with the distribution, $n(\epsilon)$. Thus the integral is over all possible energies of the soft photons. Notice that the spectral index for the synchrotron (equation 2.2) and the IC photons has the same value of $-(p-1)/2$.

Since the emission region is assumed to be moving with the shock, it has relativistic

bulk motion, with Lorentz factor Γ. Thus the enhanced luminosity due to ***relativistic beaming*** or ***Doppler boosting*** in the direction of the bulk motion is given as (Aharonian 2004):

$$(2.4) \qquad L_o \approx D^4 L, \; where \, D \equiv \frac{1}{\Gamma(1 - \frac{u}{c}cos\theta)}$$

Here L_o is the observed luminosity at earth and L is the rest frame luminosity at the source. The Doppler factor is the function of u, the velocity of the bulk motion, and θ, the angle between the line of sight and the direction of the bulk motion in the emission region of the jet.

There are other processes that emit photons, one of those is via the decay of the more heavier charged particles. One such scenario is described later in section 2.1.2.2.

There are also a number of absorption processes in the emission region as well as in the inter galactic space. One important mechanism is pair production from photon-photon interactions. This mechanism results in the annihilation of photons with the peak in the cross section at product of energies approximately equal to $4m_e c^2$. This means the soft photon wavelength $\lambda(\mu m) \approx 1.24 E_\gamma(TeV)$ of the high energy photon. Meaning for VHE γ-rays the soft photon is in optical to IR wavelength. Due to the radiation fields in the emission region this effect is expected to be high in quasars which are bright in radio and optical. However for blazars, where the viewing angles are small, the relativistic beaming of the highest energy photons makes these objects shine in the VHE regime as well. The calculation of the extinction of the VHE flux due to intergalactic absorption in this way is described in detail in section 2.4.

2.1.2.1   Leptonic models

If the accelerated particles responsible for the emission are electrons (positrons) then the processes are conventionally termed *leptonic* models. In such models there is a spherical emission region which gets an injected electron distribution which is generally described by a broken powerlaw. This results in a synchrotron component that has 3 power law component. As for the case of a simple power law electron distribution, the lowest component corresponds to the self-absorbed rising (in νF_ν verses ν) part and two falling powerlaws corresponding to the synchrotron emission of the two powerlaws components of the electron distribution. These synchrotron emission producing electrons can furthermore upscatter low energy photons via IC mechanism and case the second bump in the broad band SED, which appears beyond the X-ray part for VHE blazars. If the upscattered soft photons are generated within the same emission region by the synchrotron emission this mechanism is called the Synchrotron Self Compton (SSC), see left panel of figure 2.6 (see for example Maraschi *et al.* (1992); Tavecchio *et al.* (1998); Fossati *et al.* (2008)), whereas if the soft photons are generated outside the spherical emission region, e.g. in the accretion disk or

the BLR, or a dusty torus, it is called the Synchrotron External Compton (SEC or simply EC) mechanism (Dermer & Schlickeiser 1993; Sikora *et al.* 1994; Wagner & Witzel 1995). If one single spherical region is used to explain the entire MWL SED it is referred to as a one-zone model. A simple implementation is given in Krawczynski (2008).
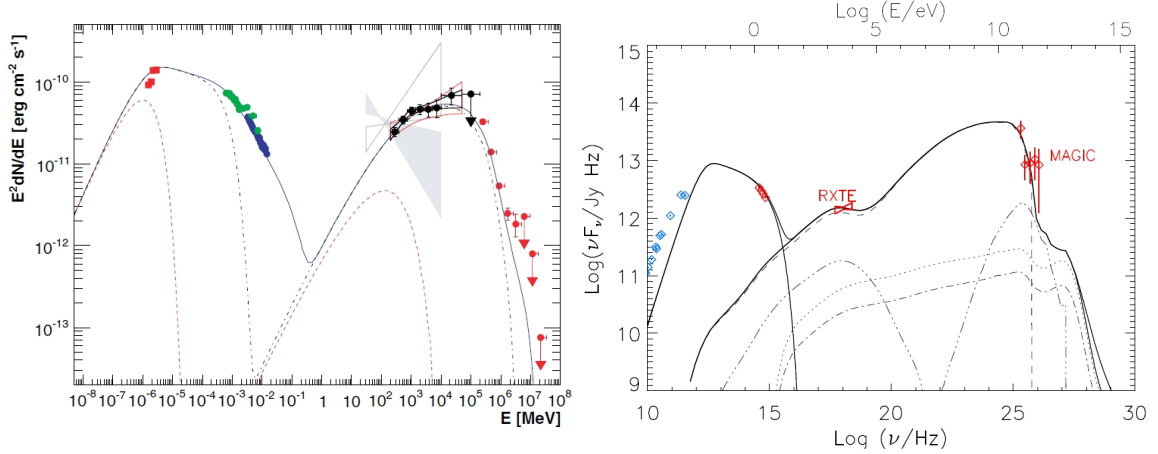
Figure 2.6: **Left:** The one zone SSC fit to the multiwavelength data on PKS 2155-304, from Aharonian *et al.* (2009). **Right:** The hadronic model fit, from Böttcher *et al.* (2009), to the 3C 279 MWL data from 23rd February, 2006 also including the VHE detection by MAGIC. This hadronic model consist of a proton synchrotron component including an external photon field from the BLR.

2.1.2.2 Hadronic models

When the accelerated particles involve protons, the models are termed hadronic. Protons accelerated to VHE energies can produce VHE photons via π^0 (Pohl & Schlickeiser 2000) decay from the interaction of the proton with matter or photons ($p\gamma \rightarrow \pi X$; where X is particle that conserves the charge). Synchrotron emission from protons and the secondary decay products in the presence of a magnetic field (Mannheim *et al.* 1991; Mannheim & Biermann 1992; Mannheim 1993; Mücke & Protheroe 2001; Mücke *et al.* 2003) can also explain the high energy bump in the SED. In such scenarios the low energy bump can still be due to the synchrotron emission of electrons. The signature of hadronic models are the production of neutrinos, though these are very hard to detect due to their negligible cross sections. See right panel of figure 2.6 from Böttcher *et al.* (2009) for an example fit of a hadronic model to the FSRQ 3C 279. This particular data set could not be fit well with a SSC or EC model without invoking unusually small magnetic fields and/or very high Doppler factors, in addition to not being able to simultaneously fit the RXTE data.

2.2 The Extragalactic Background Light

The inter galactic space is filled with photon fields in all wavelengths, which is referred to as the background radiation, and is isotropic. The back ground in the UV to IR is collectively called as the Extragalactic Background Light (EBL), and has the second highest energy density per decade after the Cosmic Microwave Background. The EBL usually refers to the photon UV-IR field at the present epoch, i.e. $z = 0$; while a number of terms like Metagalactic Radiation Field (MRF), and Cosmic Infrared Background(CIB) have been coined to describe the EBL at non-zero redshift. In this work all such fields are referred to as the EBL, since the relevant redshifts for VHE blazars is quite low ($z < 0.5$). The EBL is the sum total of all the star light radiated in the entire cosmic history. It is seen in two peaks, the high energy peak in the UV to mid-IR($\sim 10\mu m$) is the light directly emitted from stars, while the low energy peak in the mid-IR to far-IR($> 10\mu m$ and peaking at $\sim 100\mu m$) background is the star light that has been absorbed and re-emitted by dust. Other sources like emission from AGN and quasars probably contribute to less than 20% of the total EBL (Matute *et al.* 2006).

The part which is most relevant for absorption of VHE emission is the near-IR to mid-IR part of the EBL.

2.2.1 Summary of measurements

Direct measurements are hampered due to the overwhelming foreground from the zodiacal light, see Hauser & Dwek (2001) for a review. There are also contribution from nearby galactic sources. The subtraction of this bright foreground (possibly one or two magnitude higher than the EBL density) leaves the measurements with large uncertainty, see figure 2.7, right panel. Upper limits are mostly from direct measurements with the
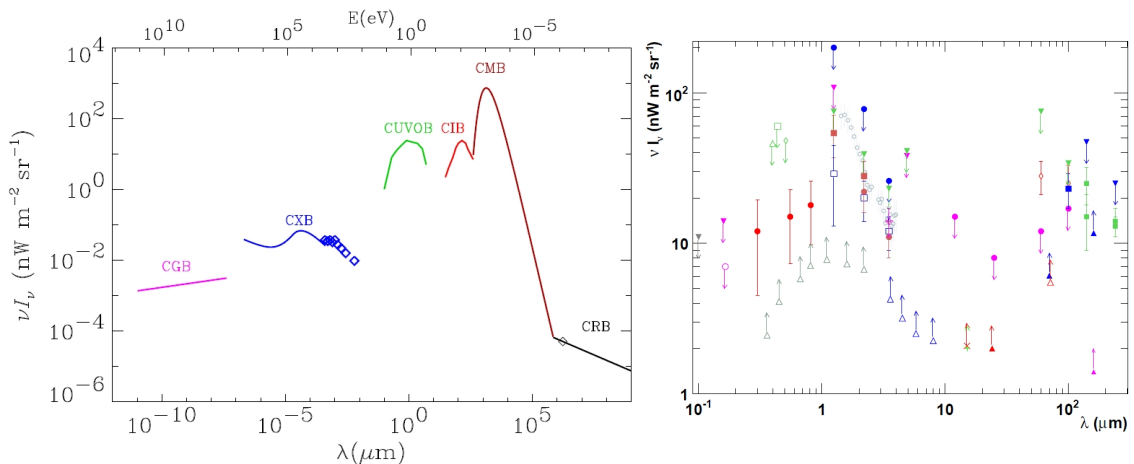
Figure 2.7: **Left:** The background photon field at all wavelengths, figure from Hauser & Dwek (2001). **Right:** Various measurements of the EBL (taken from Mazin & Raue (2007)).

DIRBE instrument on the COBE satellite, Lower limits are from source counts, open grey triangles, and also open green triangles from SPITZER measurements. Within these measurements there is a but just the confirmation of a double peak structure. The uncertainty is quite large, though recent VHE measurements Aharonian *et al.* (2006b) have put the possible EBL level near to the lower limits as implied by the source counts.

2.2.2 EBL SED models

There are a number of EBL models that analytically describe the EBL density as well as its evolution with z, which have been obtained by a number of ways. There are *forward-evolution models* that start out with a semi-analytical model of galaxy formation and their evolution - as in Primack *et al.* (2001, 2005); Gilmore *et al.* (2009). There are the *semi empirical, backward-evolution* models as in Malkan & Stecker (1998); Stecker *et al.* (2006) that use IR spectra measurements of galaxies as a function of luminosity and luminosity functions of IR galaxies to construct the EBL at various redshift. In Kneiske *et al.* (2002) semi empirical models of star formation rate as a function of redshift are used to derive the EBL density and its evolution. Franceschini *et al.* (2008) uses measurements of cosmological survey data - like number counts, redshift distributions, luminosity functions of galaxies and use a backward-evolution model to estimate the changing EBL through z. These various models are collectively shown in figure 2.8. These models all lie within the measurements shown in figure 2.7, right panel. However the extinction suffered by VHE
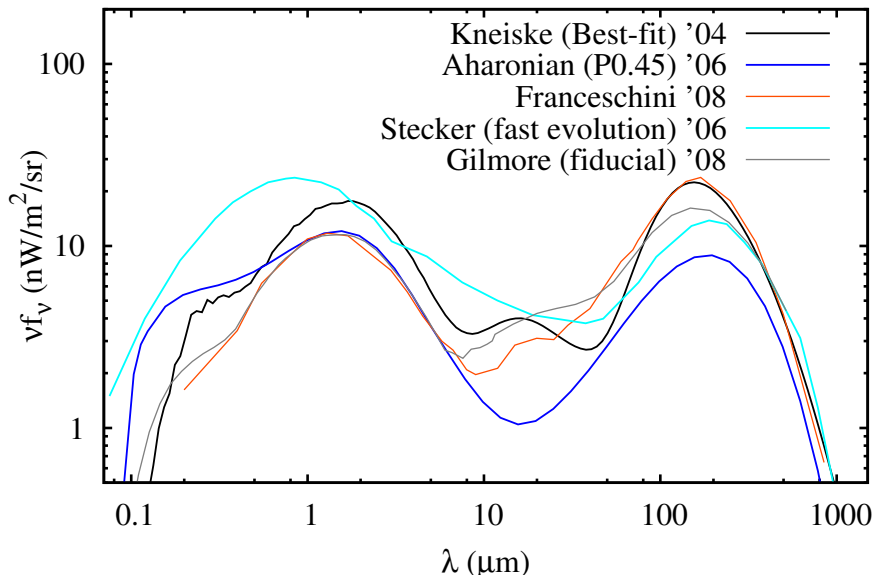
Figure 2.8: Various EBL-model curves.

photons calculated from these models does indeed vary as much as 50 times for a γ-ray energy of $300\,\text{GeV}$ for a source at $z \approx 0.35$ (see figure 5.10).

As first suggested by Stecker *et al.* (1992), the absorption features in the VHE

spectra of blazars can provide indication of the amount of intergalactic extinction the fluxes of these sources suffered. This has been worked out for many blazars (for example see Dwek & Krennrich (2005), Aharonian *et al.* (2006b), Mazin & Raue (2007), Imran & Krennrich (2007) among others) but is limited by the uncertainty in the intrinsic spectrum of the VHE sources. In chapter 5 it is demonstrated how simultaneous constraints on the intrinsic VHE spectra (using FGST measurements) and the EBL level (by fitting a spectral model that includes EBL extinction, to the GeV-VHE spectra) can be made, using the *gamma*-ray data of the distant quasar PKS 1510-089.

2.3   The H.E.S.S. IACT array

The High Energy Stereoscopic System (H.E.S.S.), Hinton (2004); Aharonian *et al.* (2006c) and is an array of 4 Imaging Atmospheric Cherenkov Telescopes (IACTs) located in the Khomas highlands of Namibia, at an altitude of 1800 m a.s.l. It was designed and built keeping in mind the advantages in combining a large detector size with stereoscopic view through multiple detectors to achieve sensitivities and energy resolutions in the VHE regime which was without precedent in this field. The complete array is functional in stereoscopic mode since January 2004. The individual telescopes stand 120 m apart in a
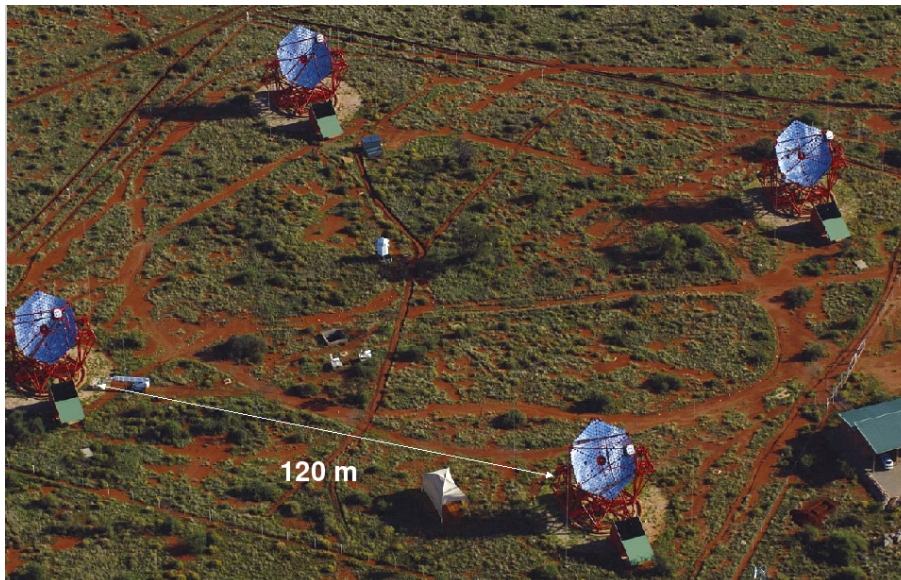
Figure 2.9: H.E.S.S. array of cherenkov telescopes. (*from www.mpi-hd.mpg.de*)

square grid. Each telescope has a optical support structure (OSS) of the Davies-Cotton style with 382, 60 cm diameter mirrors. The flat-to-flat diameter of the OSS is 13 m, giving an effective surface area of $107\,m^2$.

The HESS imaging camera (figure 2.10) consist of a hexagonal array of 960 photo-multiplier tubes (PMTs). Each PMT pixel corresponds to $0.16°$ diameter projected diam-

eter on the sky. The field of view is $5°$. The data analysis including the various background

Figure 2.10: The imaging camera of a H.E.S.S. telescope.

subtraction methods for HESS is described in detail in Aharonian *et al.* (2006c); Berge *et al.* (2007). The analysis that is relevant to this work is described in the chapter 5 and Appendix B.

2.4 Optical depth for VHE γ-rays

VHE γ-rays are absorbed in the intergalactic medium, due to the interaction with the EBL photon field. This happens via the pair production mechanism: $\gamma_\epsilon + \gamma_\gamma \rightarrow e^- + e^-$. Here I lay out the procedure implemented in this work to calculate the optical depth for the photon-photon interaction. The procedure explained in this section is implemented in *Mathematica*[3] to calculate the optical depth for a source at any given redshift. The extinction is given by $exp(-\tau)$, where τ is the optical depth.

The photon-photon pair production is the reverse process of pair-annihilation. The explicit expression of the cross section for pair production interaction is given in Heitler (1960); Coppi & Blandford (1990) among others as:

$$(2.5) \quad \sigma(E\gamma, \epsilon, \theta) = \frac{3\sigma_T}{16}(1-\beta^2) \times \left[(3-\beta^4)ln\left(\frac{1+\beta}{1-\beta}\right) + 2\beta(2-\beta^2)\right]; \; where \; \beta = \sqrt{1 - \frac{2}{E_\gamma\epsilon(1-cos\,\theta)}}$$

The cross section σ, is thus a function of the angle between the colliding photons, θ and the photon energies in units of electron rest mass energy, with E_γ as the VHE photon energy, and ϵ as the EBL photon energy. Here σ is in units of σ_T, the Thompson cross section.

This interaction has a strict kinematic threshold given by:

$$(2.6) \qquad\qquad E_\gamma\epsilon(1-cos\,\theta) \geq 2$$

---

[3]`http://www.wolfram.com/products/mathematica/index.html`

The expression in equation 2.5 has to be integrated over all angles to get the effective cross section for all possible collision angles. An approximate analytical expression for the angle averaged (integrated) cross section is given in Aharonian (2004) and is accurate to better than 3% of the explicit angle integrated value of equation 2.5. This angle averaged value is adopted in this work and is given as:

$$(2.7) \qquad \sigma(s_0) = \frac{3\sigma_T}{2s_0^2} \left[\left(s_0 + \frac{1}{2}ln\,s_0 - \frac{1}{6} + \frac{1}{2s_0} \right) ln\left(\sqrt{s_0} + \sqrt{s_0 - 1} \right) - \left(s_0 + \frac{4}{9} - \frac{1}{9s_0} \right) \sqrt{1 - \frac{1}{s_0}} \right]$$

where $s_0 = \epsilon E_\gamma$, the energies, as before, are in units of $m_e c^2$, the electron rest mass energy. Both these forms of the cross section are plotted in figure 2.11, left panel, and clearly match very closely.
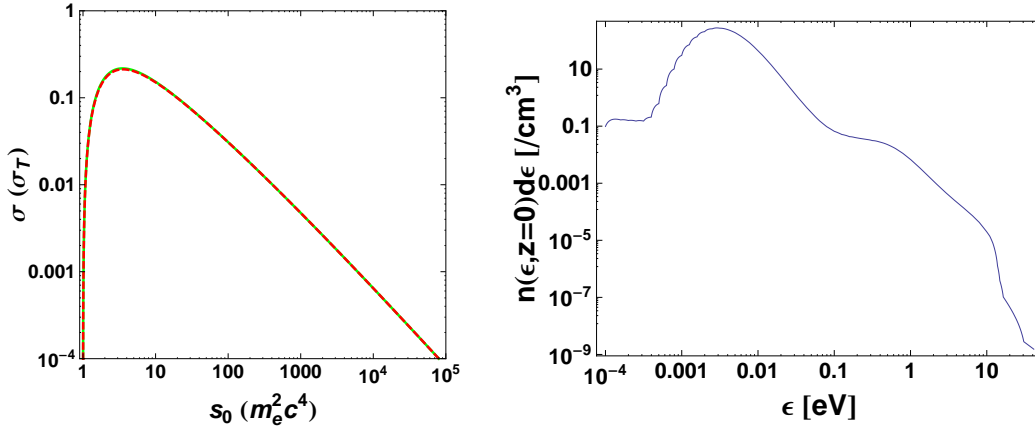
Figure 2.11: **Left**: The photon-photon interaction cross section in units of Thompson cross section, as a function of the product of the photon energies in units of electron rest mass energy. The solid green line is the approximation to the angle averaged (integrated) cross section from Aharonian (2004), while the dashed red line is the explicit angle integrated cross section from the detail expression in Coppi & Blandford (1990). **Right**: The EBL photon density at $z = 0$, as a function of photon energy, ϵ in eV. This is obtained from the corresponding wavelength representation of the EBL photon density, as shown in figure 2.8, blue curve.

The expression for optical depth is given in many papers, e.g. in Nikishov (1962); Gould & Schréder (1966); Stecker *et al.* (1992) among others. Here I give the optical depth (τ) as a function of the observed γ-ray energy, E_0 and the source redshift, z - in terms of the angle averaged cross section, $\sigma(s_0)$:

$$(2.8) \qquad \tau(E_0, z) = \int_0^z \left[\frac{dl}{dz'} \int_{\epsilon_{min}}^{\epsilon_{max}} \sigma(s_0)\, n(\epsilon', z')\, d\epsilon' \right] dz' \,;$$

$$where \left(\frac{dl}{dz'} \right) = c\left(\frac{dt}{dz'} \right) = \frac{c/H_0}{(1+z')E(z')}, \; s_o = \frac{E_o(1+z')\epsilon'}{(m_e c^2)^2}, \; and\, n(\epsilon', z')\, d\epsilon' = (1+z')^3 n(\epsilon, 0)d\epsilon$$

is the comoving photon density.

Thus the optical depth (τ) a γ-ray photon arriving with energy E_0 from a source at z encounters, is proportional to the angle integrated cross section of interaction times the target photon density of the EBL photons. This is the integrated over all possible EBL photon energies ($\int_{\epsilon_{min}}^{\epsilon_{max}} d\epsilon'$) and over the path length traversed by the γ-ray, ($\int_0^z dz'$). The various terms in this equation are now explained in detail.

The $(\frac{dl}{dz'})$ term is the differential length in terms of redshift, gives the cosmological model used in this calculation. In this work a flat universe with $E(z') = \{\Omega_m(1+z')^3 + \Omega_\Lambda\}^{1/2}$ is used unless mentioned otherwise. Values used for the density parameters are - the dark matter density $\Omega_\Lambda = 0.73$, baryonic matter $\Omega_m = 0.27$ and for the Hubble constant is $H_0 = 72 \, km/s/Mpc$, unless specified otherwise. The radiation density, Ω_r and the curvature, Ω_k are ignored except for the specified special cases.

The EBL spectral energy distribution given in Aharonian *et al.* (2006b) is used for the calculation. It gives the photon density, $n(\epsilon, 0)d\epsilon$ at $z = 0$. An EBL photon at z' with energy ϵ' corresponds to a redshifted energy of $\epsilon = \epsilon'/(1+z')$ at $z = 0$. Thus the correct photon density to be used with the cross section for interactions at $z = z'$, in terms of the density at $z = 0$, is given by $n(\epsilon', z')d\epsilon' = [(1+z')^3 n(\frac{\epsilon'}{1+z'}, 0)\frac{d\epsilon'}{1+z}]$. The lower limit of integration, ϵ_{min} is obtained from equation 2.6, and the higher limit, ϵ_{max} is set to $100 \, eV$, which is adequate for all practical purposes (see figure 2.11, right panel). This assumes that the redshift evolution of EBL density is negligible, and holds true for sources at low redshifts. In subsequent chapters where required, extinction curves derived from other EBL models evolving with z is considered.
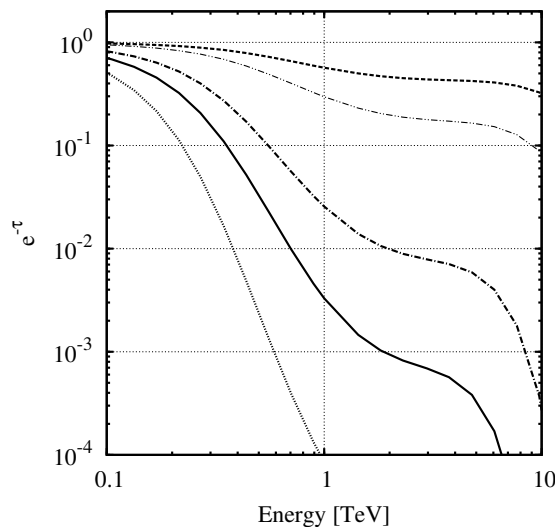
Figure 2.12: The calculated extinction, $exp(-\tau)$ suffered by VHE γ-rays while traveling through the intergalactic medium is shown as a function of the observed VHE photon energy, for a number of redshifts.

The γ-ray photon observed at the earth with energy E_0, at the redshift $z = z'$, is blue shifted to $E_0(1 + z')$, which is the value used in the expression for the cross section, i.e. $E_\gamma = E_0(1 + z')$ in equation 2.7. This is the cross section used in equation 6.1 as mentioned before.

The extinction $exp(-\tau)$ as a function of γ-ray energy calculated as described here, are shown for a number of redshifts in the right panel of figure 2.12.

Part II

Optical monitoring and correlation studies

Using VHE spectra of blazars as a means to study the EBL density requires us to find VHE sources at high redshifts. This is because the optical depth is proportional to the distance and the energy of the γ-ray. Therefore the steepening of the spectra of distant sources will be more pronounced. This however means that we need to find exceptionally bright VHE sources, such that the flux reaching earth is still detectable even though dimmed considerably first of all due to the distance and secondly due to extinction on the EBL. Flaring states of blazars are thus ideal targets for searching for VHE signal from distant blazars. Blazars are known to be extremely variable at all frequencies. There are instances of discovery of VHE blazars with triggered observation from optical flares (Albert *et al.* 2006b, 2007b, MAGIC discoveries of Mrk 180 and 1ES 1011+496 respectively). The correlation in optical and VHE fluxes of blazars is as yet not clear due to lack of long term VHE monitoring of blazars. An optical-VHE correlation is expected since it naturally follows from an SSC process dominated scenario for the VHE emission from blazars in general. Optical photons emitted from the core are the likely target photons for scattering very energetic electrons to generate the VHE photons. This possibility of trigerring VHE observations of flaring states in blazars to discover new distant sources is a major motivation forthe optical monitoring program being carried out using the **A**utomatic **T**elescope for **O**ptical **M**onitoring (ATOM) instrument.

To maximize the observation efficiency of the ATOM instrument, it was envisaged to be run remotely in a robotic mode. As a part of this thesis work I developed a *robot software* to automate the observations throughout the night. This *robot software*, or simply the *robot*, communicates with the electronics interfaces that operate the telescope hardware and the cameras of ATOM.

In the following I give the description of the ATOM instrument and its robotic software (section 3.1.1). In section 3.1.2 an account of the optical monitoring proposal of GeV bright blazars, intended to trigger HESS on optical flares is given. Though the objective of initiating optical monitoring was to discover distant blazars for EBL studies, two interesting secondary outcomes are described in section 3.2, where ATOM data is used to test for correlation in the long term optical and GeV lightcurves of blazars and section 3.3, where the correlation observed between the optical and TeV lightcurve of the

blazar PKS 2155-304 is tested.

Two optical flares (which coincided with GeV triggers as well) on two quasars which were observed with HESS is reported in a dedicated chapter, number 5.

3.1   ATOM

ATOM (see figure 3.1) with a 75 cm primary mirror is located near the H.E.S.S. array and is operated by the H.E.S.S. collaboration. It was build by Zeiss as a prototype for computer controlled azimuthal mounting. Originally built in late 1970, after being used for few decades at the *Landessternwarte* (*LSW*), Heidelberg, it was modified for robotic operations prior to being moved to the HESS site in Namibia. The main-mirror cover was motorized and the electronics control were replaced with new systems developed by the Hamburger Sternwarte. The mirrors were re-aluminized in 2005. It has two CCD cameras, the main science camera and a guiding camera. The science camera placed at the Cassegrain focus is an *ALTAE*47+ from Apogee Instruments Inc., with a *E2V* 47-10 *grade* 0[1] CCD chip. The on sky resolution is $0.47''$/pixel, with a maximum FOV of 8×8'. In addition it has a electronic controlled motorized filter wheel unit, custom made at *LSW*, with the Johnson-Cousins UBVRI broad-band photometric system (Bessel 1990).

Figure 3.1: The **A**utomatic **T**elescope for **O**ptical **M**onitoring (ATOM).

On a typical night, around 40 different targets are observed, in multiple filters if desired. The telescope is operated in a completely automatic mode, which means the telescope system gets a nightly schedule via Internet, prepared before the start of nightly observations. It then performs all the observations during the entire night without any human interaction or supervision. This operation is made possible by the robot program described in section 3.1.1. Occasionally manual intervention is needed for fine adjustments of the instrument, such as the focusing of the telescope optics or in case of hardware problems.

Data analysis is also done automatically by an analysis pipeline developed by Dipl.-Phys. Marcus Hauser, of the *Landessternwarte*, Heidelberg. This pipeline is run on site in the morning. This pipeline does the standard image reduction (i.e. de-biasing and

---

[1] E2V. CCD47-10 Backthinned Compact Pack - High Performance AIMO Backthinned CCD sensor, June 2000. 12, 15

flat fielding) as well as finding an astrometric solution for each frame down to arc second accuracy using *wcstools* Mink (2005) and the *UCAC2* catalog Zacharias *et al.* (2004). The subsequent source detection and photometry is based on the *SExtractor* package Bertin & Arnouts (1996). The resulting source catalog from each frame is then combined with older observations of the same target and archived.

3.1.1 Robotic operation of ATOM

The robot executes an observation schedule of multiple targets prepared in advance for an entire night. It does so by issuing commands to *telops* (short for **tel**escope **op**eration**s**), the software interface to the ATOM telescope control, and *instops* (short for **ins**trument **op**eration**s**), the software interface to the instrument control. While *telops* allows communication with the hardware - consisting of the enclosure, the telescope altitude and azimuth controls, and focusing system; *instops* communicates with the science and guiding cameras, and the filter wheel unit. Both *telops* and *instops* accept connections from high level programs via TCP/IP connections on specific ports, through a *command-acknowledge-response* message passing mechanism. That is, both interfaces accept commands (possibly with parameters) that are immediately acknowledged, and either a confirmation or error is returned as the response. These interfaces accept multiple connections, and use the same connection to respond to commands send, instead of broadcasting messages over all connections.

The schematic representation of the robot software and its communication with ATOM via the *telops* and *instops* interfaces is shown in figure 3.2. The robot is a program
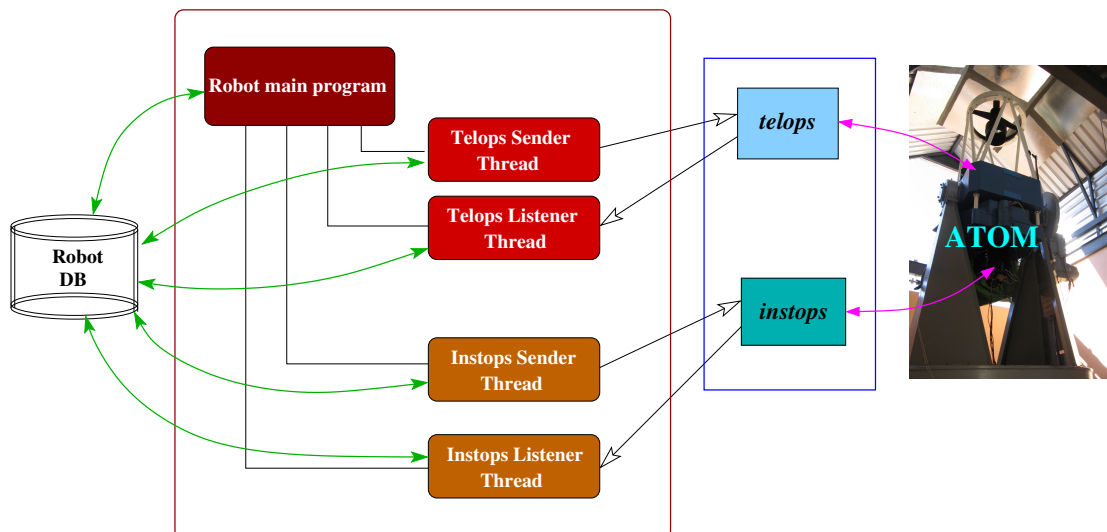
Figure 3.2: The robot software (brown box) consists of the main program and its threads which communicate with the *telops* and *instops* interfaces and execute the ATOM observation schedule. This schedule is stored in the robot database. It also logs all its operations to the same database.

written in the C programming language that communicates with these two interfaces via

a single *stream-socket* connection to each interface. To have quick response and avoid clogging of the sockets the robot was designed and implemented as a multi-threaded program. There are four threads, two for each interfaces, one thread for sending commands and another one for receiving messages. The main program accesses the schedule stored in the Robot data base and logs the status of all commands that finished execution and also the current execution state of unfinished commands.

The current version of the robot program is very stable and has been running observations for entire nights since late 2006. Bugs in previous versions of the software have been removed as and when detected.

3.1.1.1 Observation schedule and the robot DataBase

The robot data-base is implemented in MySQL server (*Version 14.12 Distrib 5.0.51a, for debian-linux-gnu, i486*) stores the schedule yet to be executed for the current night and the log from all previous observations. The robot data base schema is shown in figure 3.3. This is used for debugging the robot software in case of software problems, as
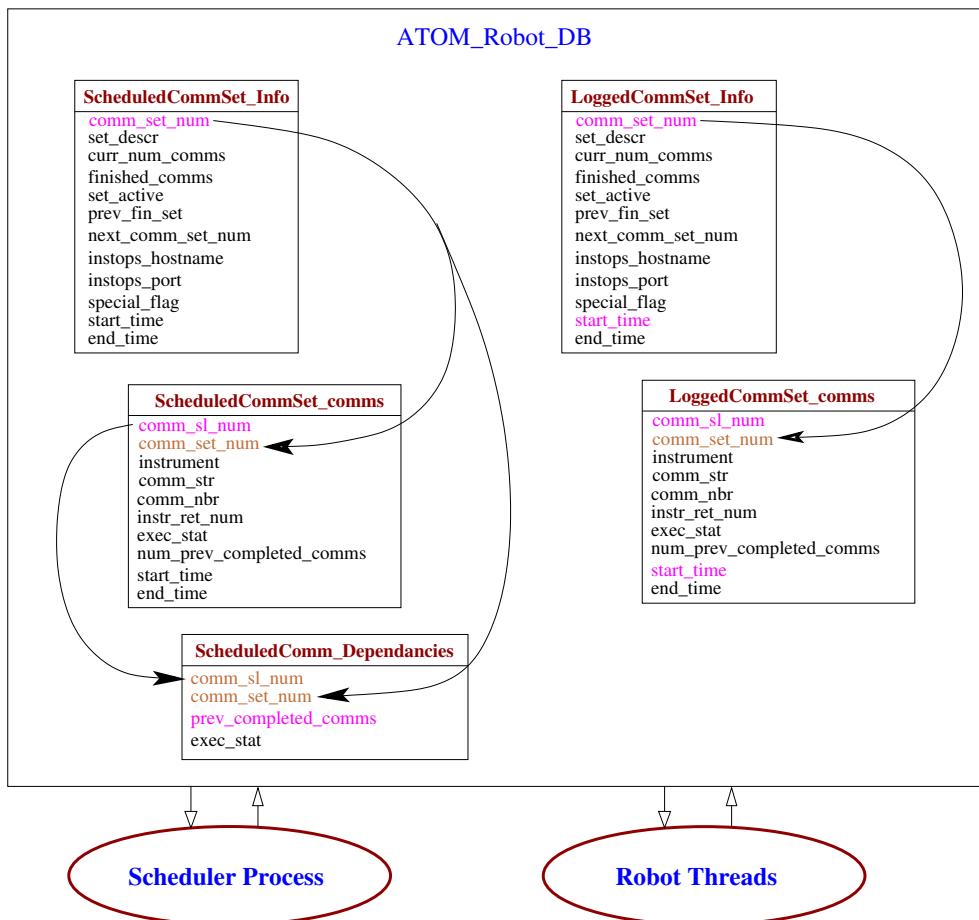
Figure 3.3: The schema for the robot DataBase, named *ATOM_Robot_DB*. Tables are boxes, *primary keys* are shown in color, with arrows showing *foreign-key* relations between tables.

well as tracing problems that might arise to due to other systems such as the interfaces or the hardware itself. Since the instops and telops return an error or time-out in case there is a problem, this state is stored in the robot data base before the robot exits from an unrecoverable error. Currently the schedule for the night is prepared by semi automatic script (implemented by M. Hauser) but in the future it is envisaged to be run as an automatic daemon that continually evaluates and updates the schedule for the night. This way it can respond to time lost due to bad-weather or other problems and optimize the schedule to get the most critical observations in the most efficient manner.

It has 5 tables, three for the schedule for the night and two for the logs. The schedule is prepared as a text file and read into the *"Scheduled"* tables, at the beginning of an observation night. The schedule consists of a number of commands grouped together in sets, each set for the observation a single source. A set can have one exposure with a single filter, or multiple exposures, each with a different filter.

The general information for a set is stored in the *ScheduledCommSet_Info* table. All individual commands in a set are stored in the *ScheduledCommSet_comms* table. Some of the commands need to wait for previous commands to be finished, e.g. exposure cannot be initiated until the proper filter is positioned in front of the camera lens, while some commands can be issued simultaneously, e.g. the telescope can be repositioning to a new source while the filter is being changed, such dependencies are stored in another table, called *ScheduledCommSet_Dependancies*. When each command is executed and the response from the interfaces are received the states of the commands are recorded in the tables in form of codes (*exec_stat* in the tables), which can later be checked in case of errors. On completion of each command set, the entries in *ScheduledCommSet_Info* and *ScheduledCommSet_comm* tables are copied with the respective time stamps to the log tables, viz. the *LoggedCommSet_Info* and *LoggedCommSet_comm* tables. The dependencies are unnecessary for the purpose of the log and not stored.

3.1.1.2   Implementation

This code written in C, is compiled using *gcc version 4.1.2 20061115 (prerelease) (Debian 4.1.1-21)* for *Target: i486-linux-gnu* and runs very stable on a Debian system *version 4.0*. The multi thread code crashes with segmentation fault on the last test on Debian *version 5.0* due to unknown reasons. This problem might be due to a bug in the memory allocation in the new OS version, and could get automatically fixed in the next release.

The logical control flow of the robot *main program* is shown as a flowchart in figure 3.4. The robots' *main program* first reads all the configurations for the ATOM software system. These are the *host names* and *port numbers* of the *telops* and *instops* ATOM interfaces, the connection details for the robot database and a flag that specifies if the observing schedule is to be read initially from a text file or straight from the database. This flag
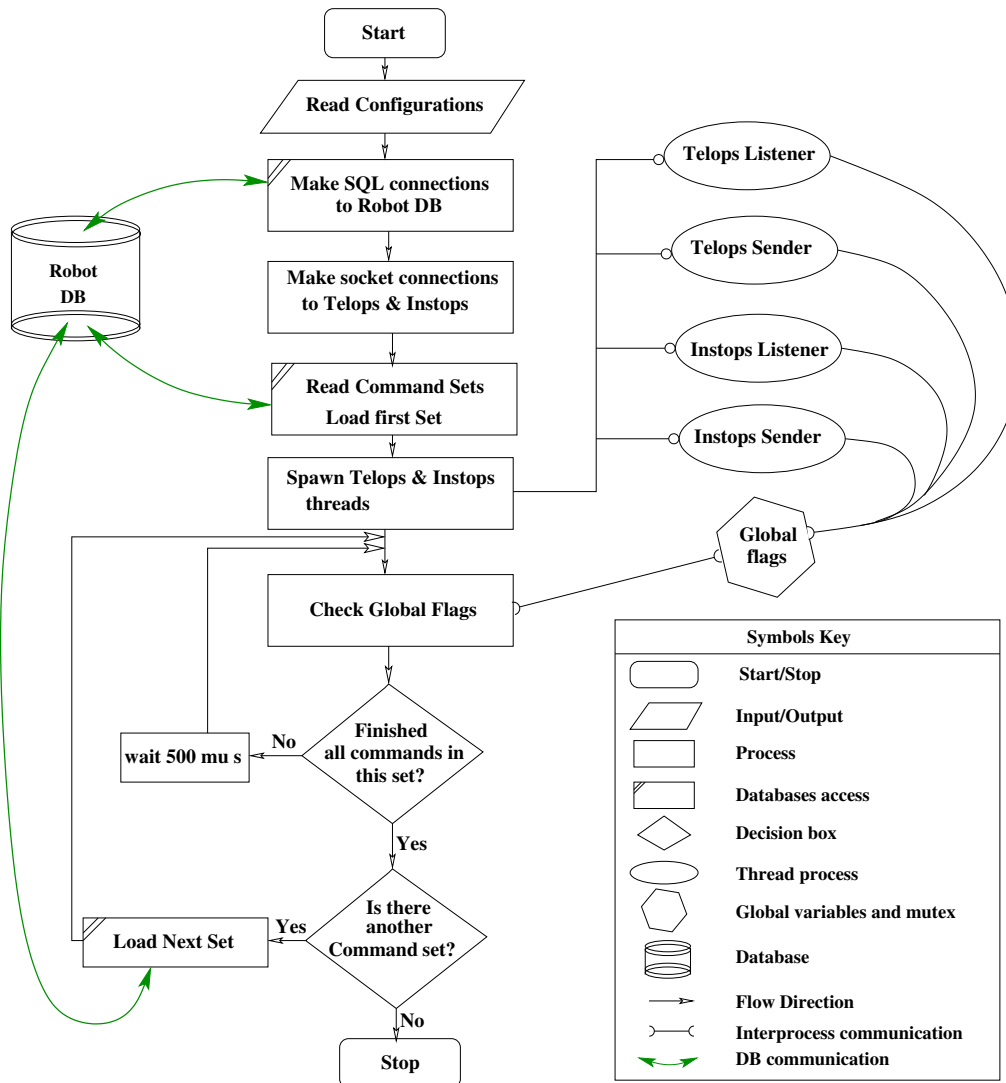
Figure 3.4: *Main program* flow chart.

is currently set to read the schedule from a text-file. When an automatic scheduler is in place the robot database will always hold the most recent schedule. The robot then makes the *stream socket* connections to *telops* and *instops*and also reads in the observing schedule from the text file and copies it to the database tables. It spawns four threads for communicating with the ATOM interfaces. The *sender* and *listener* threads for *telops* use the same *stream socket*, but as the name suggest the *listener* only reads from it while the *sender* only writes to it. The same is true for the *sender* and *listener* threads for *instops*.

Once all threads are created the *main program* loops over one the command sets, one by one. The interprocess communication between the *main program* and the threads it spawns is in this way managed using global variables, which act as *status flags*. Consistency is maintained by locks on these variables using *mutex*, i.e. only one thread can be changing the value of a *status flag* at a given time. *Status flags* reflect the execution status of individual commands in a set and can have the following states - (1) if a command is ready

to be send (2) if it has been sent to the relevant ATOM interface (3) if an acknowledgment has been received from the interface and (4) if the command has successfully completed or (5) there was an error returned. The listener threads continuously polls the *sockets* and update the states on receiving relevant messages. The sender thread sends a command when it sees that the *status flag* is set to condition (1). The command set also has a *active/inactive* flag and once all the commands in the current set are executed the set is marked *inactive* and the *main program* goes on to the next set, until all the observation for the night are done.

3.1.1.3 Handling special situations

The ATOM system has now a weather monitor that can stop observation in case the weather deteriorates, and automatically restarts observations if weather improves. This requires the schedule to be modified in the middle of a night. To allow this in the absence of a automatic scheduler, the previously prepared schedule is truncated. The sets which are done or missed due to bad weather are removed and the observation is resumed from the next possible source. This schedule modification implemented as a separate script and is launched before the robot is restarted.

The error handling in the robot is not extensive at present. In case of broken *socket* connections to the *instops* and *telops* interfaces attempt is made to renew the connection. Apart from this any error from either interface is simply logged in the data base following which, the robot exits.

3.1.2 Optical monitoring and triggers for H.E.S.S

Since it is likely that sources that are bright in the GeV band, could have their spectra extending into the VHE regime - a catalog of GeV bright blazar was sought to select sources for optical monitoring. Initially, sources were selected from the 3rd EGRET catalog (Hartman *et al.* 1999) on the following three primary criteria. Since it is intended to select sources whose GeV spectra extends undiminished into VHE, we selected bright GeV sources with hard spectral indices ($\Gamma - \Delta\Gamma \leqslant 2.50$). Additional restrictions are made on the declination and the redshift of the source. The declination cut, $dec < +20°$ is made to ensure that observation with HESS are possible with small zenith angle. This is necessary since the threshold energy of HESS is proportional to the zenith angle. The redshift cut, $z \leqslant 0.7$ is to ensure that EBL absorption does not dim the VHE flux below the detection level of HESS. A trigger criteria for each object was assigned to request follow up observations with HESS. Most blazars do not have a well defined quiescent level, since they are highly variable, and long term optical light curve is available only for a handful of objects. Initial trigger criteria was set at a brightness level of 2 magnitude brighter than the optical magnitudes quoted in the Veron-Cetty & Veron (2006) catalog.

ATOM has been taking science data since November 2006. As ATOM records lightcurves of sources the trigger value is adjusted from time to time to reflect the quiescent level obtained from long term average states.

Initially a priority was assigned to the objects based on an estimate of the VHE brightness. An estimate for the VHE brightness is obtained by calculating the integral flux above a threshold energy (usually 200 GeV in this work) of the extrapolated EGRET spectra (to VHE energies[2]) which is corrected for EBL absorption (see section 4.1). Later on as it became evident that the available observation time with ATOM was adequate to monitor a much larger sample of GeV bright sources. In addition to providing triggers for HESS follow up, this enables us to record light curves of blazars that are compared to the light curves in other wavelengths to make correlation studies. Thus the declination cut was relaxed to include sources $<40°$, and the cut on redshift was removed. Furthermore the large error on the position of the 3EG sources due to the large psf of the instrument, 1σ error radius of a point source of $5.85°$, at 100 MeV, meant that source identification from a low frequency catalog was required for ATOM pointing. Thus the list of 5 GHz radio counterparts of the 3EG sources , given in Mattox *et al.* (2001) was used, giving 78 sources. This list was cross-checked against the Extended EGRET Catalog (EEC), Casandjian & Grenier (2008), which applies a new Galactic interstellar emission models based on recent CO, HI, dark gas, and interstellar radiation field data. The implication of this revision to the 3EG catalog is that 107 sources could not be confirmed in this new analysis due to additional structures in the interstellar backgrounds. This however effected mostly Galactic sources, while most of the blazars could be confirmed. Out of the 78 sources selected from the Mattox *et al.* (2001) paper, 13 do not appear in the EEC. For all the sources where the optical counterpart for the radio sources is bright enough to be measured with ATOM, the light curves have been recorded since late 2007.

In addition to providing triggers for HESS follow up, this enables us to record light curves of blazars that are compared to the light curves in other wavelengths to make correlation studies.

3.2 Correlating longterm optical and GeV lightcurves of LAT blazars

Correlations between the optical and GeV emission in blazars have been found before, see for example - Wagner & Witzel (1995), flare state of PKS 1406-076 and Wagner (2006), flare in Mrk 421. Previous studies invariably suffered from the low sensitivity of the previous generation GeV instruments. A new era in GeV astronomy begun with the launch of FGST satelite. Combined with the optical light curve from ATOM the long term be-

---

[2]The extrapolation of a GeV spectra to VHE energies followed by the estimation of the VHE integral flux corrected for EBL absorption is described in a later chapter, section 4.1.

havior of blazars in GeV and the optical band can be studied. In this section the optical and the GeV light curves for a selected sample of blazars for the period, August-2008 till April-2009, is studied to check for possible correlations.

3.2.1 The Data Sets

Since August 2008, FGST usually operates in an all-sky scanning mode. The LAT instrument, on board the FGST satellite has a large field of view, and detects gamma-rays in the range of 20 MeV to 300 GeV. The FGST team provides daily flux measurements in multiple FGST energy-bands on a list of 23 blazars, called the "LAT Monitored source" which is publicly available at - (`http://fermi.gsfc.nasa.gov/ssc/data/policy/LAT_Monitored_Sources.html`). This list was made before FGST launch. The selection of sources in this list was motivated from historical interest in these objects. Sources have been added to this list post launch. The fluxes are available in bins of 0.3 GeV to 1.0 GeV, 1.0 GeV to 300 GeV, and 0.1 GeV to 100.0 GeV. Spectral information is not provided in these tables. Upper limits in these tables are ignored and only the measured flux points are used for this correlation study. Data is given in daily bins.

A search is made on all the ATOM data set produced by the automatic analysis pipeline, in the R-band and B-band only to find all measurements simultaneous with the FGST data points. Since FGST gives daily fluxes integrated over a 24 hour period (midnight to midnight, in UTC), and ATOM exposures are typically of the order of few tens of minutes; all ATOM exposures within a particular 24 hour period are averaged over to get a corresponding daily-average. A simple error weighted average is done. Thus the light curves and data points we consider here are insensitive to intra-day variability's in either band. Flux averaged over longer periods are not considered here.

3.2.2 Results and Discussion

The GeV and optical data are first compared by the observed fluxes in both bands and then the respective spectral indices. Only qualitative statements are made in this work.

The simultaneous R-band optical and FGST measurements for 10 sources is shown in figure 3.5, left panel. The ten sources are 3C 454.3, PKS 1510-089, 0235+164, 3C 279, 0208-512, OJ 287, PKS 2155-304, 3C 273, Mrk 421 and Mrk 501. For Mrk 421, Mrk 501, 0208-512 and OJ 287 the data is not enough to make statements on correlated variability in the optical and GeV fluxes. 3C 454.3 shows clear evidence of correlated variability in optical and the GeV band, while PKS 2155-304 and 3C 279 data shows some indication of correlation. PKS 1510-089 shows variability in both bands but does not seem to follow any trend in the overall picture. Study of individual flares in this source could shed more light. 3C 273 varies in GeV but hardly in the optical band.

Furthermore, a clear dichotomy is seen in the distribution of the points in this plot. The four sources, PKS 2155-304, 3C 273, Mrk 421 and Mrk 501 are in the bottom right corner, corresponding to high R-band flux and low LAT flux, while 3C 454.3, PKS 1510-089, 0235+164, 3C 279 and 0208-512 are in the top-left corner of the plot, corresponding to relatively low R-band flux and relatively high LAT flux. For OJ 287 a single simultaneous measurement, roughly in the middle of the two cluster of points, was obtained.

ATOM B-band measurements simultaneous with FGST data was found for 9 sources, excluding OJ 287 from the previous list, shown in figure 3.5, right panel. A similar corre-
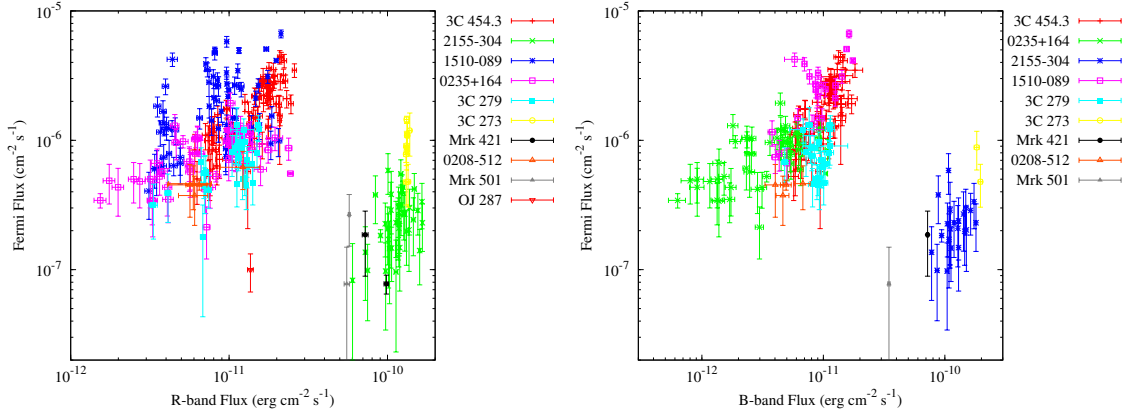
Figure 3.5: **left:** The LAT flux (from 0.1 GeV to 300 GeV) compared to the ATOM optical flux in the R-band. 10 sources listed in the text are plotted. Not all sources have equal number of points. A clear division into 2 groups is seen in the flux-flux regime. **right:** The LAT flux compared to the corresponding ATOM B-band optical flux for 9 sources. The same pattern is seen as that in the left panel.

lation in fluxes and dichotomy is seen as in the previous case. To illustrate a few examples clearly, the GeV flux versus the R-band flux for 3C 454.3 and PKS 2155-304 is shown in figure 3.6, left panel; and the same for PKS 1510-089 is shown in the right panel. 3C 454.3 and PKS 1510-089 have the maximum number of data points among the optically-faint and GeV-bright group of blazars. The characteristic correlation (or lack of correlation) is evident.

The observed dichotomy could arise from a number of reasons. This could be a purely selection effect in this small sample of sources. Considering the entire sample might fill out the region between these two clusters in flux-flux space. Note that the flux-flux plane does not a represent a physical quantity and hence the dichotomy could simply be an observational feature of a small sample. On converting the fluxes to the corresponding unbeamed luminosities will show a real division if it exists. This is however difficult without knowing the precise value of the Doppler factor and confirming that the emission in both bands are from the same region. I do not such an exercise here. Second possibility is that, we have a sample with two different subclasses of blazars. Another explanation would be a high host-galaxy optical-flux that moves a number of sources toward the right of the plots. However a correlated lower GeV flux cannot be explained
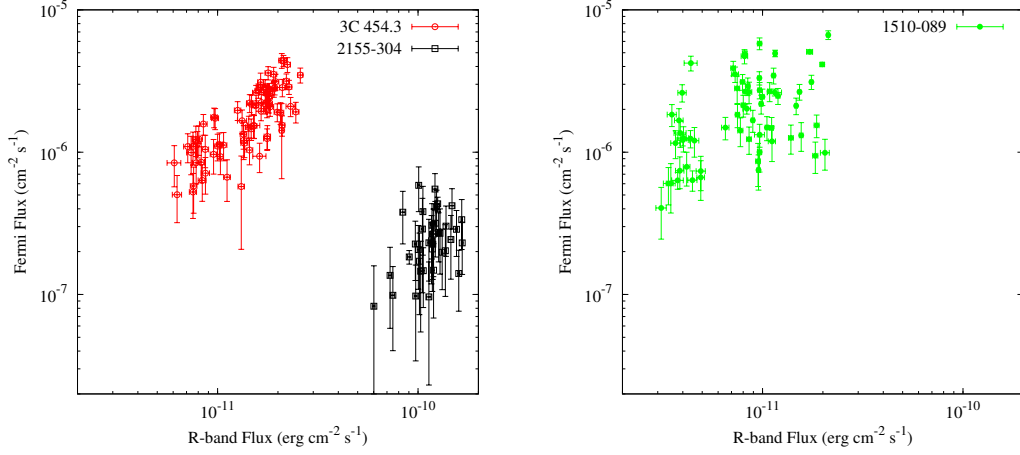
Figure 3.6: The LAT flux versus the ATOM R-band flux for individual sources. **left:** 3C 454.3 and PKS 2155-304, clearly showing the dichotomy among the two GeV-flux versus optical-flux regimes (see text), and the GeV-optical flux correlation in one source. **right:** PKS 1510-089 is the counter-example which shows a wide spread in the GeV-flux versus optical-flux plot.

away easily.

It is interesting to note that the redshift of the sources also follow this dichotomy. The optically-faint and GeV-bright blazars all have redshift greater than 0.36 (that of PKS 1510-089), where as the optically-bright and GeV-faint blazars are all nearby with redshifts less than 0.158 (that of 3C 273). Once more OJ 287 falls in the middle of these two limits with a $z \approx 0.3$.
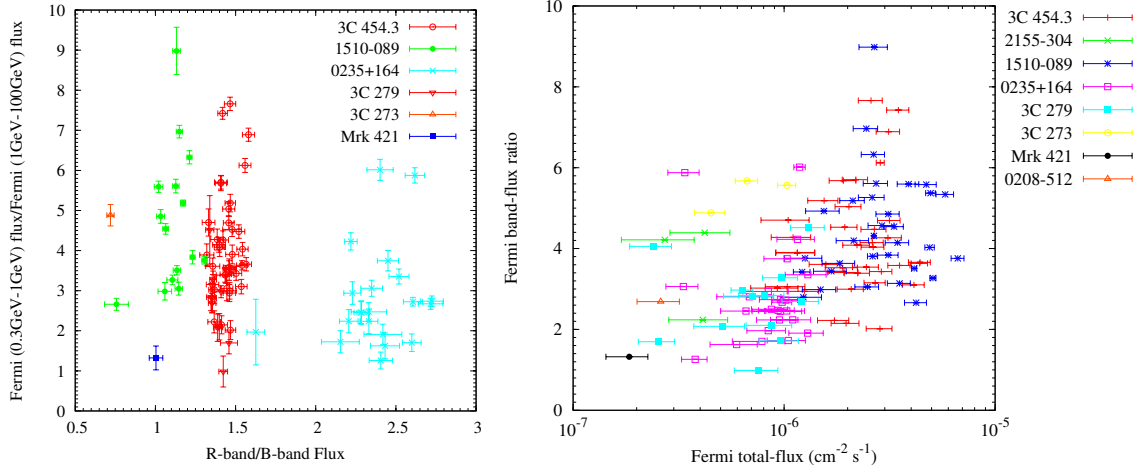
Figure 3.7: **left:** Ratio of the LAT bands (low energy band-flux over high) compared to the ratio of ATOM R-band flux to B-band flux **right:** Ratio of the LAT bands (low energy band-flux over high) compared to the total LAT flux. The error on the flux ratio is not shown.

Comparison of the spectral slopes in the GeV band and the optical wavelengths is done using the flux-ratio as the proxy for spectral-index. For LAT energies, the ratio of the flux in the low-energy band (0.3 GeV to 1 GeV) over the high energy band (1.0 GeV to 100 GeV) is used instead of the γ-ray slope; while the ratio of the R-band flux to B-

band flux is used for the slope in the optical band. The results are shown in figure 3.7, left panel. There is no clear correlation in the GeV and optical spectral index values. For individual sources, the optical flux-ratio do not scatter much, whereas there is higher scatter in the LAT flux-ratio (hence spectral-index) values. A comparison of GeV flux ratio to the total GeV flux in both bands is shown in figure 3.7 (right panel) to check any spectral softening/hardening with flux changes. There is no clear evidence of this in this sample. In other words we can conclude that the GeV spectral index varies with the GeV-flux level, whereas the optical color does not change much with optical-flux changes. A caveat should be noted that the flux ratio is not linearly related to spectral-index, hence is only a rough indicator of the later.

3.3   Testing the optical-TeV correlation in PKS 2155-304

Between August 25, 2008 and September 6, 2008 a multiwavelength (MWL) campaign on the BL Lac object PKS 2155-304 was made with HESS, FGST, RXTE and ATOM (Aharonian *et al.* 2009). The light curve for 12 consecutive days was recorded by all 4 instruments, see figure 3.8. The paper gives quantitative evidence for correlation between
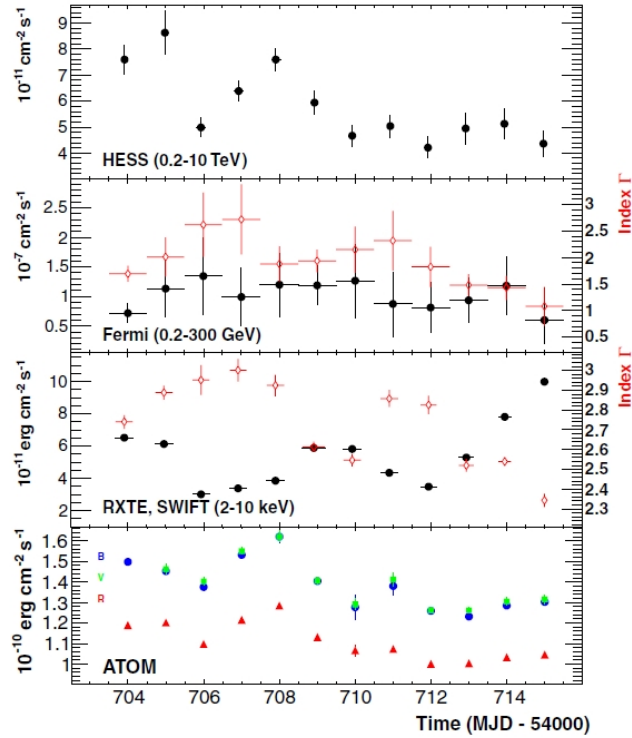
Figure 3.8: The lightcurve of PKS 2155-304 during the multiwavelength campaign of August 2008, with HESS, FGST, RXTE, and ATOM is shown (figure from Aharonian *et al.* (2009)).

the optical and VHE light curve. This correlation is quantified in terms of the *Pearson's r*,

defined as

$$(3.1) \quad r = \frac{\sum XY - \frac{\sum X \sum Y}{N}}{\sqrt{\left(\sum X^2 - \frac{(\sum X)^2}{N}\right)\left(\sum Y^2 - \frac{(\sum Y)^2}{N}\right)}}; \; or \; r = \frac{\sum z_x z_y}{N}, \; where \; z_p = \frac{P - \overline{P}}{\sigma_p}$$

In the first expression X and Y are the quantities between which *Pearson's r* (also called the sample correlation coefficient) is being calculated, and N is the sample size, i.e. the number of pairs of (X, Y) values. The equivalent expression on the right uses $\overline{P}$, the average over the parameter P and the standard deviation σ_p. The absolute value of *Pearson's r* is ≤ 1, with $+1$ denoting a perfect linear correlation and -1 for a linear correlation with negative slope. This expression is suitable for numerical calculation with a single pass over the sample. However, N should be replaced by $(N - 1)$ to maintain numerical stability for large N, i.e. to be consistent with the property that $r \leq 1$.

Since the lightcurve is in daily bins, the *Pearson's r* is sensitive only to variability timescales with duration greater than a day. The paper gives a *Pearson's r* of 0.77 to 0.86 for the flux correlation of the different optical bands with the VHE band. This high (> 0.5) positive value for the correlation coefficient is considered as a positive evidence of a true physical correlation. Having said that, it should also be noted that there is an arbitrariness in the value above which the *Pearson's r* can be considered significant. This value for any given case, depends on the accuracy of the measurements, and the characteristics of the underlying process. The former is straightforward to interpret and is proportional to the statistical errors on the measurements, which gives a spread or error in the calculated value of r. In this particular case of a light curve measurement, the second factor relates to the duty cycle of the source, which translates quantitatively to the probability of getting a given value, *Pearson's r_i*, just by chance. If the chance probability of getting a value r_i is very low, it is a strong evidence of a true correlation. Here I estimate both these effects for this source.

3.3.1   Constructing *Pearson's r* distributions

The chance probability of getting a given r_i for a pair of simultaneous lightcurve (in daily bins and a length of 12 consecutive days), can be estimated by constructing the distribution of r by correlating pairs of numerous 12-day non-simultaneous lightcurves, picked at random; then comparing the characteristics of this distribution with the value of interest, r_i.

Since R-band is the most commonly used filter with ATOM, a search in the optical R-band ATOM data was made on this source. To reduce the possible effect of a temporal offset betwen the VHE and optical band, the excluded simultaneous data consisted, in addition to the 12-day lightcurve shown in the figure, the two 12 day lightcurves obtained by shifting the time window by one day in both directions. In cases where more than 12

consecutive days of R-band data was found, as many as possible sets of 12 consecutive days were extracted from it. For example, if a 14 consecutive day lightcurve was found, 3 sets of 12-days long light curves could be extracted like so - Day 1 to Day 12, Day 2 to Day 13, and Day 3 to Day 14. In total there were 18 sets of R-band lightcurves, and all were individually correlated with the same 12-day VHE light curve of the MWL campaign. The constructed distribution of r is shown in figure 3.9, left panel. When the simultaneous R-band lightcurve and the one day shifted quasi-simultaneous lightcurves are also included in the r distribution, we get the right panel in figure 3.9.
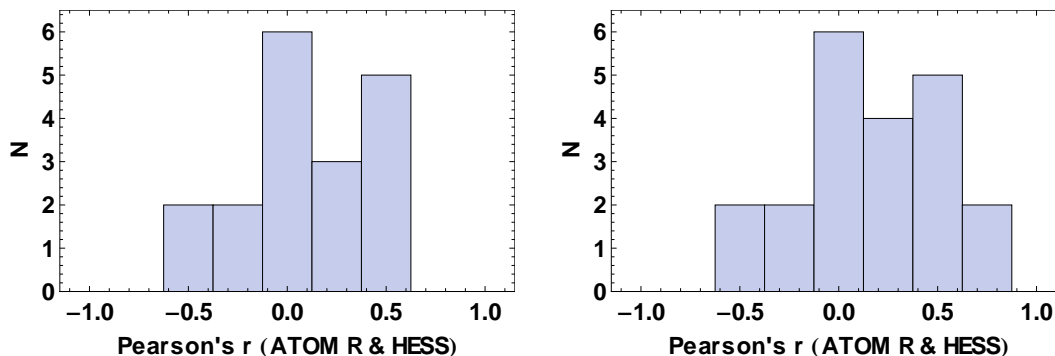
Figure 3.9: Evaluating the chance-probability of *Pearson's r*. **Left:** The distribution of 'r' obtained by excluding the 12-consecutive-days ATOM-lightcurve that are strictly contemporaneous with the 2008-MWL campaign period. *Note: This excludes three instances of 12-day-lightcurves since the 2008-MWL campaign has measurements spanning over 14 consecutive days.* **Right:** The distribution of 'r', got by calculating the Pearson's correlation between the HESS light-curve (limited to 12 consecutive days) during the MWL-campaign, with all 12-(consecutive)-day lightcurves in the ATOM-R band. *Note: The ATOM set of light curves include the contemporaneous data during the 2008-MWL campaign, as well as non-contemporaneous archival ATOM data.*

For PKS 2155-304, from all the ATOM data taken so far, we know that the R-band and the B-band fluxes are correlated. It is instructive to construct a r distribution between these two optical bands which are known to have a correlation. This can act as a control experiment for checking the effect of the duty cycle and the measurement error in the optical band on chance correlations. The results are shown in figure 3.10.

These distributions have small sample size, though the essential characteristics still stand out. In principle a similar distribution can be made by taking all the pairs of 12 day long R-band lightcurves in the entire ATOM data on this source, and finding r for these, i.e. correlating the R band flux with itself. Figure 3.11, shows these distributions. The left panel is obtained by excluding the correlations of those light curves that lie within a ± 4 days overlapping period, while the right panel includes all pairs, meaning every light curve is correlated with itself as well.

The distributions obtained here are representative of the *Pearson's r* distribution for 12-day long lightcurves in this particular source. Interpretation is made in section 3.3.3 following a study of the effect of measurement errors.
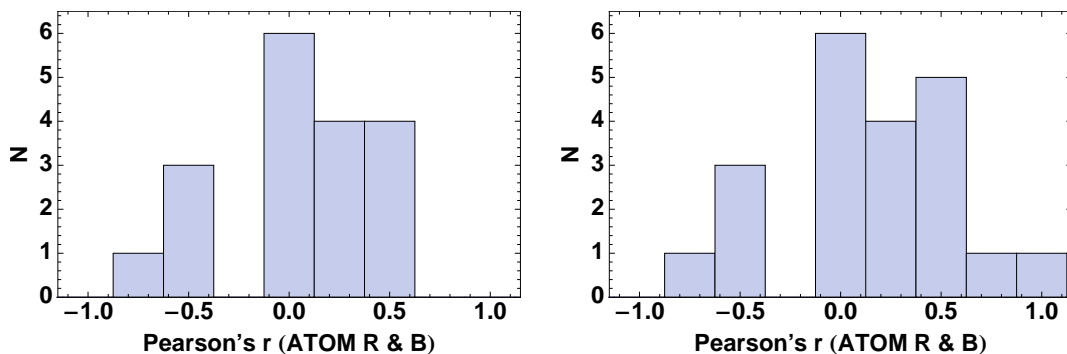
Figure 3.10: **Left:** The distribution of *Pearson's r*, obtained by correlating the B-band ATOM-12-consecutive-days lightcurve with all the sets of 12-consecutive day R-band lightcurve, excluding the strictly contemporaneous data sets of the 2008-MWL campaign. **Right:** The same as left but including the contemporaneous data sets.
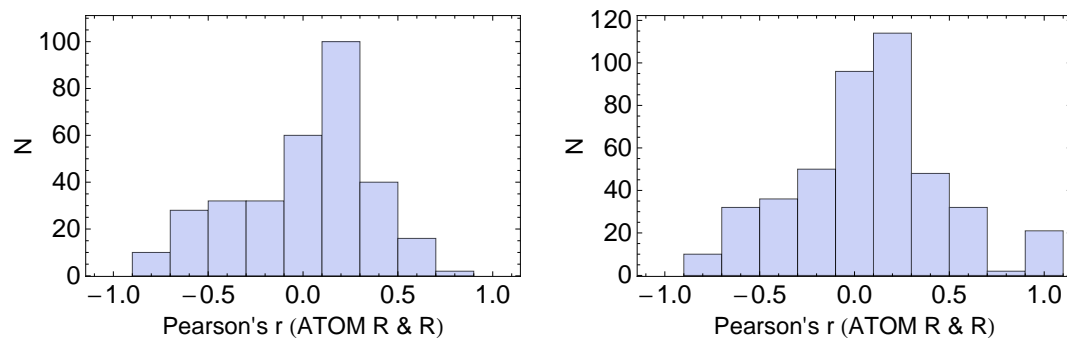
Figure 3.11: **Left:** The distribution of *Pearson's r*, obtained by correlating the R-band ATOM-12-consecutive-days lightcurve with all the sets of 12-consecutive days lightcurves in the same R-band, excluding the lightcurves overlapping within a ±4 day period. **Right:** The same as left but including all the R-band lightcurves.

3.3.2   Effect of VHE measurement errors

From figure 3.8, it is clear that the fractional error in the VHE band will be the dominating contributor to the error on the calculated *Pearson's r*, thus in this section errors on the optical fluxes are neglected. To estimate this error on r, the 12-day VHE and R-band lightcurves of the MWL campaign was taken and the best-fit linear relation in $Log[Flux_{(VHE)}]$ and $Log[Flux_{(R-band)}]$ was calculated. This was assumed to be the true underlying correlation between the VHE and optical fluxes, and a synthetic 12 day VHE lightcurve was generated from the fit, taking the R-band measurements as the true optical flux values for the source. To get a range of VHE fluxes that could be obtained within the accuracy of the HESS instrument, given this R-band lightcurve, two extreme VHE fluxes for each day was obtained by taking the error of each true VHE flux point for the corresponding day number. This gives three VHE points for each R-band flux, and in all gives us $3^{12} = 531441$ VHE light curves. Since the error bars on the VHE light curve are not of equal value and this simple approach gives big number of VHE lightcurves, there

is no need for a more complicated MonteCarlo simulation to generate VHE lightcurves. The distribution of the *Pearson's r* for these with the R-band MWL lightcurve is shown in figure 3.12. Note that there are hump like features in the overall distribution as a result of
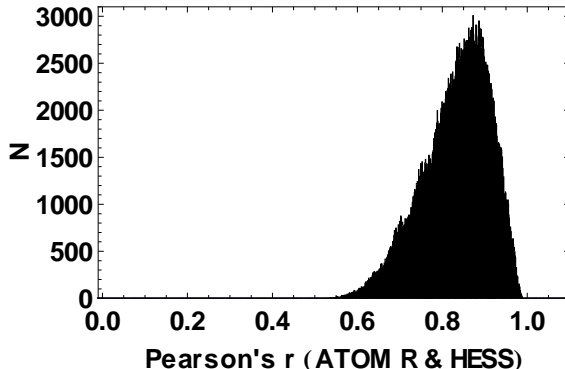
Figure 3.12: Under the assumption that there exists a true correlation between VHE flux and the optical band - the dispersion in Pearson's 'r' due to the measurements uncertainties (assumed to be solely due to the HESS uncertainties), is evaluated using roughly half a million simulated HESS light curves of 12 days length - correlated with the 12 day ATOM R-band lightcurve during the 2008-MWL campaign.

the approximate method used here to generate the VHE lightcurves. However these are not so prominent and the distribution is fairly smooth to serve our purpose. The peak of the distribution is ≈ 0.875 and the FWHM is ≈ 0.175. This is clearly an unsymmetrical distribution.

3.3.3 Discussion and Conclusion

Before interpreting the results obtained here, it is worthwhile to consider what we expect a *Pearson's r* distribution to look like. The values *Pearson's r* can take is between -1 and +1. It is thus expected that a distribution of r values generated from randomly selected non-simultaneous light curves of a fixed length will peak at zero, as no correlation is expected between these. The width of the distribution depends on the error in the measurements and the duty cycle of the source. High duty cycle means there is higher chance that any two randomly picked non-simultaneous lightcurves might catch flares in the source giving a large value for r (can have either sign), thus broadening the distribution. If the duty cycle of the source is low and the length of the lightcurve is large compared to the characteristic variability timescale, a true correlation caused by an isolated flare is expected to stand out from the r distribution generated from randomly selected non-simultaneous light curves.

The distributions obtained in section 3.3.1 do show a peak at $r = 0$. However both the VHE versus R-band as well as B-band versus R-band distributions are rather broad. From the distributions in the left panels of figures 3.9 and 3.10 a value of the width (or FWHM) cannot be clearly ascertained. The size of these distributions is not very large however the distinctive features of a peak at 0 and a wide distribution in the range is

evidently characteristic of this particular source. This is because the distribution of R and B bands which have very low measurement error, but still shows these features, meaning that the errors cannot be responsible for such a broad spread. Since R and B band are in fact correlated in this source for simultaneously measured light curves, the width is due to the high duty cycle of the source.

From figure 3.11, for correlation of the R band with itself the sample size is large enough to give a good coverage with a similar binning as in the other figures of section 3.3.1. The left panel (which excludes overlapping light curves) clearly shows an unsymmetrical distribution, with peak around 0.2 instead of 0. The distribution rapidly falls on both sides of the peak, but has a long tail towards negative values. The right panel is similar except the bin at $r = 1$ which is now populated with the 21 values obtained from the autocorrelation of the 21 sets of 12 day long light curves. The broad distribution is again similar to the r distribution of R with VHE and R with B, and is therefore an universal characteristic of this particular source. This distribution cannot be directly compared to the r distribution of the correlation of the VHE and R band, because the characteristic fluctuations in VHE might be different from the R-band. In fact this is what is intended to discover from this exercise.

The peak is not centered at 0, but at +0.2, which can be attributed to the characteristic fluctuations of this source in this waveband.

Looking at the right panel of the figures in section 3.3.1, it is seen that the exactly simultaneous sets of lightcurves fall into the highest value bins, $r \approx 0.8$ for R-band with the VHE, $r \approx 1$ for R-band with the B-band, and exactly $r = 1.0$ for the autocorrelation in R. The r distributions with and without the simultaneous (contemporaneous) lightcurves are consistent with each other. However, the high positive r values for the exactly simultaneous sets do fall into the extreme positive bins. For this source a precise critical r value that separates the chance distribution from the true distribution cannot be determined. Thus it cannot be ruled out that the highest values cannot occur simply by chance.

From figure 3.12 in section 3.3.2, the FWHM of ≈ 0.175 is as an estimate of the error in r due to the measurements errors of the lightcurves.

Thus the *Pearson's* r of $r \approx 0.8$ for the correlation between the VHE and optical R-band during the 2008-MWL campaign on PKS 2155-304 is consistent with what we expect from a true correlation as shown in figure 3.12, within the error on r for a true correlation. The data set here shows a quantitative evidence of a correlation in the VHE and optical light curve in the source PKS 2155-304. Having this value purely by chance, however cannot be ruled out, from the various characteristic r distributions we get for this source.

Connecting the GeV and TeV bands of blazars

Blazars have been detected in γ-rays in a broad range of frequencies. The EGRET (Energetic Gamma-Ray Experiment Telescope) instrument on the CGRO (Compton Gamma Ray Observatory) detected a number of blazars at energies $> 100\,\mathrm{MeV}$ (with the highest energy photons at $\sim$ few GeV)[1]. The 3rd EGRET catalog Hartman *et al.* (1999), gives the spectra of 66 blazars. In addition to these "there were 27 lower confidence potential blazar identifications" in this catalog. The Fermi Gamma-ray Space Telescope (FGST) group, has published a list of 104 bright AGNs called the LAT Bright AGN Sample (LBAS), Abdo *et al.* (2009a) from the first three months of sky-survey done with the Large Area Telescope (LAT). In the VHE-band, remarkable advances in the field of ground based γ-ray astronomy in the last two decades, has resulted in the detection of more than 25 VHE blazars, and still counting. Catalogs of VHE sources are currently maintained at the following websites: The VERITAS groups' TeVCAT, http://tevcat.uchicago.edu/, and the MAGIC group maintained catalog at www.mppmu.mpg.de/$\sim$rwagner/sources/. No simultaneous measurements of blazar SED in γ-rays at MeV to TeV energies had been made prior to 2008. The emission component in blazars spanning these energies has not been unambiguously explained. To describe the emission, both leptonic (electron/positron synchrotron emission followed by and inverse-Compton scattering on a photon field) as well as hadronic models (proton-synchrotron and particle decay) are still in contention.

The launch of the Fermi-Gamma-ray-telescope (FGST), has opened up the opportunity for doing simultaneous multi-wavelength measurements of blazars overlapping the MeV-TeV bands. While FGST scans the entire sky on a daily basis, and provides GeV flux and spectral information on blazars - the VHE flux level of most blazars pose a challenge to the sensitivity of current IACT experiments. Thus relatively long exposure times (of the order of 10s of hours) are required to detect blazars in the VHE regime. In addition IACTs have a small field of view, compared to GeV gamma-ray satellite telescopes. An all sky survey with a deep exposure is thus not technically feasible using current installations. Therefore it is necessary to adopt some selection procedure to chose candidate VHE blazars to be observed with IACT experiments. Selecting blazars with high X-ray and radio fluxes for TeV observations Costamante & Ghisellini (2002) has been successful

---

[1]The energy range accessible to γ-ray satellite experiments, i.e. between roughly $100\,\mathrm{MeV}$ to $100\,\mathrm{GeV}$, is referred to as the GeV energy band throughout this work

in discovering new TeV blazars. According to this approach the nonthermal emission of HBLs are dominated by the synchrotron emission in the X-ray band and the VHE part of the SED is the IC emission of the electrons producing the X-rays. In this chapter it has been attempted to select blazars that are likely to be bright in TeV energies, from those already detected in the MeV-GeV band.

4.1 Selection strategy for candidate VHE blazars from GeV bright blazar samples

According to the leptonic scenario, the GeV and VHE emission of blazars are physically connected, since both these components arise from the IC emission of one and the the same electron distribution. This would imply that the spectra in the MeV-GeV regime is correlated to the spectra at TeV energies. From a purely observational point of view - the GeV spectrum and the VHE spectrum of most blazars are well described by powerlaws. Since most VHE blazars show no sign of a spectral cut-off, to first order it is assumed that the GeV spectra extends into the VHE regime. The observed VHE spectrum is this extrapolated spectrum that has been modified due to EBL absorption. Thus GeV blazars, that are bright and have a hard spectra are likely to be bright in VHE. The 3rd EGRET catalog gives the average state of blazars over a four and half year period. I look at this catalog as well as the LBAS which gives a more recent list, to select VHE candidate sources.

The selection strategy is based on the VHE brightness of the extrapolated GeV spectra of each source from a preselected GeV bright subsample. A limit on the maximum redshift and the maximum spectral slope are used as the pre selection criteria. Each of the resulting source is then corrected for EBL extinction. The optical depth as a function of VHE photon energy and the source redshift, $\tau(E_{TeV}, z)$ is calculated using the EBL model in Aharonian *et al.* (2006b)[2]. This EBL model is derived from actual VHE observations assuming a theoretically hardest intrinsic spectra and is hence an upper limit on the EBL. The extrapolated spectra is attenuated by the extinction factor, $(e^{-\tau})$ to obtain the predicted spectra which can be observed in VHE (see figure 4.1). The integral flux of the EBL corrected spectra is compared with the HESS sensitivity (as a prototype for current generation of IACTs) to extract promising candidates for VHE observation.

4.1.1 EGRET blazars suitable for VHE observations

From the 3rd EGRET catalog Hartman *et al.* (1999), AGN were selected that are relatively nearby (redshift, z < 0.6) and have a hard spectral index ($\Gamma \leq 2.5$). The integral flux of the extrapolated EBL corrected VHE spectra is calculated as described above. Our

---

[2]referred to as the "Aharonian-2006" EBL model, hereafter
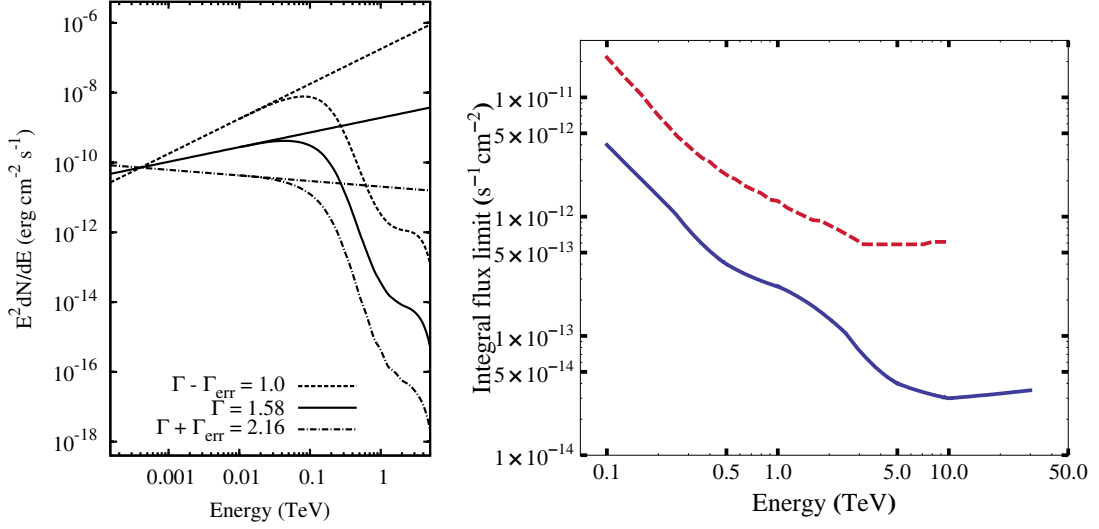
Figure 4.1: ***Left:*** Shown here is 3EG J0852-1216. Straight lines are extrapolations from EGRET values with the upper and lower lines reflecting the errors on the spectral index. Curves are the respective attenuated spectra due to EBL absorption. The area under the middle curved line (between $\approx 0.17\,\mathrm{TeV}$ and $\approx 10.0\,\mathrm{TeV}$) gives the estimated brightness, used for the ranking in Table 6.1.***Right:*** The sensitivity for the HESS array in units of integral flux. The red dashed line is for a 10 hours exposure, and the blue solid curve is for a 50 hour exposure. In both cases the integral flux is the minimum required for a 5σ detection and least 10 events. A crab photon index is chosen for the sources spectra.

calculations show that for almost all VHE blazars which have EGRET spectral measurements, such an extrapolation is rather conservative (for example, see figure 4.2, left panel).
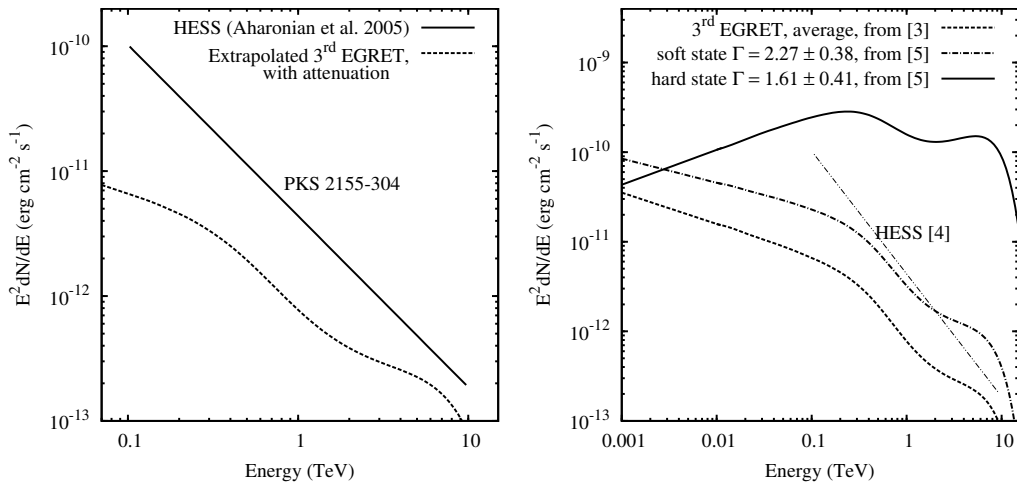
Figure 4.2: **Left:** Shown here is the power law fit (solid line) to the measured spectra of PKS 2155-304 (HESS observations in Oct-Nov 2003 Aharonian *et al.* (2005b)) of a low state of this object. But as seen in the plot it is well above the extrapolated EGRET spectra (dashed line). **Right** The high variability in the spectral index as well as the flux level of blazars can cause significant differences in the extrapolation of GeV spectra to TeV energies. Three EGRET states of PKS 2155-304 are shown along with HESS observations.

The fluxes and spectral indices from the 3rd EGRET catalog used for this work, and the results of the extrapolations are given in table 6.1. It should be noted that blazars are usually variable in GeV, hence the extrapolations can change dramatically, resulting in quite different fluxes in VHE (see figure 4.2, right panel).

Table 4.1: Candidate ranking based on the expected VHE flux. Shown here are the 3rd EGRET flux (6th column) and spectral indices (column 4), the estimated VHE flux (7th column) taking Γ as the spectral index. The $*$ at the end of common names denote blazars already detected in VHE energies

(1) Rank	(2) 3EG-Name	(3) z	(4) Γ	(5) Γ_{err}	(6) F_{3EG} ($>$ 100MeV) 10^{-8} /cm^2/s	(7) Integral Flux 10^{-12} /cm^2/s	(8) Other-Names
1	J1104+3809	0.031	1.57	0.15	13.9	1168.2	Mrk 421*
2	J1222+2841	0.102	1.73	0.18	11.5	194.9	W Comae*
3	J0852-1216	0.566	1.58	0.58	44.4	56.5	PMN J0850-1213
4	J1255-0549	0.538	1.96	0.04	179.7	27.4	3C 279*
5	J1009+4855	0.200	1.90	0.37	5.7	17.4	1ES 1011+496*
6	J1605+1553	0.357	2.06	0.41	42.0	16.4	4C +15.54
7	J2158-3023	0.116	2.35	0.26	30.4	7.21	PKS 2155-304*
8	J0853+1941	0.306	2.03	0.35	10.6	7.16	OJ+287
9	J0222+4253	0.444	2.01	0.14	18.7	5.04	3C 66A*
10	J0958+6533	0.368	2.08	0.24	15.4	4.86	0954+658
11	J0721+7120	0.300	2.19	0.11	17.8	4.42	0716+714
12	J2202+4217	0.069	2.60	0.28	39.9	2.2	BL Lacertae*
13	J0204+1458	0.405	2.23	0.28	23.6	2.14	4C +15.05
14	J0530-3626	0.055	2.63	0.42	31.9	1.51	0521-365
15	J0828+0508	0.180	2.47	0.40	16.8	1.33	0829+046
16	J1517-2538	0.042	2.66	0.43	28.2	1.15	1514-241
17	J1324-4314	0.002	2.58	0.26	13.6	1.11	Cen A*
18	J0416+3650	0.049	2.59	0.32	12.8	0.81	3C 111

The selected GeV sources were ranked according to their predicted observed-integral-flux between ≈ 0.2 TeV to ≈ 10.0 TeV, and the top 18 objects are presented in table 6.1. Sources with extrapolated integral flux (7th column of table 6.1) greater than 10^{-12} /cm^2/s are above the integral flux sensitivity above ≈ 100 GeV of the HESS array, for a 5σ detection in 50 hours (figure 4.1, right panel - the blue curve). Since at this energy all current generation IACT arrays have similar sensitivity, these sources can thus be detected with Cherenkov telescopes like HESS, MAGIC and VERITAS. In fact, eight of these are already established VHE sources.

A subset of the sources that had declination less that $20°$ and passed the VHE detection criteria were proposed for observations to the HESS collaboration. It was decided by the HESS observing committee, in 2007, that these sources would be observed only on GeV flares detected with the FGST, as Trigger of Opportunity (ToO) sources.

4.1.2 Fermi LAT bright AGN sample

The LAT instrument on the FGST is designed to measure blazar spectra from $20\,\text{MeV}$ to $300\,\text{GeV}$, with a sensitivity of $\sim 10^{-9}\,/\text{cm}^2/\text{s}$. The LAT sensitivity is higher than that of the EGRET instrument. It is thus able to detect fainter blazars in shorter exposure times. The LBAS, Abdo *et al.* (2009a) consists of 106 source which have high-confidence associations of with known AGNs. It contains 104 blazars of which 58 are FSRQs, 42 are BL Lac objects, and 4 blazars are with uncertain classification. In addition it has two radio galaxies, Centaurus A and NGC 1275. The LBAS gives the integral flux between $100\,\text{MeV}$ and $100\,\text{GeV}$ and the spectral index (derived from a power law fit between $200\,\text{MeV}$ and $100\,\text{GeV}$) for all sources. A search for the redshift of all sources in the available literature yielded redshift measurements for 92 objects.

Table 4.2: The list of candidates for VHE obs. chosen from LBAS.

FGST Name	RA	dec	z	F$_{100}$	Γ_{Fermi}	I(> 0.2TeV)	Other Name
				$(10^{-8}/\text{cm}^2/\text{s})$		$(10^{-12}/\text{cm}^2/\text{s})$	
0FGL J1104.5+3811	166.137	38.187	0.030	15.3 ± 1.1	1.77 ± 0.04	349.	Mrk 421*
0FGL J2158.8-3014	329.704	-30.237	0.116	18.1 ± 1.2	1.85 ± 0.04	137.	PKS 2155-304*
0FGL J1653.9+3946	253.492	39.767	0.033	3.1 ± 0.6	1.70 ± 0.09	115.	Mrk 501*
0FGL J1053.7+4926	163.442	49.449	0.140	0.5 ± 0.3	1.42 ± 0.20	56.6	MS1050.7+4946
0FGL J1218.0+3006	184.517	30.108	0.130	9.7 ± 1.1	1.89 ± 0.06	51.1	B2 1215+30
0FGL J1719.3+1746	259.830	17.768	0.137	6.9 ± 0.9	1.84 ± 0.07	49.5	PKS 1717+177
0FGL J1015.2+4927	153.809	49.463	0.212	4.9 ± 0.7	1.73 ± 0.07	47.2	1ES 1011+496*
0FGL J2000.2+6506	300.053	65.105	0.047	4.2 ± 1.0	1.86 ± 0.11	44.6	1ES 1959+650*
0FGL J1221.7+2814	185.439	28.243	0.102	8.3 ± 1.1	1.93 ± 0.07	38.6	W Comae*
0FGL J2009.4-4850	302.363	-48.843	0.071	2.9 ± 0.9	1.85 ± 0.14	28.6	PKS 2005-489*
0FGL J0320.0+4131	50.000	41.524	0.018	22.1 ± 1.9	2.17 ± 0.06	27.6	0316+413
0FGL J1517.9-2423	229.496	-24.395	0.048	4.1 ± 1.2	1.94 ± 0.14	24.1	AP Lib
0FGL J0449.7-4348	72.435	-43.815	0.205	12.0 ± 1.3	2.01 ± 0.06	17.6	PKS 0447-439
0FGL J0222.6+4302	35.653	43.043	0.444	25.9 ± 1.6	1.97 ± 0.04	8.79	3C 66A*
0FGL J0722.0+7120	110.508	71.348	0.310	16.4 ± 1.4	2.08 ± 0.05	7.52	S5 0716+71*
0FGL J0507.9+6739	76.985	67.650	0.416	1.7 ± 0.8	1.67 ± 0.18	5.36	1ES 0502+675
0FGL J2202.4+4217	330.622	42.299	0.069	8.5 ± 1.8	2.24 ± 0.12	4.9	BL Lacertae*
0FGL J0303.7-2410	45.940	-24.176	0.260	3.8 ± 0.9	2.01 ± 0.13	3.96	PKS 0301-243
0FGL J1751.5+0935	267.893	9.591	0.322	18.4 ± 2.1	2.27 ± 0.07	2.04	OT 081
0FGL J1512.7-0905	228.196	-9.093	0.360	55.8 ± 3.3	2.48 ± 0.05	1.05	PKS 1510-089

A subset of these objects, excluding sources with a relaxed $z_{max} < 1.0$ (since this is a more recent sample) was used for selecting candidate sources for VHE observations. The same strategy as the previous section was used to estimate the observable VHE spectra, i.e. simple extrapolation of the GeV spectra to VHE with correction for EBL absorption.

The Integral flux of the extrapolated spectra, gives an indication of the flux that would be seen using the current generation of IACTs such as VERITAS, H.E.S.S., and MAGIC. Requiring an integral flux above $200\,\text{GeV}$ greater than $10^{-12}\,/cm^2/s$, for a $5\,\sigma$ detection in $50\,\text{hours}$, a list of candidates ranked by their VHE integral flux is presented in table 4.2. In the table, F$_{100}$ is the LBAS flux in the $1\,\text{GeV}$ to $100\,\text{GeV}$ band. Γ_{Fermi} (also from LBAS) is the spectral index derived from a simple power law fit between $0.2\,\text{GeV}$

and 100 GeV. Candidates having $I(> 0.2\,\text{TeV}) > 10^{-12}/cm^2/s$ are listed here. The asterisk after the common names of some blazars, denotes that these are already established VHE emitting blazars. The fact that there are ten VHE emitters in this list of twenty predicted VHE emitters, gives support to this selection method.

4.1.3 LAT triggers for VHE follow up observations

The FGST orbits the earth once in 90 minutes, and in its sky-survey mode can scan the entire sky in three hours. In the first year of operations, flux values for a list of sources (called the "LAT monitored sources") was made publicly available with a latency of about a day. As of August 25, 2009 all LAT data is publicly available. Since we expect a correlation between the GeV and VHE brightness, it is useful to have a set of criteria that allows us to decide whether VHE follow-up of GeV flares will lead to detections. This would allow us not only to catch flares from known VHE sources, but also to discover new VHE blazars.

It is planned by ground-based Cherenkov telescope groups and the FGST group to have dedicated simultaneous observations of some known VHE blazars. However it is necessary to increase the VHE source sample, to identify spectral features universally present in γ-ray bright blazars to build a collective model. Search for VHE blazars following the strategy in Costamante & Ghisellini (2002) is biased towards the HBL class, resulting in a VHE sample consisting mostly of HBLs. However FSRQs are bright GeV sources and it is interesting to explore this class at VHE energies. Following up of GeV flares, especially of FSRQs is a mechanism to pick up states that might also be VHE bright. Also some blazars (e.g. 1ES 1101-232) have been detected only during their bright states.

The trigger criteria for TeV experiments from LAT flares is on the estimated source brightness in VHE. This estimate is based on an extrapolated spectra from GeV to VHE and thus depends on the GeV spectra characteristics and the source redshift. Since most GeV spectra of blazars are well described by simple powerlaws, the spectral shape is defined by the two parameters viz. the normalization and photon-index, or equivalently the integral flux (assuming a powerlaw) and a photon-index. The redshift dependence is due to the EBL correction required in the VHE regime. The trigger criteria can then be represented as regions in the integral-flux versus photon-index plane, where the GeV brightness corresponds to VHE detectable flux for a specified redshift. Figure 4.3 shows this trigger criteria for a number of redshifts. The region lying above a given line corresponding to a specific redshift, gives the GeV source characteristics for an extrapolated VHE spectrum that lies above the sensitivity of IACT experiments. The FGST integral flux is given in flux above 100 MeV.

This result was submitted as a ToO proposal to the HESS collaboration, and ac-
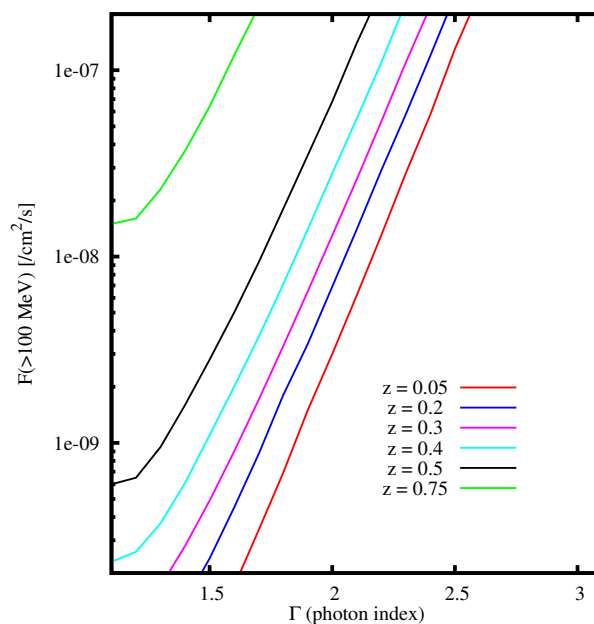
Figure 4.3: The minimum LAT flux (greater than 100 MeV) required, at a measured photon index to have a corresponding flux in the energy range of 0.2 TeV to 10 TeV greater than 10^{-12} /cm^2/s is shown for various source redshifts. Sources with LAT fluxes above the line corresponding to the redshift of the blazar would be in a flaring state and hence would be detectable using Cherenkov telescopes like HESS, MAGIC and VERITAS.

cepted, with a simplified criterion of $I(>100\,MeV) > 10^{-6}/cm^2/s$ and $z < 0.5$, for having ToO observations. Initial observations were to be of 4 hours durations, which could be followed up with additional time in case of continuing high-state at GeV energies, or an indication of brightness in the VHE regime. Two such observations from ToO from FGST flares are reported in chapter 5. Sources with $z > 0.5$, could also be observed if there were exceptionally bright flares that imply a VHE flux above the instrumental sensitivity.

4.2 Checking the prediction strategy

The extrapolation from GeV to TeV can be tested in two ways -
1) by comparing if archival GeV and VHE data are compatible within the average measurements, and
2) by measuring the simultaneously measured SED from MeV to TeV energies.

4.2.1 Archival VHE data of GeV-blazars

For all VHE blazars that appear in the LBAS or the 3rd EGRET catalog, the comparison of the extrapolated, EBL-corrected spectra against the measured VHE spectra is made (see figure 4.4 and 4.5). For VHE measurements the fits to the differential flux are shown. Eight of the ten sources shown have the GeV extrapolations crossing the VHE measurements.
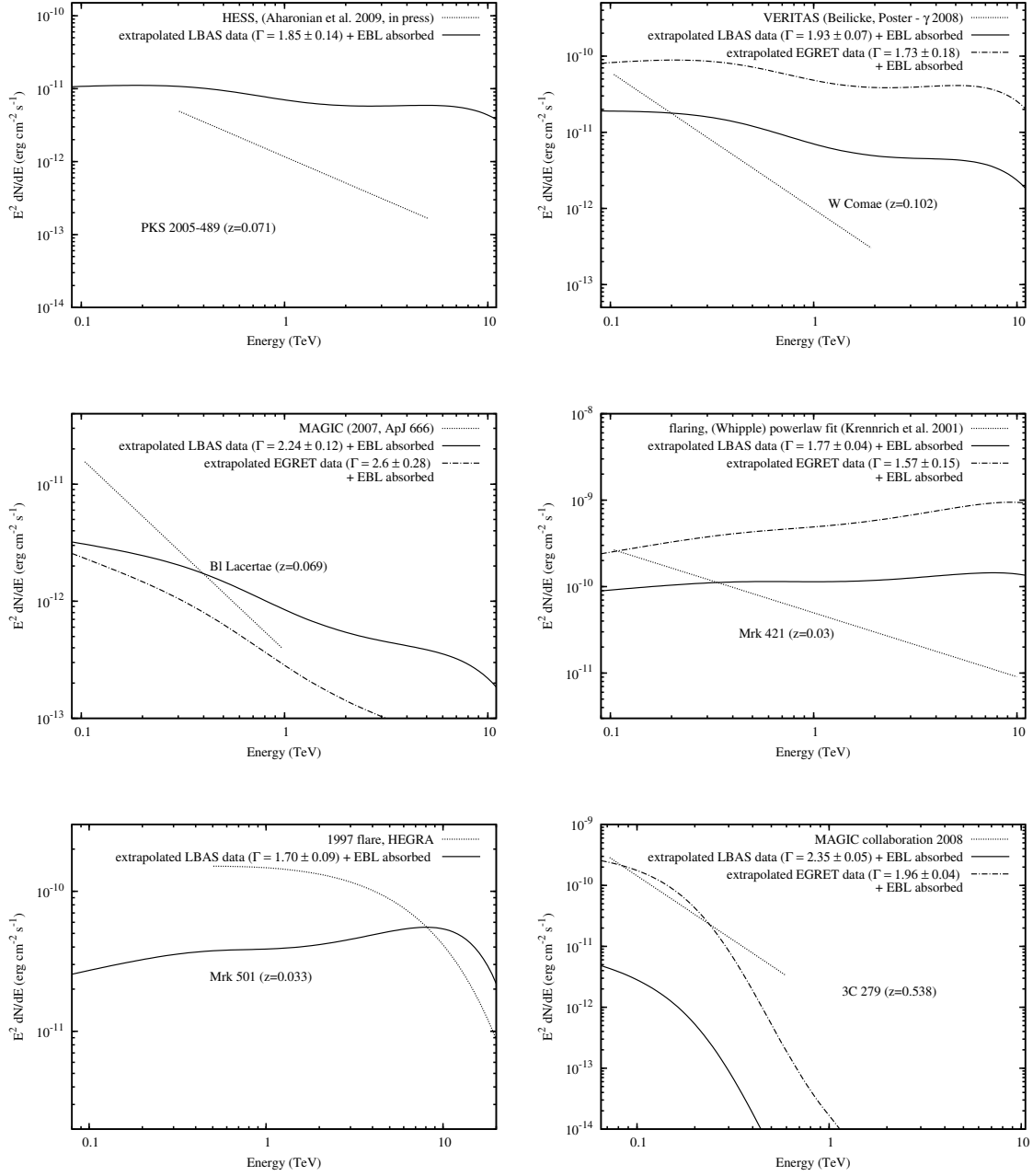
Figure 4.4: Comparison of the extrapolated and EBL-absorbed GeV spectra, calculated from the LBAS and the 3rd EGRET catalog (where available), with VHE measurements. The VHE measurements are shown in terms of the fits to the actual flux points, and are drawn between the energy ranges within which the fits are valid. Except for PKS 2005-489 the GeV extrapolations for all sources cross the VHE spectra (also see figure 4.5) . This shows that the extrapolations broadly agree with the VHE measurements.

Apart from PKS 2155-304 none of the VHE measurements are simultaneous with the GeV measurements. Since blazars are known to be variable, and the extrapolation from $\sim 100\,\mathrm{MeV}$ to $\sim 1\,\mathrm{TeV}$ covers 4 decades in energy, the fact that most of the extrapolations cross the VHE spectra shows that they are compatible in general.
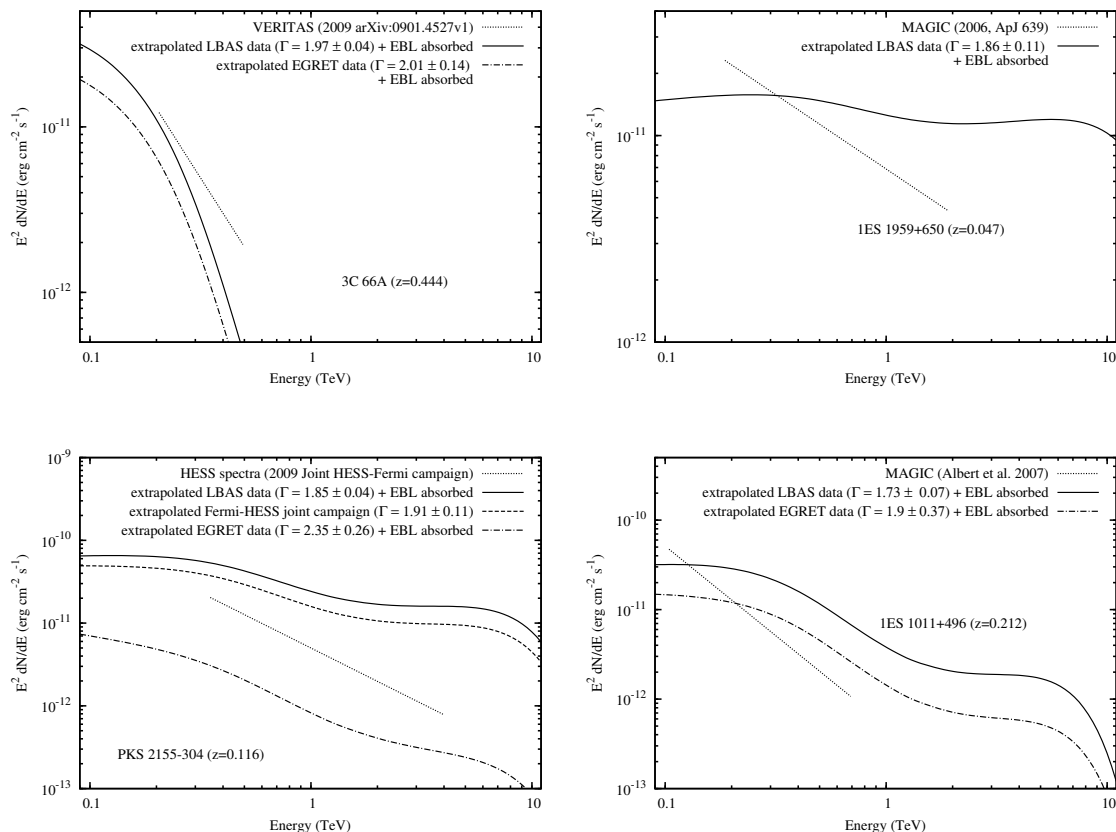
Figure 4.5: Comparison of the extrapolated and EBL-absorbed GeV spectra with VHE measurements (see figure 4.4). In the case of 3C 66A both the LBAS and the EGRET extrapolations underestimate the VHE measurements. Apart from this, all sources are in general compatible.

4.2.2 Simultaneous GeV and VHE observations

At the time of writing this thesis there were two published instances of simultaneous SED measurement of blazars with the LAT instrument and IACT arrays. LAT observed PKS 2155-304 with the HESS array (Aharonian *et al.* 2009) along with RXTE in X-rays and ATOM in optical; and 3C 66A with the VERITAS array (Reyes 2009).

The PKS 2155-304 campaign between August 25, 2008 and September 6, 2008, give the first simultaneous spectra from GeV to TeV energies of a blazar. The LAT spectra during the campaign is well described by a powerlaw. To increase photon statistics the GeV data extended over a longer period with a similar average flux state, shows a clear break at 1 GeV (see figure 4.6, left panel). To be consistent with the strategy used in this work, I used the strictly simultaneous powerlaw fit to the GeV data for the extrapolation from GeV to VHE band. The EBL absorption is accounted for using the Aharonian-2006 model as before. Furthermore, to compare with other EBL models, the EBL correction is also shown for two models in literature that give the very low and very high attenuation and the Aharonian-2006 model, which gives moderate extinction. These two extreme

models are the fiducial model from Gilmore *et al.* (2009)[3] and the best-fit model in Stecker *et al.* (2006)[4] respectively. The extrapolations are done using the FGST GeV slope, and the minimum and maximum possible slopes within the error on this measured. Thus the softest spectra (with slope $\Gamma_{GeV} + \Delta\Gamma_{GeV}$) is corrected with the maximum possible extinction, given by the Stecker-2006 model. While the hardest spectra (with the slope of $\Gamma_{GeV} - \Delta\Gamma_{GeV}$) is corrected using the minimum possible extinction, Gilmore-2009 EBL model. This resulting range of extinction corrected extrapolations, indicate the uncertainty in the EBL level. The right panel of figure 4.6 shows these extrapolations along with the HESS measured flux points. The error bars are statistical errors only. The VHE data is marginally consistent with the extrapolations. However as we noted before there is evidence of a break in the extended GeV data, while we are taking the single powerlaw fit to the simultaneous data. Thus it is concluded that such a break actually exists in the GeV spectra and is the reason for the bad match of the extrapolation with the VHE flux points.
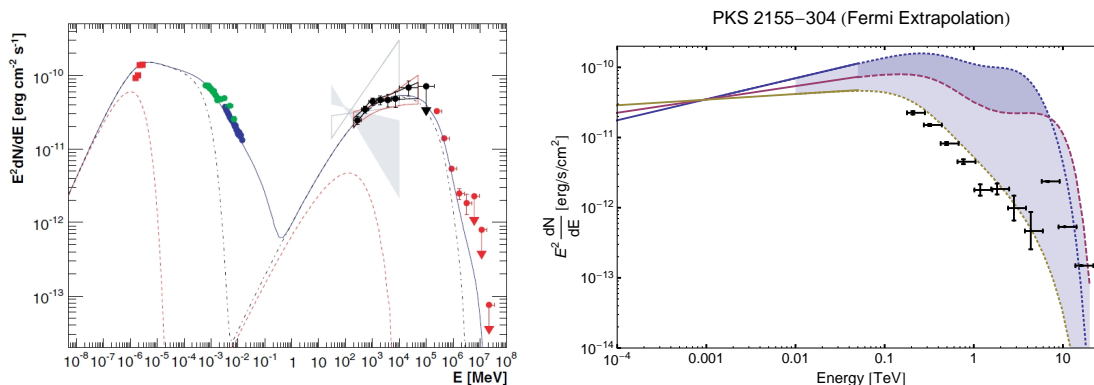
Figure 4.6: ***left:*** The multi wavelength data from Aharonian *et al.* (2009)with the SSC model fits. Note the clear break in the GeV spectra at ≈ 1 GeV. ***right:*** The extrapolation from the GeV measurements within the error on the GeV photon index and the uncertainty in EBL is shown here. The three extrapolations correspond to the measured spectral index Γ_{GeV} and the hardest and softest slope within the errors, i.e. $(\Gamma_{GeV} - \Delta\Gamma_{GeV})$ and $(\Gamma_{GeV} + \Delta\Gamma_{GeV})$ respectively. The hardest spectra was corrected using the Gilmore-2009 EBL model (minimum extinction), the softest with Stecker-2006 model (maximum extinction) and the extrapolation of the measured spectral slope with the Aharonian-2006 model. The data points are the HESS VHE measurements.

VERITAS detected a strong flare from 3C 66A in October 2008 (Reyes 2009). This happened to coincide with a GeV flare recorded with FGST. The resulting measurements and the SSC model fits are shown in figure 4.7, left panel. Similar to the previous case of PKS 2155-304 the extrapolated GeV spectra corrected for EBL extinction is shown in the right panel of the figure. The GeV flare spectra measured with FGST is used for the extrapolation. In this case the measured VHE flux is shown as the powerlaw fit to the VERITAS data (red solid line). In this case the extrapolations match the measured VHE

---

[3]referred to as the "Gilmore-2009" model, hereafter
[4]referred to as the "Stecker-2006" model, hereafter

spectrum very well.
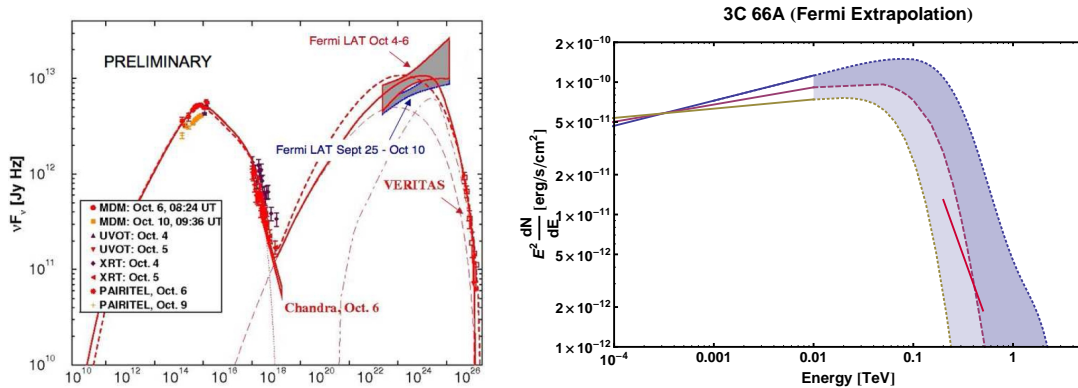
Figure 4.7: **left:** The measured spectra of 3C 66A from Reyes (2009). **right:** The extrapolations within the measurement errors on the GeV spectra and corrections to give the range of extinctions within the various EBL models (see text and figure 4.6).

From these comparison with non-simultaneous and simultaneous γ-ray measurements, it is concluded that a simple extrapolation from GeV to VHE energies, with appropriate EBL absorption take - gives in general a good match to the VHE data. In the case where there is a clear break, i.e. for the August 2008 observations of PKS 2155-304 the extrapolations are slightly off but still compatible within the statistical error in the VHE measurements and the uncertainty in the EBL attenuation.

A detail study of the GeV and VHE spectrum of the quasar PKS 1510-089 was done in the course of this thesis using LAT and HESS measurements respectively, and is reported in chapter 5.

4.3 Redshift upperlimits of γ-ray bright blazars from EBL extinction.

There are not many instances of VHE blazars that do not have a well measured redshift, since the selection process for observing blazars usually involves a limit on the redshift. However there are some blazars which were detected in the VHE regime, due to either a serendipitous mistaken redshift attributed to it, or because it happened to be an interesting enough source to risk the observing time. By using some assumptions on the intrinsic spectra the amount of EBL absorption could be estimated from the VHE flux measurements. Such assumptions on the intrinsic spectra can be either from theoretical emission models or as in the previous sections an extrapolation of the GeV measured spectra. Theoretical estimates usually assume the hardest possible spectra from the emission mechanism considered, and hence will give an upperlimit limit on the amount of EBL extinction suffered, correspondingly an upper limit on the redshift. The measured spectral

index in the GeV on the other hand can be much softer than the theoretical limits. Thus assuming that the VHE and the GeV part are from the same emission mechanism this method gives stronger constraints to the redshift. Table 4.3 gives such estimates based on GeV extrapolations and the Aharonian-2006 EBL model for 4 blazars.

Table 4.3: Redshift estimates from EBL extinction.

Name	FGST data			VHE data				z
	Epoch	F(> 100MeV) ($/$cm$^2/$s)	Γ_{GeV}	Instruments	Epoch	E_{thr} (GeV)	F($>E_{thr}$) ($/$cm$^2/$s)	
3C 66A	Sept/Oct '08	3.6×10^{-7}	1.87	VERITAS	Sept/Oct '08[5]	200	1.75×10^{-11}	0.48
PG 1553	LBAS	8.0×10^{-8}	1.7	HESS	May/August '05[6]	200	5.8×10^{-12}	0.55
				MAGIC	Mar-May '08[7]	200	1.76×10^{-11}	0.47
S5 0716+714	LBAS	1.64×10^{-7}	2.08	MAGIC	Nov '07/April '08[8]	400	8×10^{-13}	0.25
PKS 1424+240	LBAS	6.2×10^{-8}	1.80	VERITAS	Feb-June '09[9]	200	$\sim5\times10^{-12}$	0.47
				MAGIC	April-June '09[10]	100	1.1×10^{-10}	0.25

The GeV and VHE observations for the source 3C 66A are the only truly simultaneous measurements in this list, and gives the most accurate constraint on the redshift by this method.

For PG 1553, neither the MAGIC nor the HESS data are simultaneous with the FGST observations. The redshifts derived are thus not very constraining due to possible variability in the source. The FGST and MAGIC data on S5 0716+714 are again non-simultaneous and the previous caveat applies.

The VHE measurements of PKS 1424+240 are during flaring episodes. The true GeV spectra during these flares is likely to be different than the LBAS measurements, therefore these redshift estimates are uncertain.

---

[5] Reyes (2009)
[6] Aharonian *et al.* (2006a)
[7] Elisa Prandini *et al.* (2009), ICRC 2009
[8] Mazin *et al.* (2009), ICRC 2009
[9] ATEL 2084, Ong & the VERITAS Collaboration (2009b)
[10] ATEL 2098, Teshima (2009)

Part III

Observation of high-z blazars: *PKS 1510-089* and *3C 279*

High redshift blazars, suffer more EBL-extinction, hence are ideal for measuring the level of EBL in the intervening extragalactic space. Two schemes to trigger HESS observations of blazars, on flares in the optical and/or GeV wave bands, were laid out in chapters 3 and 4. As a result of these monitoring activities, there were three triggers on two blazars for which H.E.S.S. data was taken.

There were two GeV-triggered H.E.S.S. observations on *PKS 1510-089* in March and April 2009. *PKS 1510-089* is an extreme FSRQ, a γ-ray blazar detected previously with the EGRET instrument. This source showed a prominent GeV flare in March-2008, recorded with the AGILE satellite (D'Ammando *et al.* (2008), ATel on March 20), before the launch of FGST. The results of this observation are published in D'Ammando *et al.* (2009a). Subsequently several flaring episodes were reported both by AGILE (D'Ammando *et al.* 2009b; Pucella *et al.* 2009; Vercellone *et al.* 2009) and Fermi-LAT (Tramacere & the Fermi Large Area Telescope Collaboration (2008); Ciprini & the Fermi Large Area Telescope Collaboration (2009); Cutini *et al.* (2009)). A hard-X-ray burst was also reported by Swift/BAT, (Krimm *et al.* 2009). Optical bright states were reported by the GLAST-AGILE Support Program (GASP) of the Whole Earth Blazar Telescope (WEBT) via ATels Villata *et al.* (2009); Larionov *et al.* (2009).

The AGILE detected flare in March, 2008 was during the full-moon period when HESS doesn't observe. PKS 1510-089 was observable from the HESS site in 2009 from mid-February till mid-August. The first ATel in 2009 from AGILE was sent out on March 10th, a day before full moon, and in the subsequent days the moon was up during the good-zenith-angle range of this source, making observations with HESS, impossible. The first window of opportunity for HESS started from 20th of March, on which the first observations on this source with HESS was taken. This ToO observation campaign ended on April 2nd 2009, when FGST measurements showed the GeV flux to have gone below $F(> 100\,MeV) = 10^{-6}/cm^2/s$.

The FSRQ *3C 279* was observed following a bright phase (R magnitude brighter than 15.5) recorded with ATOM, in December, 2008 till January, 2009. During this optically bright phase, a GeV flare was also recorded by the Fermi LAT-team. Both these observations prompted a Trigger of Opportunity (ToO) request for observations

with HESS. This was one of the sources on the Fermi LAT-monitored-sources list, for which the LAT-team provided GeV fluxes since August 2008, binned over 1 day periods. Increased activity, with Flux(E > 100 MeV) in excess of 1.5×10^{-6} photons cm^{-2}s^{-1}. in this source was indicated by Fermi, ATel on 6 Dec 2008 Ciprini *et al.* (2009). However this source became visible from the H.E.S.S. site at reasonable zenith angles ($< 40°$), only from January 2009. HESS observations

In this chapter the analysis of the VHE data from H.E.S.S. observation on these two sources is presented. In addition the analysis results of the relevant Fermi data on PKS 1510-089 is also reported. The combined γ-ray data, are then used to discuss the implication on the EBL level.

5.1 HESS observations and VHE data analysis

HESS observations are taken during the night in moonless periods. Observations are taken only if there is no chance of precipitation, since the camera electronics is operated at high voltages. The telescopes record the Cherenkov lights (UV and blue) from air-showers in the atmosphere, (Aharonian *et al.* 2006c). VHE signals have low signal to background, hence observations on a target are taken in long exposures, called *runs*. A complete run is 28 minutes in duration. For VHE sources, typically $\sim 10s$ of hours of observations are required for a detection. Some runs might be shorter than 28 mins. to fit into the available dark time, or could have been cut short during run time due to technical faults or bad weather. The observations are taken in the *wobble mode*, in which, the source position is offset from the pointing direction of the telescopes by (usually) a fixed angular distance. For runs on the source presented here the angular offset was $\pm 0.5°$. The pointing direction was off-set around the source position in RA and dec by this fixed angular distance from run to run.

The standard approach to analyze VHE data, is to start out with an analysis of the entire exposure available on a source, to get maximum photon counts from it. In case of detections, a spectra and light-curves are generated, if possible. For non-detections, the usual procedure is to accumulate more observation-hours on the source, and reanalyze after sufficient data has been accumulated.

For the data set considered here, such a procedure is not possible since observations were based on flares in other-wavelengths. This implies a unique state in the source, and possible flares that could be observable in the future cannot be predicted. The triggers for VHE observations was explicitly done since it is expected - that the VHE brightness is correlated with the GeV brightness. In chapter 4, I have shown that this is indeed the case for most sources that are bright in both the GeV and VHE bands. Furthermore, since both the sources PKS 1510-089 and 3C 279 are not established VHE emitters, the number of analysis should be kept minimum to keep trial factors low. In principle each analysis

is considered as a separate measurement and adds to the trials. Also, breaking the data into sub parts counts as separate measurements for each sub part, and hence additional trials. The trial factors are used to penalize the maximum significance of a measurement, to account for the chance probability of getting a given significance when making multiple measurements (analysis).

Therefore the approach I use here is to define the analysis method prior to doing the analysis and also define a priori how the entire data set will be divided into sub parts. The analysis is defined by the *analysis method* and the selection-cuts used in the analysis. Analysis methods used could be - a Hillas style analysis Aharonian *et al.* (2006c), Toolkit for Multivariate Data Analysis (TMVA), Ohm *et al.* (2009), 3-D shower reconstruction analysis Lemoine-Goumard *et al.* (2006) or model analysis de Naurois & Rolland (2009). Selection-cuts are required to maximize the signal to noise ratio for a given source spectrum. After choosing an analysis method, at first the entire data set would be analyzed and a spectrum extracted, if possible. Irrespective of whether this first analysis yields a detection or not, the VHE data that is strictly simultaneous to the GeV/optical flare period (that triggered the VHE observations) is analyzed separately. This is done to check if there is a correlated increase in the VHE flux level compared to the low frequency band.

For the analysis done in this work, is the *wobble-chain* analysis, Aharonian *et al.* (2006c). The data recorded is first checked for quality. These quality cuts are used to reject those runs that were taken during less than optimal weather conditions to have low systematic errors. Clouds or haze in the atmosphere affect the cosmic-ray rate detected by the telescopes, which under perfect weather conditions is a function only of the zenith angle. Hence too low cosmic rate, or a large fluctuation in the rate is indicative of unstable atmospheric conditions, which would lead to a large error in the measurements. A cut on the overall zenith-angle-corrected cosmic-ray rate and its rms fluctuation is used for rejecting bad weather data. For the same reason individual telescopes that suffered from hard ware problems or had problems in triggering or recording the data during a run are excluded from the analysis. Any telescope with more than 5% of the pixels marked as broken pixels (i.e. turned off during all or part of the run) is excluded from the analysis. Runs with such hardware problems are still used for data analysis, but as 3-telescope or 2-telescope runs depending on how many telescopes had too many broken pixels during data taking (or any hardware problem for that matter). The quality-calibrated data used in this work, is made available by the HESS group at MPIK, Heidelberg - and is conventionally referred to as the *Heidelberg quality cuts* within the HESS collaboration. This terminology is used in this work as well, in order to differentiate with other HESS internal calibration tools.

The data-analysis for a point source can be summarized in the following steps:

1) Discriminating γ-ray photons from background hadrons,

2) Reconstructing the energy and source direction of the primary γ-ray photons,

3) Estimating the background rate of cosmic-ray events, and

4) Construct the source spectrum by binning the photons into energy bins (weighted by the relevant effective area).

This standard analysis tool was developed at the MPIK, Heidelberg, and has been used extensively within the HESS collaboration.

The image on the camera for an event triggering the telescopes, is parametrized according to it shape. The characteristic distribution of the shape parameters are used to discriminate γ initiated showers from cosmic-ray initiated shower. These shape parameters and the optimum selection cuts on these given in Appendix B. The intensity of the recorded event and the angular distance (from the source position) squared are also parameters that are used in the γ-hadron separation. HESS sensitivity is non-linearly dependent on the photon energy, and the VHE signal from sources is overwhelmed by the strong background of cosmic-rays. Furthermore, the minimum energy threshold strongly depends on the zenith-angle of observation. This is important as VHE sources invariably have a powerlaw spectrum with a negative slope. This implies that a lower energy threshold leads to more photons being detected from a source. Therefore the source spectral characteristics (i.e. the slope and normalization for a powerlaw approximation of the source) needs to be considered while optimizing the shape-cuts to maximize the detection significance. These optimum cuts on the image parameters for specific source spectra are called *shape-cuts*.

The background cosmic-ray rate, is obtained by the so called *reflected-region* background method, Berge *et al.* (2007), where a number of off-source regions are chosen around the center of the camera FOV. The off-source regions have same offset angle from the center of the camera, as the on-source region. The on-source region is defined by a fixed radius around the source position (source position is usually taken from the radio counterpart position). The stereoscopic view of shower images greatly improves direction reconstruction Hofmann *et al.* (1999). The ratio of the area of the on-source region to the summed area of all off-source regions is called the "α" parameter, and is used for normalizing the off-source counts. The excess events is calculated by $[excess = on - \alpha \times off]$. The significance of the source is calculated using equation (17) in Li & Ma (1983).Due to the high background rate in the VHE regime, it is conventional to require a minimum of $5\,\sigma$ to claim detection of a new source.

For distant sources like PKS 1510-089, at $z = 0.36$, and 3C 279, at $z = 0.546$, the VHE spectra is expected to be very soft ($\Gamma \approx 5$, from estimation of the extrapolation of EGRET spectra) as well as faint, due to EBL absorption. Therefore *soft-cuts* were chosen as the appropriate shape-cuts for the analysis of these sources. The *soft-cuts* (see Aharonian *et al.* (2006a) and Appendix B) are optimized for a source photon-index of 5, with a 1% crab flux ($> 100\,\mathrm{GeV}$).

5.2 PKS 1510-089

PKS 1510-089 is a radio-loud, highly polarized quasar (Stockman *et al.* 1984; Hewitt & Burbidge 1993) at a z of 0.36. It is a FSRQ with clear indication of the jet pointing at earth at very small orientation angle, due to apparent superluminal motion of $20c$, Homan *et al.* (2001). The radio VLBI observations of this source (Homan *et al.* 2002) show clear jet counterjet features and a high degree of polarization. This source has been extensively monitored in X-rays and broad band simultaneous spectrum has been published (see D'Ammando *et al.* (2009a) and the references therein). The broad band spectrum shown in D'Ammando *et al.* (2009a) shows a synchrotron component with peak in the IR. It also shows a probable thermal component as a UV bump, which could be from the accretion disk. It was detected in MeV-GeV γ-rays with the EGRET instrument on board the CGRO, Hartman *et al.* (1999). The EGRET integrated flux above 100 MeV was measured to be between (13 ± 5) and $(49 \pm 18) \times 10^{-8}$ photons cm^{-2} s^{-1} and the average over all EGRET data is described with a power law with photon index $\Gamma = 2.47 \pm 0.21$.

There were a series of GeV outburst observed from the quasar *PKS 1510-089*, in 2008 and 2009. The publicly available Fermi light curve is shown in figure 5.1 (upper panel), along with the optical light curve obtained with ATOM (lower panel). The two triggered HESS observations were from the two largest flares seen with Fermi, marked with the blue boxes. In the optical band, ATOM recorded flaring activity from January
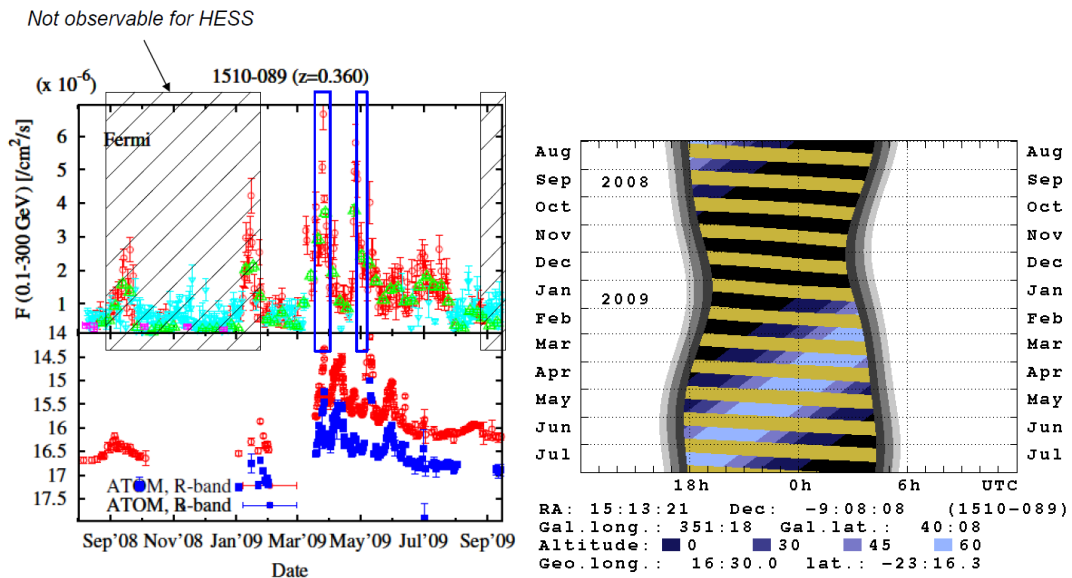
Figure 5.1: **Left:** GeV and optical light curve of the quasar PKS 1510-089. The periods of HESS observations are denoted by the blue boxes on the Fermi light curve. **Right:** The visibility of the source from the HESS site, using the tool by Konrad Bernlöhr (MPIK, HESS internal web pages). The colors show the altitude of the source, light blue for the best observing conditions and darker shades for lower altitudes. Light brown color denotes periods with the moon in the sky, when HESS does not observe.

2009, lasting till July 2009; considering an R-band magnitude of ~ 16.0 as the base flux for the period between August 2008 and Sept 2009.

5.2.1 H.E.S.S. observations of PKS 1510-089

The first HESS ToO-campaign was between the 20th of March and the 2nd of April, 2009 (called the "March-2009 flare", hereafter); and the second was between 27th of April and 29th of April, 2009 (referred to as the "April-2009 flare", hereafter) [1]. In all there were 48 runs taken on the source (see Appendix A, table A.1 for the complete observing log). However, 29 of these failed to pass the Heidelberg data quality cuts Aharonian *et al.* (2006c). The summary of the runs that pass quality cuts are given in table 5.1.

Table 5.1: Details of HESS observation on PKS 1510-089, triggered from GeV flare. Only those runs which passed Heidelberg quality cuts, and have at least 3 good telescopes taking part in the run are included in this table. Event selection requires an event to be recorded by at least 2 telescopes, however the soft-cuts configurations used for the analysis of this data is available for only the 4-telescope and 3-telescope runs.

Data set	N_{tel}	Date	Z range (°)	$<Z>$ (°)	N_{runs}	Live time (hours)
Ia	4	20 Mar - 2 Apr, 2009	14-44	26	9	3.9
Ib	3	20 Mar - 2 Apr, 2009	14-37	20	7	2.7
II	any	27 Apr - 29 Apr, 2009	...	...	0	0

The data sets after applying the Heidelberg data-quality cuts are presented here. The data set during the March 2009 flare was divided into two subsets depending on the number of telescopes participating in the run (N_{tel}). The range of zenith angles for the runs and the mean live-time weighted zenith angle is given in the table as "Z-range" and "$<Z>$". The live time in hours is obtained after correcting for dead time.

No HESS observations could be made of the GeV flare seen in February, since it was outside the visibility period for HESS. The March-2009 GeV flare was accompanied by an optical flare as well. Though during the April-2009 flare the optical flux was nominally high, there was no well defined peak contemporaneous with the GeV flare as in the previous one. The highest optical flare seen in May, 2009 could have been observed with HESS, but wasn't observed since it corresponded to a low state in GeV band.

5.2.2 Analysis I: Entire data-set

Initial analysis was done on all the 4-telescope and 3-telescope data that survived the Heidelberg data-quality-cuts. A total of 21 runs out of the 40 runs taken following the March-2009 flare had to be rejected due to bad weather and/or hardware problems, and

---

[1]Note that in the text references to flaring episodes in PKS 1510-089, refer to the MeV-GeV band (i.e. the HE band) unless specified otherwise

all runs from the April-2009 observations as well. There were 3 runs which had problems with 2 of the telescopes, and were discarded from the analysis. This is because, accounting for the systematics on the energy (and the reconstructed spectrum) gets more complicated when combining 2 telescope runs to 3 and 4 telescope runs. Thus resulting in a total of 16 runs surviving all the data selection criteria.
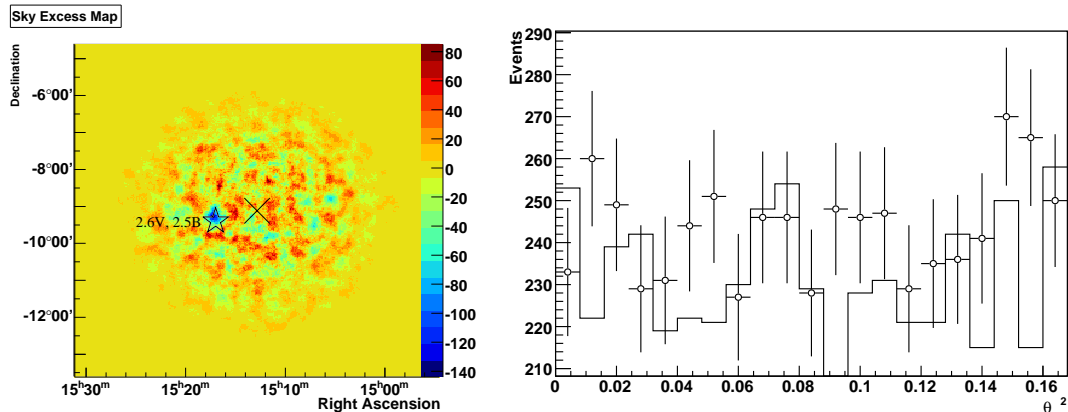
Figure 5.2: **Left:** The sky excess map from all good 4 Tel runs in the period March-April 2009, from *wobble-chain* analysis with *soft-cuts*. The vertical axis shows the declination angles. The position of PKS 1510-089 is marked with a '×'. The negative excess around the position marked with a 'star' symbol is due to PMTs being switched off around this position - since there is a bright star, HIP 74785 (2.6 V magnitude and 2.5 B magnitude) here. **Right:** The theta square distribution for the on-source events (points with error bars) and off-source events (solid histogram), of the same data set. The events with $\theta^2 \leqslant 0.02 \, \text{degree}^2$ are used to calculate the excess (on - off). There is no detection in this particular analysis.

Table 5.2: Results of VHE data analysis of PKS 1510-089. First 5 rows are data which pass the Heidelberg quality-cuts. The last row is on data, with relaxed limit on the broken pixels (see section 5.2.3)

Data Set	method	*on*	*off*	α	excess	rate (γ/minute)	significance (σ)
Ia	soft-cut/wobble-chain	609	4486	0.128	32.998	0.14	1.3
Ib	soft-cut/wobble-chain	341	2354	0.133	28.389	0.18	1.5
Ia+Ib	**soft-cut/wobble-chain**	**950**	**6840**	**0.13**	**62.168**	**0.16**	**1.9**
Ia	TMVA/Heidelberg-HAP	...	...	...	7.0	0.03	0.7
French DSTs	standard/French-HAP	34	237	0.09	12.778	0.04	2.4
(Ia+Ib)*RBPL*	soft-cut/wobble-chain	1121	7778	0.13	123.223	0.31	3.6

The results of my analysis is summarized in the first three rows of table 5.2. The data set Ia and Ib correspond to the previously defined observations (runs) passing the Heidelberg data quality cuts (see table 5.1). The analysis on this data did not yield a detection, since the significance of excluding a null hypothesis is only $\approx 1.9\,\sigma$.

The excess events sky-map, and the (angular-distance)^2 distribution of events around the source position, for data set Ia, is shown in figure 5.2. The angular-distance, θ for a γ-ray event is the angular separation between the reconstructed source position and the

actual source position.

It is customary in the HESS collaboration to cross-check results with multiple analysis chains. In the 4th and 5th rows of table 5.2, the results of the cross-check analysis of alternative analysis chain is shown. The TMVA analysis, Ohm *et al.* (2009), was performed by Stefan Ohm of MPIK, using an equivalent set of *soft-cuts* appropriate for this analysis - called the *weak-ζ-cuts*. The cross-check was done on data set Ia. Due to the lower excess events got with this analysis, it is not expected to perform better on the data set Ib, which has only 3-telescope data. The French DSTs are obtained after a slightly different set of data-quality cuts as the data set in my analysis. This analysis was done by Francesca Volpe of MPIK. The *standard* shape-cuts (table B.1) to discriminate photon and hadrons are also different. The standard-cuts used for this cross-check have a higher threshold energy due to a higher *Size-cut* (i.e. a higher image intensity), and thus it would detect significantly less events for a source with a soft spectra. For such low significance, the excess events and significances from separate analysis are expected to differ. The cross-checks confirms the results of the analysis done here.

5.2.3 Recovering problematic data

The data set obtained during this campaign was triggered during two historically high GeV-flares in this source, and hence are unique. However, the total usable data was a fraction of the total observation. I investigated the possibility of recovering the rejected data. The data set suffered from a combination of bad-weather and hard ware problems. Figure 5.3 gives a summary of the problems in the entire data set (data sets Ia and Ib). The problems fall into three categories - viz. hardware problem, bad-weather, and other problems. The first category includes those runs that had either one or more telescopes excluded due to more than 5% of the pixels broken during the run, or due to error in tracking information in one or more telescopes. Such a run is still considered as good run, as long there was just a single telescope which had the problem and can be excluded from the analysis. For weather affected data the runs are summarily rejected, since these have large systematic errors due to fluctuations in the system rate. The runs in the third category have no useful data that can be analyzed, 5 runs being too short in duration (less than 10 mins) of the runs and the other 2 runs had hardware related problems. Of the later, one run had information missing for which the data could not be calibrated, whereas the second run had problems with data acquisition.

In the weather affected runs I checked the rms deviation in the cosmic-ray rates recorded during the runs. Some runs showed large dips in the rate during the run with high rms fluctuations; where as some seem to have a stable rate, even though the absolute rate was lower than the acceptable threshold. However, all of these runs also had hardware problems. The combined systematic errors would be too too high. Hence these runs could

29 runs were rejected out of a total of 48

hard ware problems (33 runs)	**Weather problems** (23 runs)	**other problems** (7 runs)

all had some hard-
ware problems too

Tracking / no HW info 9(ct1) + 17(ct4)	Broken Pixel 17 runs	Truncated runs 5 runs	1 run: all 4 tels 1run: no DST

10 still accepted as good runs:
7 (3-Tel) runs + 3 (2-tel) runs

Multiple problems in some runs
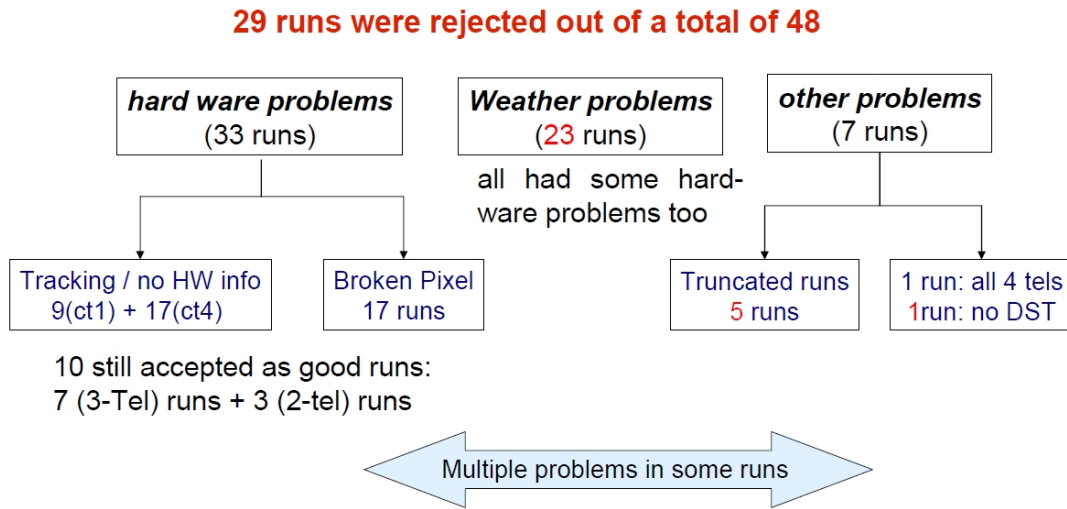
Figure 5.3: The breakup of the runs as per the type of problems in the data set. Note that there is an overlap in all categories, i.e. there are runs that had multiple problems, and hence get counted separately under the various categories. For example, all bad weather data also had some hardware problems, thus the out of the 33 runs listed under *hardware*, 23 are also included in the *weather problem* category.

not be used.

The runs affected by hardware problems involving broken pixels can however be reconsidered by relaxing the limit on the number of broken pixels. For such cases, except for the broken pixels, the data from the entire camera is recorded as usual for the entire run duration, and can be analyzed in the usual scheme by changing the value of a configuration-flag. Each of the HESS cameras consist of 960 pixels and the nominal broken pixel limit is 50 ($\approx 5\%$ of the pixels). During a run pixels get turned off, if there happens to be a bright star at that position or due to meteor transits. There could also be hardware or software problems in a set of pixels grouped together (a drawer consist of 16 adjacent pixels, having their trigger and read out systems, as well as the high voltage power supply together). I found that most of the telescopes that were rejected due to broken pixels had a few drawers missing from data-taking during the run. An example is show in figure 5.4, where the camera of CT4 for the run with id 50482 is shown. There are three cluster of broken pixels marked in red, one drawer each in the top right and bottom left; and two adjacent drawers nearer to the center of the camera. A systematic error of 5% is assigned on an average, due to broken pixels in the telescopes, as long as the number of such pixels is less than 50. Internal studies in the HESS collaboration have estimated an increase in the systematic errors by less than 2% if the limit is relaxed to 100 pixels, even with the broken pixels near the center of the camera. However to be conservative I relaxed the broken pixel limit to a the minimum number that effectively recovered as many of the affected runs, that had less than 100 broken pixels. This limit was found to be 75 pixels, and is used in my subsequent analysis on this source. The systematic errors will not be more than a 2% percent by doing this.
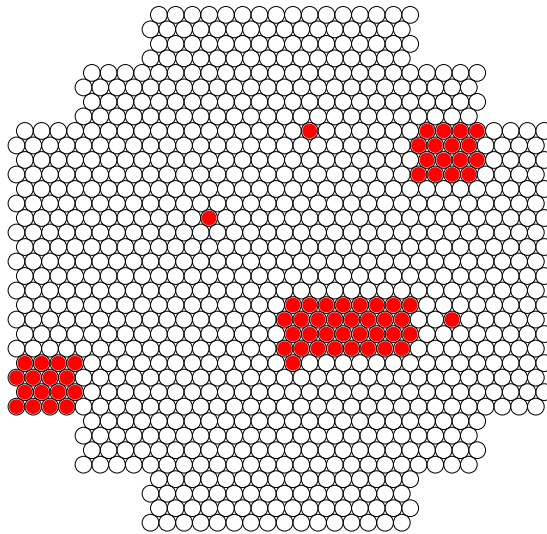
Figure 5.4: The schematic picture of the telescope-camera that was kicked out in a particular run (run number 50482) due to broken pixels in the camera exceeding the Heidelberg data-quality cuts.

In the entire data set there were 5 runs in which one of the telescopes could be recovered in this way, and the runs analyzed as complete 4-telescope runs. The run numbers of these recovered runs are - 50403, 50404, 50482, 50483, and 50484. However, the resulting analysis gives us a significance of only 3.6σ (c.f. 1.9σ otherwise, see last row of table 5.2); which cannot be considered as a detection.

5.2.4 Analysis II: Sub-set of data, based on Fermi flare

It is shown in the chapter 4, that the GeV brightness, can be in general a good proxy for the VHE brightness. It is therefore likely that VHE flux in PKS 1510-089 might have also undergone a flare, contemporaneous with the GeV flare. It is therefore justified to break the HESS data into a smaller subset, isolating the period covering the Fermi flare and analyze it separately. The data that could be recovered by relaxing the limit on broken-pixels, as described in the previous section, is used in this analysis.

Selecting runs contemporaneous to the March'09 GeV flare

The FGST data is publicly available, at - `http://fermi.gsfc.nasa.gov/ssc/data/` `analysis/`.The analysis software developed by the Fermi team and the user documentation is available for public use from this webpage as well. The LAT instrument records data is more sensitive and hence useful for non-GRB sources. FGST operates in a sky-scanning mode (except for specific pointed observations). It takes 90 mins for a single orbit around earth and can scan the entire sky in 3 hours. The LAT data can thus be analyzed to obtain light curves. A a 24-hour time bin was found adequate for the relatively bright states of this source in March-April 2009. The FGST data analysis of this period resulted in significant detections on a daily basis (except between 12th to 15th of March'09) in the

LAT data.

The resulting light curve from my analysis on the LAT data for the month of March and April, 2009 is shown in figure 5.5. The time axis counts days from 1st of March, 2009; and the integral flux calculated between $100\,\mathrm{MeV}$ and $300\,\mathrm{GeV}$ is shown on the vertical axis. Except for the days from the 12th to the 15th of March, daily fluxes could be obtained for the two month period. Note that FGST documentation recommends an unbinned likelihood analysis on each single temporal bin (1-day bins in this case) to get the correct normalization for the integral fluxes. This light curve is not generated from such a likelihood analysis, but from from a temporal binning of all photon events, weighted with the exposure. In such a analysis the normalization of the integral flux will be biased, though the relative variation in the integral fluxes is expected to be accurate within the error bars. For the purpose of identifying the duration of the flare this light curve is precise enough and will suffice.
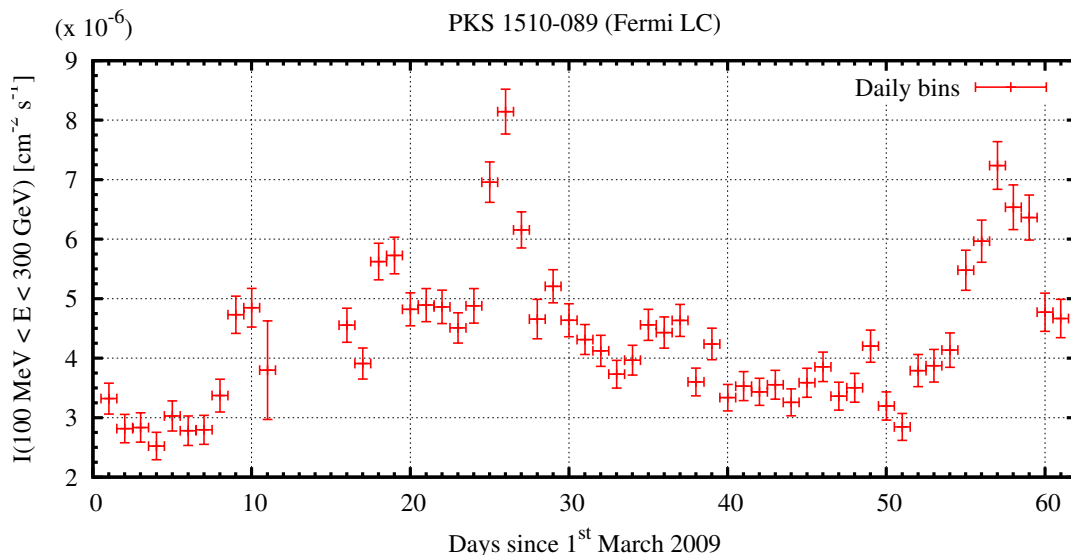
Figure 5.5: FGST light curve starting from the 1st of March 2009, clearly showing the two flares in March and April.

The two flares can be clearly identified; the first one peaks on the 26th of March, and the second one peaks on the 26th of April. I arbitrarily set a threshold flux of $6 \times 10^{-6}/cm^2/s$ to define the a flare in this data set. Thus the March-2009 FGST-flare lasted for three days from 25-03-2009 (UTC 00:00:00) till 27-03-2009 (i.e. 28-03-2009 UTC 00:00:00). In the following I will restrict the VHE data analysis to the data obtained during these three days. Since HESS observes during night time only (centered roughly around midnight UTC), binning for the LAT lightcurve could have been done centered on midnight UTC. However, note that after the night of $22^{nd}/23^{rd}$ March till the end of March, all HESS observations on a particular night were after midnight UTC. Hence the binning of LAT data from midnight to midnight is still appropriate as the HESS runs on

a given night do not get split by the LAT lightcurve bins. The runs taken during these three nights is summarized in table 5.3. Shown are the run number, the date, the zenith angle, the relevant threshold energy after correcting for reduced optical efficiencies and other relevant information. Recall that all the data taken during the April flare suffered from bad-weather and hardware problems, and is therefore not usable.

Table 5.3: The details of the runs taken during the March-2009 flare nights (see text).

Run#	Date (UTC)	<Z> (°)	t_{live} (hours)	E_{thr} (GeV)	eff	$E_{thr}^{\mu corr}$ (GeV)	N_{tels}	*Notes*
50421	25-03-2009	-	-	-	-	-	-	rejected/bad weather
50422	25-03-2009	-	-	-	-	-	-	rejected/bad weather
50424	25-03-2009	-	-	-	-	-	-	rejected/bad weather
50459	26-03-2009	18	0.43	195	1.1098	216	4	good run
50460	26-03-2009	14	0.43	191	1.1036	210	4	good run
50461	26-03-2009	15	0.43	191	1.0881	208	4	good run
50482	27-03-2009	16	0.44	192	1.1014	212	3	CT4: 73 broken pix
50483	27-03-2009	14	0.44	190	1.1322	216	3	CT4: 70 broken pix
50484	27-03-2009	17	0.44	193	1.1062	214	3	CT4: 54 broken pix
50485	27-03-2009	22	0.43	207	1.1185	231	4	good run
50486	27-03-2009	28	0.43	234	1.1322	264	4	good run

Data Analysis

In the VHE-data of the three March-2009 GeV-flare nights, there were three runs (run numbers 50421, 50422, and 50424) which were taken during bad-weather conditions and also had multiple hard ware problems in two or more telescopes - thus had to be rejected. There were 5 runs with all 4-telescopes passing the data quality cuts. There were three other runs for which three of the telescopes passed the data quality cuts, but the telescope, CT4 failed the nominal cuts, as it had > 50 broken pixels. The number of broken pixels were - 73 (run 50482), 70 (run 50483), and 54 (run 50484). According to the relaxed broken pixel limit of 75 pixels, these 8 runs are considered as 4-telescope runs in this analysis. This data-set gave, a significance of 4.8σ (see first row of table 5.4), very close to what is considered a conventional detection in VHE (i.e. a 5σ level). Accordding to the usual procedure, a cross-check analysis was requested with a separate pipeline called the *model++* analysis de Naurois & Rolland (2009), which is known to give good background rejection compared to the *wobble* analysis used in this work. The *model++* analysis does not perform an image cleaning, but models the noise distribution in the pixels as well as the signal. This results in more precise reconstruction of shower parameters and better background suppression (Acero *et al.* 2009). The results of the *model++* analysis confirm the detection of a VHE source at a 8.5σ level, at the position of PKS 1510-089, results are in the second row of table 5.4.

The sky-map from the analysis done in this work (*wobble* chain) showing the excess event distribution the March'09-flare dataset is shown in figure 5.6, left panel. The θ^2 distribution is shown in the right panel of figure 5.6. The exposure weighted average zenith

Table 5.4: Results of VHE data analysis of the March-2009 flare nights.

Data Set	method	on	off	α	excess	rate (γ/minute)	significance (σ)
Mar'09 flare	soft-cut/wobble-chain	666	4330	0.1252	124.	0.6±0.12	4.8
Mar'09 flare	loose-cuts/model++	309	1945	0.0909	132.2	0.63±0.09	8.5

angle for this entire data set was $\approx 19°$ and the optical-efficiency corrected threshold energy is $\approx 220\,\mathrm{GeV}$. A spectra is extracted between $220\,\mathrm{GeV}$ and $320\,\mathrm{GeV}$, shown in figure 5.7.
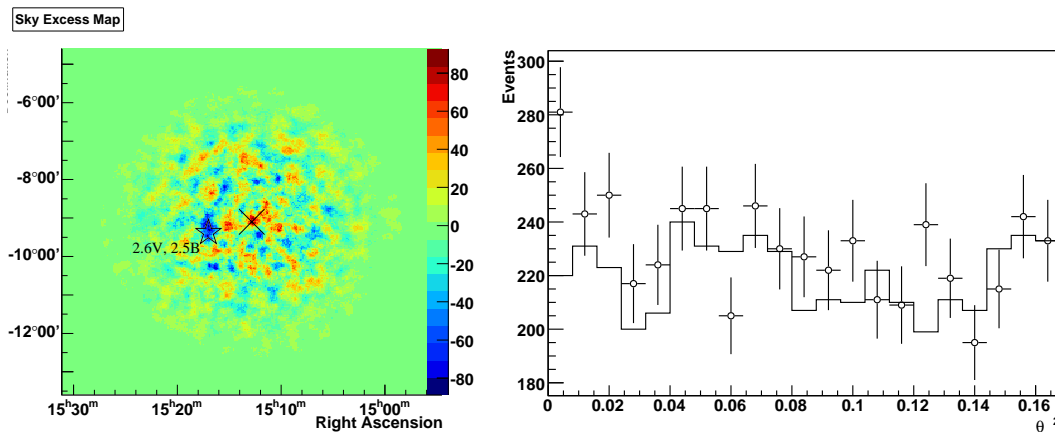
Figure 5.6: **Left:** The sky excess map from the runs on the March-2009-flare nights, analyzed as 4-telescope runs using the *wobble-chain* analysis with *soft-cuts*. The vertical axis shows the declination angles. The position of PKS 1510-089 is marked with a '×'. An excess is seen at this position. The negative excess around the position marked with a 'star' symbol is due to PMTs being switched off around this position - since there is a bright star, HIP 74785 (2.6 V magnitude and 2.5 B magnitude) here. **Right:** The theta square distribution for the on-source events (points with error bars) and off-source events (solid histogram), of the same data set. The events with $\theta^2 \leqslant 0.02\,\mathrm{degree}^2$ are used to calculate the excess (on - off).

The binning in the spectrum is chosen such that there is at least 1.5σ per bin, as well as > 10 events per bin (the three lowest energy points in figure 5.7). The spectrum can be fit with a power law:

$$(5.1) \qquad \frac{dN}{dE} = N_o \left(\frac{E}{0.25\,TeV} \right)^{-\Gamma}$$

with parameters $N_o = (9.73 \pm 3.28) \times 10^{-11}/\mathrm{cm}^2/\mathrm{s}/\mathrm{TeV}$, and $\Gamma = 5.13 \pm 3.74$. The integral flux in the energy range $220\,\mathrm{GeV}$-$320\,\mathrm{GeV}$ is $\approx 9\%$ of the crab flux, within the same energy band.

5.2.5 Accounting for trials

The resulting maximum significance for the VHE data-analysis on the March'09 flare, needs to be penalized for the various trials on the data. As explained before each separate
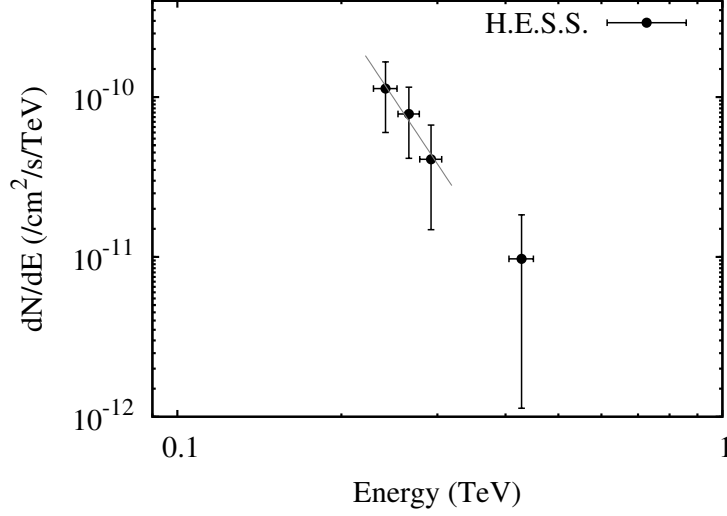
Figure 5.7: The spectrum obtained using soft-cuts, re-binning all events between 220 GeV and 320 GeV. Points that are consistent with zero are not shown. the power-law fit was restricted to the three bins between 220 GeV and 320 GeV. The last point (highest-energy) was not used in the fit as it has less than 10 events in the bin.

analysis is an independent measurement for the VHE flux of the source. Even though the source is variable and we specifically observed based on a GeV-flare the multiple cross-checks would also count as trials. To be conservative all the different analysis done all the entire data-set as well as the March'09 are counted in the trials. Thus we have 4 trials for the entire data set (last 4 columns of table 5.2) + 2 trial for the March'09 flare data (table 5.4), giving a total of 6 trials, to get the *model++* detection of 8.5σ. The trial factor are calculated as follows:

➤ If p_x is the probability of getting a positive 'x'σ level detection in a single measurement by chance (i.e. due to random fluctuations)

➤ Then getting at least a single 'x'σ level detection in n number of trials is

$$(5.2) \qquad = \sum_{i=1}^{n} C_i^n (p_x)^i (1 - p_x)^{(n-i)} \approx n p_x (1 - p_x)^{(n-1)} \approx n p_x \, ;$$

where $C_i^n = n!/(i!(n-i)!)$.

(The approximation is true if 'x' is highly significant, in which case p_x is very small and all higher orders, $p_x^{(i>1)} \to 0$. Holds very well for $x > 5\sigma$)

➤ This is also the readjusted probability of rejecting the null hypothesis.

➤ Therefore the new sigma level, 'y' is the significance level such that -

$$(5.3) \qquad p_y = n p_x$$

For the PKS 1510-089 detection, we have a 8.5σ detection and 6 trials, i.e. $x = 8.5$, therefore $p_x = 4.44 \times 10^{-16}$, and $n = 6$. Thus $p_y = 2.664 \times 10^{-15}$. This corresponds

to a post-trial significance $y = 7.8\sigma$. Thus this detection is at a 7.8σ level, taking trial factors into account. A further penalty could be added to the trials since we know that *model++* analysis shows systematically higher significances compared to *wobble* analysis, and the quantitative relation between the significances is not well defined for a given source. However such a penalty is unlikely to reduce the significance to below detection levels, since the amount of trial factors needed to bring a 8.5σ detection to below 5σ level is ≈ 650 million trials.

Post-trial significance

The detection of PKS 1510-089 is the detection of the furthest VHE blazar (at $z = 0.36$) with a secure redshift and high significance (7.8σ), till date.

It should be noted that for the VHE blazar 3C 66A (Reyes 2009), the redshift is not known. The value of $z = 0.44$ is the *commonly adopted* one. The detection of 3C 279 by MAGIC, Albert *et al.* (2008), was on a single night on February 23, 2006, at a pre-trial significance of 6.15σ. This detection is contentious due to the following region. The number of trial factors used to report the post-trial significance of 5.77σ, was only 10, the number of days in the 2006 observation campaign. The results were however reported two years later in 2008. The number of trials should count all single night observations of the source until the results were reported, in addition to counting the separate analysis done on all the data as well, which was not accounted for. The number of trials on the reported 3C 279 detection, that can result in a post trial significance of $< 5\sigma$ is ≈ 750. Such a number of trials could be easily added up by counting all days of observations prior to the publication of this result, and including all the different analysis on this source. This was an unfortunate result of delaying the analysis/reporting of an otherwise important result.

5.3 Constraints on EBL from observations of PKS 1510-089

For PKS 1510-089, a source at a redshift of 0.36, the measured VHE spectrum should be considerably attenuated due to EBL absorption. To constrain the EBL by the extinction the flux suffers, we need a good estimate of the intrinsic spectrum. This is possible since this source is bright in GeV energies, and as shown in chapter 4 the GeV spectum in general can be simply extrapolated to the VHE regime, and is consistent with measurements, corrected for EBL. In the following I analyze the publicly available FGST data on the source to extract an average (on the data from August 2008 till end of Sept 2009) as well as flare-period (March-2009 flare) spectra for the source in the MeV-GeV range.

5.3.1 Extracting *FGST* Spectrum

The differential spectra from FGST data is calculated by doing a likelihood analysis (individually on each energy bin) on the events within a time period, binned in energy. I choose

a suitable (approximately logarithm) binning to get a precise measurement for as wide a energy range as possible. The lower limit for the first energy bin is fixed at 200 MeV to keep systematic effects low, as advised by the Fermi LAT documentation. All bins that give a test statistics (TS) greater than 36 ($\approx$ equivalent to 6σ) and consistent with a positive-flux within the statistical-errors of the likelihood analysis are accepted.
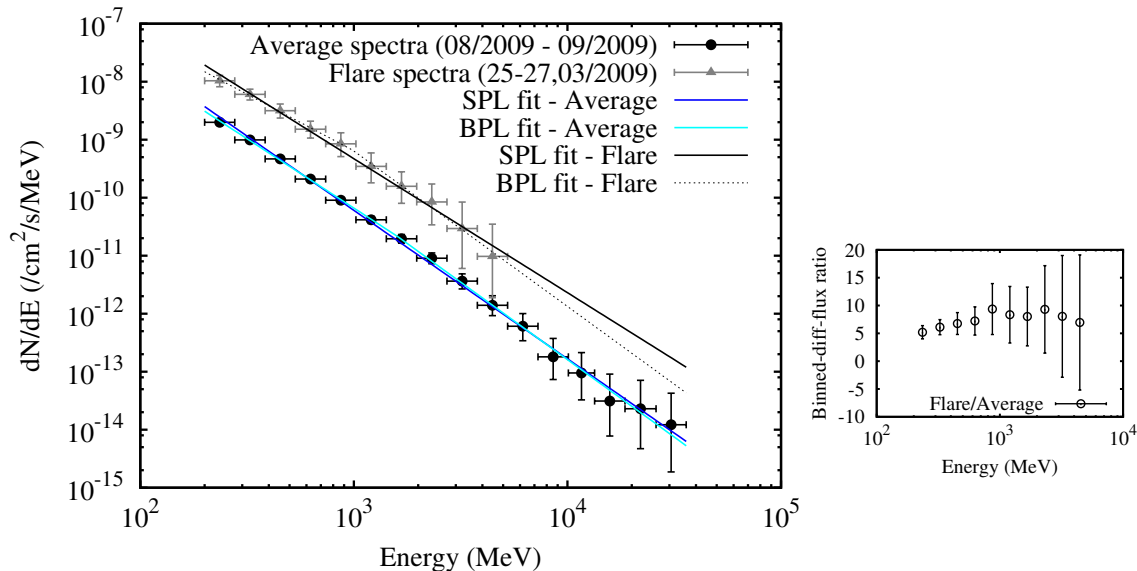
Figure 5.8:   **Left:**   Fermi spectral fits got by unbinned likelihood analysis of the March-2009-flare nights, and the average spectra obtained of the 14 month period between August 2008, and September 2009. **Right:** The ratio of the fluxes in the 10 bins over which the differential flux on the flare could be calculated with TS greater than 36.

The results of the analysis are shown in figure 5.8, left panel. The lower spectrum corresponds to the 14 month average, and the higher one is the spectrum for the three nights corresponding to the March-2009 flare (as identified in section 5.2.4). The 14-month average extends up to ≈ 36 GeV where as the flare spectra could be constructed up to ≈ 5.3 GeV. The ratio of the binned differential flux of the flare spectra over the 14-month-average, shows that within the statistical errors there is no evidence of a spectral change (see figure 5.8, right panel). The average (weighted by the square of the errors) of the binned-flux-ratio is $\approx 6.16 \pm 0.42$. Both the spectra are well fit with a simple power law (form of eq. 5.1, with the scale as 300 MeV), while a broken power law:

$$(5.4) \qquad \frac{dN}{dE} = \begin{cases} N_o \left(\frac{E}{E_{break} \, MeV} \right)^{-\Gamma_1} & ; \text{if } E < E_{break} \\ N_o \left(\frac{E}{E_{break} \, MeV} \right)^{-\Gamma_2} & ; \text{otherwise} \end{cases}$$

gives only a marginally better fit (see table 5.5). This further demonstrates that there is no curvature seen in the measured spectra for this source. Thus the flare spectrum is consistent with the 14-month average spectra rescaled by the average binned-flux-ratio, as can seen in figure 5.9.

70

Table 5.5: Results of spectral fits to Fermi data analysis on PKS 1510-089.

Data Set	function	Γ_1	N_0 or N_{break} $(/cm^2/s/MeV)$	Γ_2	E_{break} or E_{scale} (MeV)	χ^2/ndf
14-Month	SPL	2.56	1.32×10^{-9}	-	300	5.58×10^{-5}
14-Month	BPL	2.39	2.14×10^{-11}	2.67	1604	4.54×10^{-5}
March'09 flare	SPL	2.31	7.59×10^{-9}	-	300	9.74×10^{-5}
March'09 flare	BPL	1.95	6.61×10^{-10}	2.68	987	3.33×10^{-5}
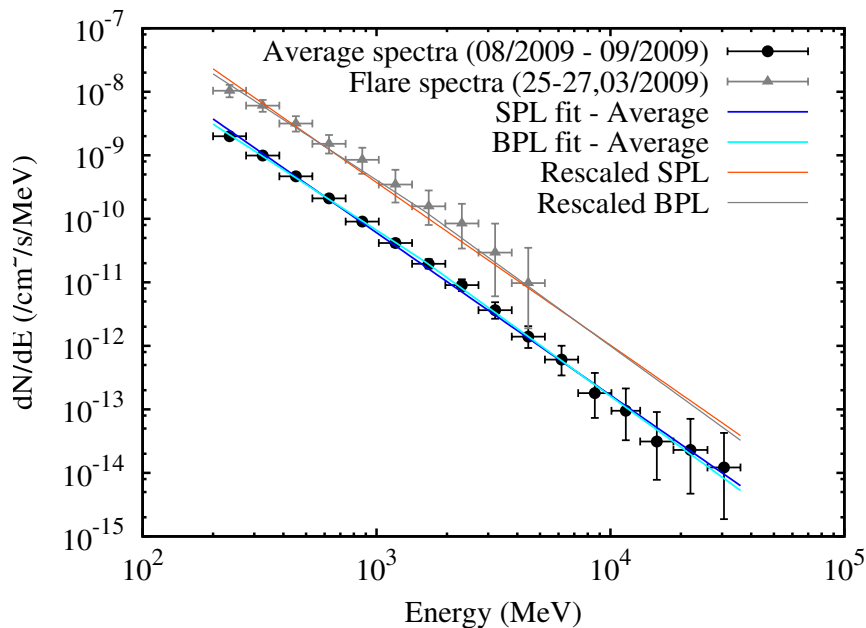
Figure 5.9: The Fermi LAT spectra for the March 2009 flare, and for the 14-month period between August 2008 till Sept 2009. The respective powerlaw (SPL) and broken-powerlaw (BPL) fits to the spectra are also shown.

Note that this energy regime (i.e. below $100\,\mathrm{GeV}$) is essentially unaffected by the EBL. Hence it is the spectrum at the source,i.e. the intrinsic spectra. Post analysis of the Fermi data, shows me that the spectrum of this source does not show any indication of a break or cut-off. Thus it is possible that the spectrum extends further with the same spectral shape, into the the VHE regime. In the following section I replace the flare spectra spectrum with the 14-month average spectrum rescaled by a factor 6.16 and use this as the de facto intrinsic spectra from 200 MeV to the regime of the VHE measurements, i.e. up to $\approx 320\mathrm{GeV}$.

5.3.2 EBL limits within spectral measurement errors

With the estimate of the intrinsic spectra and the HESS measurements in the previous sections I can check the amount of EBL absorption. A number of models for the EBL SED and its evolution with z are available in literature. The extinction as a function of energy for PKS 1510-089's redshift of 0.36 is shown in figure 5.10. The Gilmore-2009 model, and

the Franceschini-2008 models result in the least amount of absorption, while the Stecker fast-evolution model gives ≈ 50 times more extinction, at $300\,\mathrm{GeV}$. The vertical line in the figure, marks the energy of $300\,\mathrm{GeV}$, approximately the position of the last significant flux bin in the HESS spectrum. At first I ignore the systematic errors in the spectra measured in the Fermi and HESS regime, and test which model is best able to describe the combined data set, within the statistical errors. Then I consider the effect of systematic errors, and state what conclusions can be drawn on the EBL models and the EBL intensity.
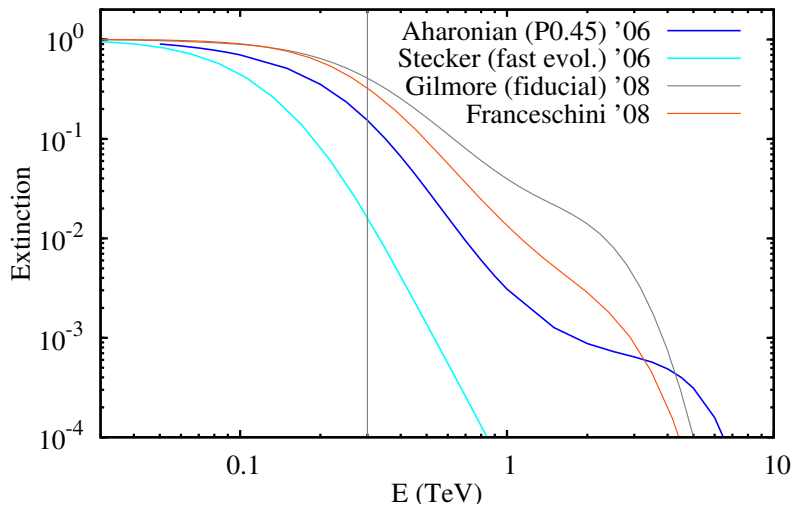
Figure 5.10: The extinction as a function of γ-ray energy, calculated taking the various EBL models in figure 2.8, for a source at $z = 0.36$. The vertical line is at $300\,\mathrm{GeV}$, and shows that the extinction can differ more than a factor of 10 at this energy within the different models.

The intention here is to fit the simplest functional form that can best describe the entire dataset from $200\,\mathrm{MeV}$ to $320\,\mathrm{GeV}$. The data set consist of the spectrum from the 14-month observations with Fermi - rescaled to the level of the March-2009 flare, and the HESS measured VHE spectrum during the same Fermi-flare. The simplest model that I can use is a power-law intrinsic spectra, corrected for EBL extinction (I call this model as the "γ-ray spectrum-fit', henceforth'). Thus the free-parameters that I need to fit are the normalization, and photon-index of the powerlaw component; in addition to the EBL model for the extinction correction. The EBL model can be any of the ones discussed in chapter 2.1 (see figure 2.8). I choose to try out the EBL-models which give the least (Gilmore-2009 and Franceschini-2008) amount of extinction, the most (Stecker-fast-evolution-2006) extinction and one which lies somewhere in between. For the last case, I can conveniently choose the Aharonian-2006 model which has been my working model in all the other chapters. The two lowest-extinction models are based on theoretical estimates from source populations responsible for contributing directly and indirectly to the EBL photons. The Aharonian-2006 model is a lower limit, derived assuming the VHE emission mechanism in blazars is dominated by inverse-Compton scattering electron. While the Stecker model can explain recent VHE measurements by invoking hadronic scenarios for

the VHE emission processes. Since I base my modelling of the VHE spectra solely on observations (from MeV to VHE range), and attempt to fit the simplest fitting model without special assumptions on the VHE emission mechanism of a particular source, this method can directly pick out the best EBL shape. The assumptions on the intrinsic spectra of the source is minimal since I directly measure it in a regime free from EBL absorption but still close enough to the VHE regime, to be fairly accurate. Thus the power of this technique is dependent only in the total error in the measurements of the blazar spectra.

To fit the powerlaw-EBL corrected models I developed a Markov Chain Monte Carlo (MCMC) code, using the Metropolis-Hastings algorithm, to find the parameters that maximize the likelihood of the model fit. Since the redshift of the source is known, the EBL extinction is applied as a precomputed extinction-curve (extinction verses energy of the photon) which was used to scale the intrinsic power law model. These extinction-curves are shown in figure 5.10. Thus the remaining free parameters were the normalization and the photon-index of the powerlaw. I assumed the errors follow a Gaussian distribution, and set up 10,000 iteration in the MCMC code, after ensuring that the acceptance-ratio was around 50%. I tried out a range of initial-guess values for the free-parameters, to converge on the best set of values yielding the maximum likelihood for each EBL model. The results are given in table 5.6 and the model curves are shown graphically in figure 5.11.

Table 5.6: Results of the MCMC modelling to the γ-ray data on PKS 1510-089.

EBL model	N_o $(10^{-9}/cm^2/s/MeV)$	E_{scale} (GeV)	Γ	$-Log\left[\frac{l_{G'08}}{l}\right]$
Gilmore-2009	7.4	300	2.55	0
Franceschini-2008	7.38	300	2.53	0.69
Aharonian-2006	7.29	300	2.36	2.30
Stecker-2006	7.23	300	2.42	0.91

5.3.3 Discussion

The Fermi spectrum covers more than two decades in energy compared to less than half a decade spread of the VHE spectrum. Moreover the fractional error on most of the Fermi flux points are much better than the HESS points. Therefore the normalization and photon-index of the powerlaw model fit is likely to follow the Fermi spectrum which is well described by a power-law. Hence it is no surprise that the fit parameters in table 5.6 are very similar. The extinction-curve would steepen the powerlaw-fit model above $\approx 100\,\mathrm{GeV}$, and the compatibility of the fit with the VHE data points will be dictated by the accuracy of the EBL-model. It is clear from the log of the likelihood-ratios (with respect to the Gilmore-2009 model) given in the table 5.6 that this quantity is dominated by the 16 data
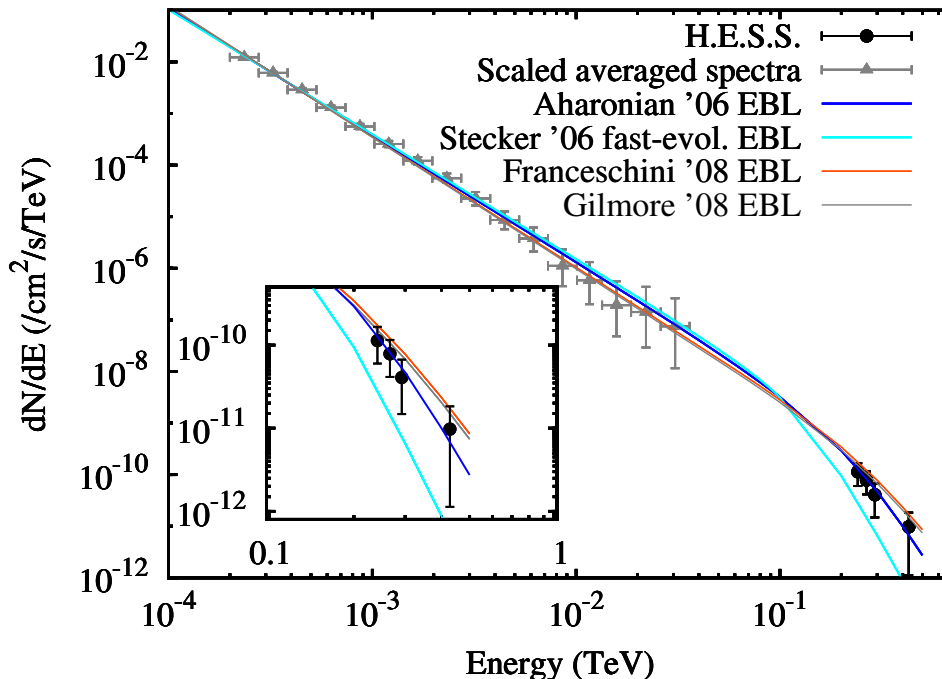
Figure 5.11: The various γ-ray spectrum-fit models are plotted, on top of the estimated Fermi flare spectra (rescaled 14-month Fermi spectra), and the HESS spectra. The inset is a blow up of the HESS measurements, showing clearly the compatibility of the EBL-models within the statistical error of the measurements. Note that only 1σ statistical errors are shown on the fluxes. An additional 20% systematic error on the HESS measured fluxes coupled to a 10% systematic error on energy would mean that all the models are compatible with the data.

points of the Fermi spectrum, yielding roughly the same goodness-of-fit for all the models. However from figure 5.11, it is clear that - the γ-ray spectrum-fit for the Aharonian-2006 model best matches the HESS data within the statistical errors. The Franceschini-2008 and Gilmore-2009 models are also compatible within the 1σ errorbars, where as the Stecker-2006 fast-evolution model implies much too high EBL extinction for the source, and is incompatible.

The systematic errors on the flux measurements ($\approx 20\%$) as well as the energy uncertainty, in effect allow a shift in the measured powerlaw spectrum by a scale factor in brightness and thus need to be taken into account to make conclusive statements on the EBL model. The Fermi systematic error on the flux measurements is dominated by the error on the effective area and is energy dependent. It ranges from 10% at 100 MeV to 5% at 560 MeV, and increases to 20% at 10 GeV. The systematic error on the energy is denoted by $\frac{\Delta E}{E} = ^{+5\%}_{-10\%}$, Abdo *et al.* (2009b).

The systematic error on the HESS flux is $\approx 20\%$, Aharonian *et al.* (2006c). Here I ignore any additional effect due to the relaxation of broken pixel limit, which is justified, from studies within the HESS collaboration that indicate less than 2% overall effect, for the broken pixel limit relaxed to more than 100 pixels. The uncertainty in energy calibration is

also energy dependent in the case of HESS. It depends on the spread of the reconstructed energy in the MonteCarlo simulations of air-showers. The energy resolution for HESS above the energy threshold is $\frac{\Delta E}{E} = \pm 10\%$ (see figure B.2 in Appendix B). Here ΔE is the difference between the reconstructed and true energy of a shower.

With the additional systematic errors on the flux and energy, it is clear that all the 4 EBL-models are compatible with the data. Therefore attempting to obtain the best normalization of a particular EBL-model (hence obtaining a constraint on the EBL level) with this data-set will give weak constraints. Such a normalization with its large errors, will be compatible with all the EBL-models considered here. No further statement on the EBL can be made from this data set.

5.4 3C 279

3C 279 is a well known quasar. It was the brightest γ-ray blazar during the EGRET era, and was always detected with EGRET when ever observed Hartman *et al.* (1999).

5.4.1 H.E.S.S. observations

The FSRQ 3C 279 was observed in January, 2009 following a flare in GeV detected with Fermi. The source was active in the optical bands during this period as well. The GeV and optical light curves are shown in figure 5.12, top panel. The blue box in the GeV light cure shows the period during which HESS observations were taken. There were other flaring episodes in this source which could not be observed since they happened during periods the source was either not visible from the HESS site, or had bad-weather. The GeV flare in the beginning of July was overlapping with the full moon period, when HESS does not observe.

5.4.2 HESS data analysis and results

3C 279 had been observed previously in 2007, for ≈ 2.4 hours. Analysis done by other HESS members on that data-set had not indicated any hint for a VHE signal from the

Table 5.7: Results of VHE data analysis on 3C279.

Data Set	T_{eff} (hours)	$<Z>$ ($^\circ$)	E_{thr}^{μ} (GeV)	excess	significance (σ)	UL=I($>E_{thr}^{\mu}$) ($/cm^2/s$)
Jan'09	2.6	29	≈ 300	21	1.	5.8×10^{-12}
All	5	27	≈ 240	89	2.5	8.6×10^{-12}

source. The January, 2009 observations amounted to ≈ 2.6 hours of good quality data. The analysis was done on just the January-2009 flare data set, as well as on all the data available
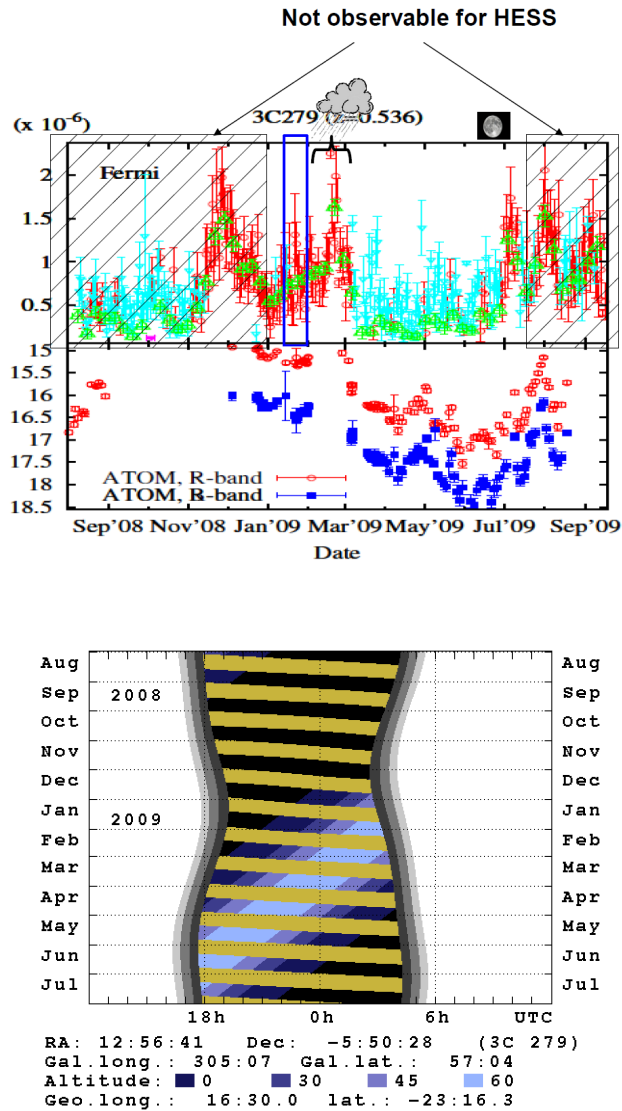
Figure 5.12: **top:** The optical and GeV light curve of FSRQ 3C 279, over a period of roughly one year. The Fermi light curve is from the publicly available Fermi LAT webpage of monitored-sources. The optical light cure is from ATOM monitoring. **bottom:** The visibility window of the source from the HESS site for the year August, 2008 till July, 2009 - generated using the tool by Konrad Bernlöhr (*MPIK, HESS internal web pages*).

on the source. Since this source, like PKS 1510-089 is at a high redshift (z=0.536), I used the soft-cuts ("soft_north_1b" configuration) for my analysis. The analysis procedure of this HESS data set was identical to that done on PKS 1510-089. Except that in this case the runs did not suffer from hardware problems like the ones described for PKS 1510-089 - thus needing no special treatment. The results of the analysis (see table 5.7) do not give a detection. Upperlimits on the integral flux above the effective threshold energy, assuming a photon-index of 5 is quoted in the last column of the table.

The HESS upper limits along with the VHE measurement reported by the MAGIC group is shown in figure 5.13. Since only upperlimits were obtained from these observa-
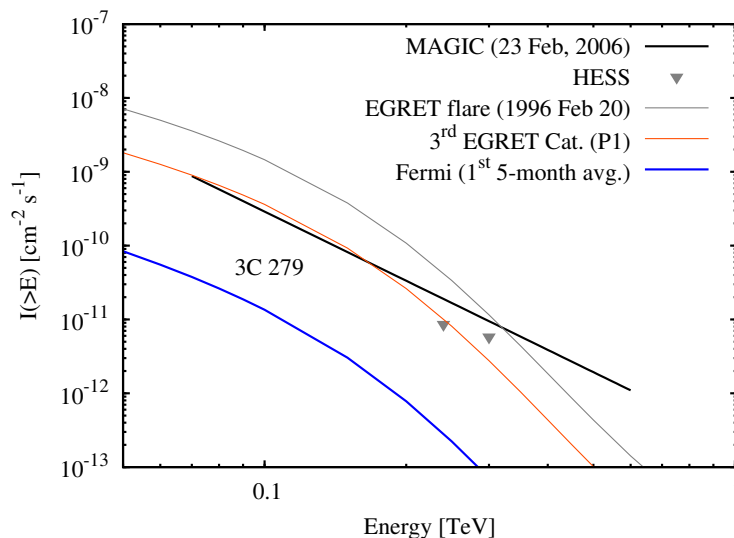
Figure 5.13: The VHE data and extrapolations from GeV instruments for 3C 279, in terms of integral fluxes. The line is the fit to the MAGIC spectrum on the night of 23 February 2006. The gray triangles are upper limits from HESS observations. The left point corresponds to all the data on this source taken with HESS, and the right point is from the data taken only in January 2009. The Fermi extrapolation is from the average spectra of the first 5 months of operation Fegan *et al.* (2009), corrected for EBL using Aharonian-2006 model. The EGRET extrapolations are from the bright flare detected on February 20, 1996 Nandikotkur *et al.* (2007), and the P1 flux from the 3rd EGRET catalog, Hartman *et al.* (1999) corrected for EBL using Aharonian-2006 model.

tions, no detail modelling of the spectrum is possible. The HESS upperlimits are compatible with the extrapolated Fermi first-5-month average flux.

5.5 Conclusion

A more precise measurement of the VHE spectrum though desirable, was not been possible due to the overall small number of photons detected from PKS 1510-089. This is due to the fact that this source exhibits a very soft intrinsic spectral index of around 2.5, hence with the steepening due to EBL absorption the photon statistics from such a source is too low to make a precise measurement of the VHE spectrum covering a wide energy-range. I note here that other sources like PKS 2155-304 and 3C 66A which have published simultaneous GeV and VHE spectra (see section 4.2.2) suffer from other problems due to which a strong contraint on the EBL is not possible. PKS 2155-304, is not very distant ($z = 0.116$). Furthermore it shows a clear break in the GeV band, which can further steepen in the VHE regime, thus increasing the uncertainty on the intrinsic spectrum in the VHE regime. For 3C 66A the redshift is not known. To proceed further with this technique a bright, sufficiently high redshift source with much harder intrinsic spectra is required. From the measurements of PKS 1510-089, I conclude that all the 4 EBL models considered here are compatible with the data.

Effects of EBL extinction

The EBL extinction of the fluxes of VHE blazars fundamentally modifies the observed sample as it allows only the brightest sources with hard photon indices to be detected at progressively high redshifts. It also modifies the observed spectrum by softening it. Therefore in any study of the sample properties of VHE blazars need to take into account the effect of EBL extinction. In section 6.1 a number of Monte Carlo generated VHE parent blazar samples are compared with the true VHE blazar sample to deduce the effects of EBL absorption on the observed spectral trends with redshift. Furthermore, with these Monte Carlo simulations the parent sample properties (viz. the luminosity function, density evolution and intrinsic spectral-index distribution) which might have a discernible effect on the observed sample are studied.

EBL extinction can also be used as a diagnostic tool for other astronomical effects. In the second part of this chapter the sensitivity of EBL extinction to the uncertainty of cosmological parameters is studied. Followed by a estimation of the various sources of error in the estimation of EBL extinction.

6.1 Extracting parameters of the parent-population of VHE blazars

The VHE blazar sample has been studied in some recent publications to discern the effect of intergalactic extinction and estimate sample properties of these sources. In Persic & de Angelis (2008) for example, the authors looked at the spectral trends in VHE blazars and explained the trend with z (or rather the lack of it) by invoking the possibility of a combined effect of a bias towards bright flaring states and the steepening effect of EBL absorption. They argue that flaring states of blazars (likely candidates for the high redshift sources) would correspond to harder spectra according to the SSC emission scenario; but the softening of the source spectra due to intergalactic attenuation would be effectively cancel out this effect.

The VHE blazar sample considered in Persic & de Angelis (2008) was limited to a redshift of 0.25, which is rather low. Subtle effects in the intrinsic spectral index, luminosity-function, or the density evolution of blazars would need a larger sample that extends into higher redshifts. To a first order, the effect of EBL attenuation on the VHE

spectra of a sample of blazars should be insensitive to both the details of the EBL SED as well as its evolution over z (for $z \lesssim 0.25$); since all EBL models essentially result in the same form of the optical depth versus energy (and redshift), i.e. absorption increases with photon energies above around a few $100\,\mathrm{GeV}$ and is proportional to the redshift of the source. Thus as the VHE blazar sample grows and we detect more and more sources over a wide range of redshifts, for which the time averaged spectra can be constructed, we can discern any statistical trend in the observed spectral index with redshift, due to EBL absorption.

It is expected that EBL absorption will result in an overall softening trend of blazar spectra with z, and an overall reduction in the number of VHE blazars with increasing z. The observed number distribution with z, as well as the average spectral index with z will therefore be biased by the effect of EBL extinction.

The true VHE blazar sample has been obtained by detections from a number of different instruments that have different flux sensitivities. The sensitivity of a VHE instrument is a non-linear function of energy. Furthermore the size and multiplicity of the detectors determine the range of energies over which an instrument will be sensitive. This means different instruments will detect sources with different characteristics. This introduces another bias due to the detectors in the observed sample.

Another selection effect which is difficult to untangle is the selection effect in the sample. Since the observed sample is obtained not by a sky-survey, but as a result of a pre-selected list of targets. This selection introduces a bias in the observed sample.

All these biases present in the observed VHE blazar sample will make it impossible to extract the parent sample properties like luminosity function (LF), density evolution (DE) and the intrinsic spectral-index distribution (SID) in a straightforward manner.

The approach followed here is to generate various parent samples by Monte Carlo simulations of the LF, DE and SID. The VHE detectable source sample from these simulations are then compared to the true VHE blazar sample to check what parametrization for the parent-sample properties are compatible with observations. The results are also scrutinized to identify those properties that have a discernable signature in the observations. In this method the EBL extinction effect is taken into account while extracting the VHE detectable source sample from the simulated parent sample. The effect of instrumental bias is also checked. The bias due to selection effect is constrained by requiring that the true VHE blazar sample should be compatible with the simulated VHE sample, i.e the simulated VHE sample should represent a parent population from which the true VHE sample can in principle be derived. For this test, the observed-spectral-index versus redshift, plane is used as the diagnostic plane.

The VHE blazar sample is presented in section 6.1.1.1. The choice of the variations in the parameters used to construct the various parent VHE blazar samples, and the

justification for the same are given in section 6.1.2. To extract the simulated VHE sample from the parent sample, a specific EBL model is chosen to get the EBL absorbed flux of each simulated source. Those simulated sources which have an integral flux (above 200 GeV) greater than the HESS sensitivity for 50 hours of observations (see figure 4.1, right panel) are selected. In section 6.1.3, the results of the simulations are presented, and compared with current observations to test the validity of the simulation parameters. The bias that might arise due to the fact the VHE blazar sample is a result of multiple non identical instruments is also discussed in this section, followed by the conclusions.

6.1.1 Constructing parent sample for VHE blazars

6.1.1.1 True VHE blazar sample

There were 25 reported extragalactic VHE sources at the time this project was done, in November 2008. Of these, there are 17 blazars that have, both, a well measured spectra and a confirmed redshift. A few new sources discovered in the intervening period have not been included in this study. These are presented in Table 6.1 and make up the true VHE-blazar sample used in this study. Of the extragalactic sources excluded in this study, 5 sources (viz. MAGIC J0223+430, 3C 66A, S5 0716+71, 1ES 0806+524, and PKS 0548-322) did not have a reported VHE spectra, when this work was done. Of the other three, M 87 is not a blazar but a FR-I (Fanaroff-Riley, type I) galaxy, PG 1553+113 has no confirmed redshift, and 3C 279, the only VHE-detected FSRQ (Flat Spectrum Radio Quasar), has only been detected during a single night (see Teshima *et al.* 2007), out of all the published data. The 3C 279 detection was probably of an exceptional flare, and is therefore left out of this study. The sources in Table 6.1 have been ordered by redshift, the measured spectral parameters, viz. the observed spectral index and the normalization at 1 TeV, to a simple power-law fit ($\frac{dN}{dE} = N_{0,fit}E^{-\Gamma_{obs}}$) are given in column 4 and 5, respectively. A few of these sources show dramatic variability, the lowest spectra obtained from a literature survey is used here (citations for the spectra are given in the last column of the table), to remove bias towards bright flares. These spectra are affected by absorption due to the EBL. The published fit to the spectrum was deabsorbed using the EBL extinction calculated as a function of redshift and photon energy as explained in section 2.4. The resulting intrinsic spectral indices calculated between 0.2 TeV and 1 TeV, are given in column 6. The EBL limits given in Aharonian *et al.* (2006b) has been used to calculate the relevant attenuation.

The true VHE blazar sample considered here, extends in redshift from z ≈ 0.03 to z ≈ 0.2. Over this range of redshifts the attenuation due to EBL absorption would vary (for example, see Stecker *et al.* 2006, Fig. 4), and it is expected that this should lead to an general softening trend in the spectra of blazars toward higher z. However, it is clear from the values given in column 4 in Table 6.1, and the plots in the figures presented in Section

Table 6.1: The VHE blazar sample, sorted by redshift. The values for the photon indices and the normalization (to a power law fit) at 1 TeV are from the references in the last column. The $6^{t}h$ column gives the approximate calculated values (corrected for EBL absorption) for the intrinsic Γ, and column 7 is the intrinsic luminosity at 400 GeV.

(1) Sl#	(2) Name	(3) z	(4) Γ_{obs}	(5) $N_{0,fit}$(at1TeV) 10^{-13} [cm^{-2}s^{-1}TeV^{-1}]	(6) Γ_{int}	(7) Log[L$_\gamma$] (at 400 GeV) [erg s^{-1}]	(8) Instrument (for spectra)	(9) References
1	Mrk 421	0.031	3.19	380.0	3.0	44.66	HEGRA	Ah02
2	Mrk 501	0.034	2.76	84.0	2.6	43.92	HEGRA	Ah01
3	1ES 2344+514	0.044	2.95	15.5	2.7	43.51	MAGIC	Al07a
4	Mrk 180	0.045	3.25	8.99	3.0	43.42	MAGIC	Al06a
5	1ES 1959+650	0.048	2.72	43.0	2.5	43.95	MAGIC	Al06b
6	BL Lacertae	0.069	3.64	2.37	3.2	43.42	MAGIC	Al07b
7	PKS 2005-489	0.071	4.0	1.66	3.6	43.44	HESS	Ah05a
8	RGB J0152+017	0.08	3.53	4.40	3.1	43.81	HESS	Ah08
9	W Comae	0.102	3.81	6.09	3.2	44.34	VERITAS	Ac08
10	PKS 2155-304	0.116	3.32	20.0	2.6	44.82	HESS	Ah05b
11	H1426+428	0.129	3.55	185.0	2.7	46.00	Whipple	Ho02
12	1ES 0229+20	0.14	2.5	6.23	1.6	44.22	HESS	Ah07a
13	H 2356-309	0.165	3.06	3.08	1.9	44.37	HESS	Ah06b
14	1ES 1218+304	0.182	3.0	101.0	1.7	46.01	MAGIC	Al06c
15	1ES 1101-232	0.186	2.94	5.63	1.6	44.76	HESS	Ah07b
16	1ES 0347-121	0.188	3.1	4.52	1.8	44.75	HESS	Ah07c
17	1ES 1011+496	0.212	4.0	3.20	2.4	45.15	MAGIC	Al07c

6.1.3 that there is no clear spectral-softening trend with redshift in the true sample. This lack of trend is counterintuitive and it could be either due to a bias in the measurements, or due to some peculiar distribution in the properties of the parent blazar sample.

Out of the three properties that are used here to define the parent sample, the DE is independent of the observation wave band. However the LF and SID might be dependent on the observational band. It would be straightforward to use a model for the DE derived from other wave bands, for the parent sample, if such a model exists. The LF and SID can be derived either from direct observations, or, from theoretical predictions using LFs in different wavebands combined with a well established broad-band emission model. The functional forms used for simulating the synthetic parent blazar sample for the three parameters mentioned above are described below.

6.1.1.2 Luminosity function and density evolution

While there are calculation of LFs, and characterization of the DE of AGN in many wavelengths such as radio and X-rays that are derived from relatively large samples (Hasinger *et al.* 2005; Ueda *et al.* 2003) - the sample sizes used for the few attempts to derive such parameters for blazars are rather small (see for example Padovani *et al.* 2007, and references therein). For X-ray, Hasinger *et al.* (2005); Ueda *et al.* (2003), the LF for AGN are well described using broken power laws (BPLs), within the redshift ranges of interest to us, i.e. $0.015 < z < 0.25$. However, these for non-beamed AGN, i.e. excluding blazars from the AGN samples studied therein. In Padovani *et al.* (2007) the sample sizes

are the largest for blazars till date, but the numbers are dominated by FSRQs, unlike the true VHE-blazar sample which is composed, almost entirely of the BL Lac type. Also, this blazar study gives LF for BL-lac objects and FSRQs in the radio wave band and not γ-ray energies. This point need to be stressed, since converting a luminosity (and consequently a LF) observed in radio (for AGN and/or blazars) or in another wavelength like X-rays, to a γ-ray band-luminosity is non trivial due to the following reasons. First of all, the luminosity of non-beamed AGN is assumed to be isotropic, whereas for blazars (the beamed AGN) it is most decidedly not so, and the strong beaming effect needs to be accounted for. This is difficult due to the large range of Doppler factors involved, as evident from the wide scale variability in blazars. Secondly, the radio to X-ray are generally from the first peak in the SED of blazars, the so called "synchrotron component", whereas the γ-rays are from the second component, the so called "inverse-Compton" component. The exact emission mechanism involved in the second component is not clearly identified (see Dermer *et al.* (1997); Ghisellini *et al.* (1996); Mastichiadis & Kirk (1997) for leptonic, and Mannheim *et al.* (1991); Mannheim & Biermann (1992); Mücke *et al.* (2003); Böttcher (2005); Reimer *et al.* (2005) for hadronic scenarios) and might be dominated by different mechanisms in individual blazars. Hence the parameters like the strength of magnetic fields involved, etc. cannot be uniquely calculated; making it difficult to predict the luminosity in the γ-ray band from the luminosities in the synchrotron peak.
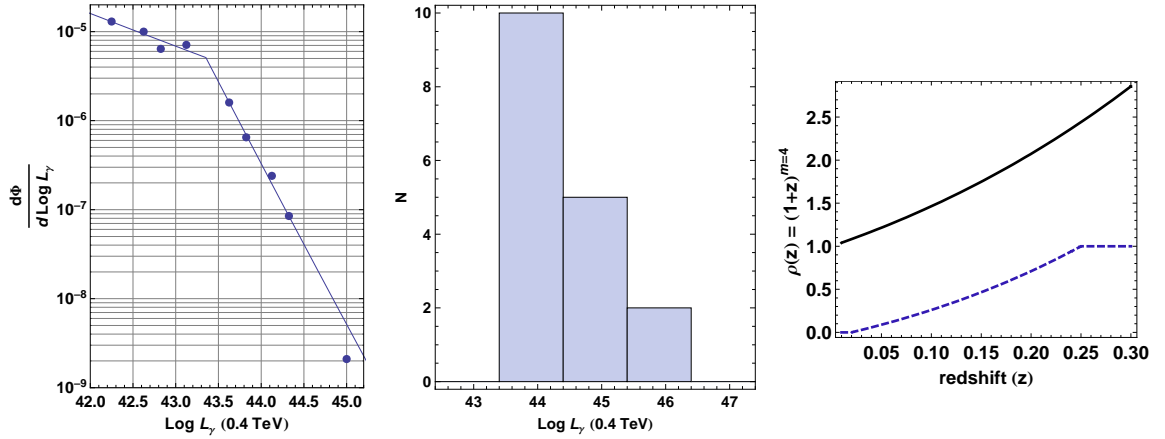
Figure 6.1: ***Left***: Blazar LF adapted from soft X-ray luminosity data from Hasinger *et al.* (2005). The x-axis has been replaced by a VHE luminosity (see text). The thin solid line is our own BPL fit, and is consistent to the LDDE model in the paper for z between 0.015-0.2 (see Figure 4, in Hasinger *et al.* (2005), and the text therein). The value of the slopes of the individual (hard and soft) components of the BPL, are taken as the slopes for the hard and soft SPL, respectively, for the simulations. The BPL in the simulations has the same components with the value of the break energy adjusted to suitable values. ***Center***: The luminosity distribution of the true VHE blazars given in Table 6.1. The luminosity is the approximate intrinsic luminosity at 400 GeV (in erg s^{-1}) calculated from the de-absorbed spectra. ***Right***: The number DE with redshift for blazars is shown in solid, following the DE for low luminosity AGN ($Log[L_x]$ range of $42.0 - 43.0$) in Hasinger *et al.* (2005). The dashed line is the corresponding cumulative-*pdf* for the simulated sample, z between 0.02-0.25.

It is however important to note that blazar LFs in radio, are nevertheless well described by power laws, and so are X-ray LFs (2 component power laws). Since an adequate LF for VHE blazars is not available, a simple powerlaw (SPL) functional form for a LF is used in the simulations. To explore the range a powerlaw can have, a broken powerlaw (BPL) is also tried out, with the contribution from the two components adjusted by using the break luminosity.

Since the simulated parent samples will be tested using the sub sample that's could be potentially detected with VHE instruments this simple approach is adopted in this work. The comparison of the resulting detected-sample to the true-VHE-sample will ultimately be the test for it plausibility. Since SSC emission from seed electrons emitting at X-ray energies, is the usual assumption behind SSC models explaining the VHE emission of HBLs, I decided to pick a X-ray LF as the template. To get a range of parameters for the slope, the following approach was used. The LF used here was assumed with Doppler factor ~ 1 for all sources (this is true for numerous VLBI measurement of jets that measure Doppler factor of the ~ 1). Broad band SED for VHE blazars were studied and it was found that the energy flux (νI_ν) for the X-ray energy used to get the LF given in Hasinger *et al.* (2005) is approximately of the same order as the VHE energy flux at $0.4\,\mathrm{TeV}$ for a number of sources. Thus the luminosity scale of the LF given in Hasinger *et al.* (2005) was adopted for the monochromatic VHE luminosity at the energy of $0.4\,\mathrm{TeV}$. The points shown in the left panel of figure 6.1 are from this X-ray LF. The BPL is the fit to these points derived in this work. The slopes obtained were adopted as the slopes for a BPL fit for the VHE LF, and used as the two extreme slopes for the SPL fit for the simulations done here. The VHE LF used was a in terms of number counts. The spectral-indices being 185 and 36, in the representation. The BPL used in our simulations has the same values for the slopes of the 2 components but with the break energy as a free parameter, constrained such that, the detected sources are not dominated by either of the individual powerlaw components. The LF thus obtained is used as a probability density in the simulations. The luminosity given is chosen to correspond to the isotropic luminosity at $400\,\mathrm{GeV}$, since this is the energy around which the true VHE-blazars have measured spectral information. On comparing with the VHE blazars the range of values in Log[*Luminosity*], assuming isotropy, cover values from 43.4 to 46 (column 7 of table 6.1). Assuming that these values are biased towards bright blazars due to the selection procedure in this sample, the minimum luminosity for the parent samples is set at a lower value: Log[L_γ] < 42.0, at first. For the BPL the break energy was set to a value such that the hard and the soft component were both able to contribute to the total parent sample size. Thus in all, there are three different LFs used for the simulations - two of which are SPLs and one a BPL.

There is no clear agreement for the DE of blazars. It is of the view that X-ray selected blazar samples show a negative evolution, i.e. sources getting fainter or less numerous at higher z (Beckmann *et al.* 2003; Rector *et al.* 2000), where as radio-selected samples show

very little evolution (Stickel *et al.* 1991), i.e. a flat density distribution with redshift. On the other hand all other AGN (e.g. X-ray DE in Hasinger *et al.* (2005)) show very clear positive DE, i.e. sources getting brighter or more numerous at higher z. Since this issue is not resolved, we chose two different DEs functions for our simulations. One is a power law positive DE like that of AGN, picked from Hasinger *et al.* (2005) with power-law index of 4, see Figure 6.1 (right panel), and another is a flat DE.

6.1.1.3   Photon index distribution

The intrinsic SID of the true VHE blazar sample is shown in the left panel of Figure 6.2, along with the best Gaussian fit to it. The true VHE sample is small, and there might be biases involved in the selection of these sources, yet this distribution might still be representative of the parent blazar sample, and is the best available information from direct observations. Therefore the Gaussian fit (with parameters $n_0 = 6.0$, $q_0 = 1.3$, $x_0 = 2.6$, in $f(x) = n_0 \exp[-q_0 (x - x_0)^2]$) to the SID of the real VHE blazar sample, is used as one possibility in the simulations, corresponding to the first column in the results (Figures 6.3, 6.5, 6.6, and 6.7). Qualitatively, alternative distributions of the spectral index that are symmetric (like the Gaussian discussed here), with possibly a different mean value, would not lead to any drastic differences in any spectral trend with redshift, but would only lead to a wider or narrower distribution. Hence this function is representative off all such symmetrical distributions.
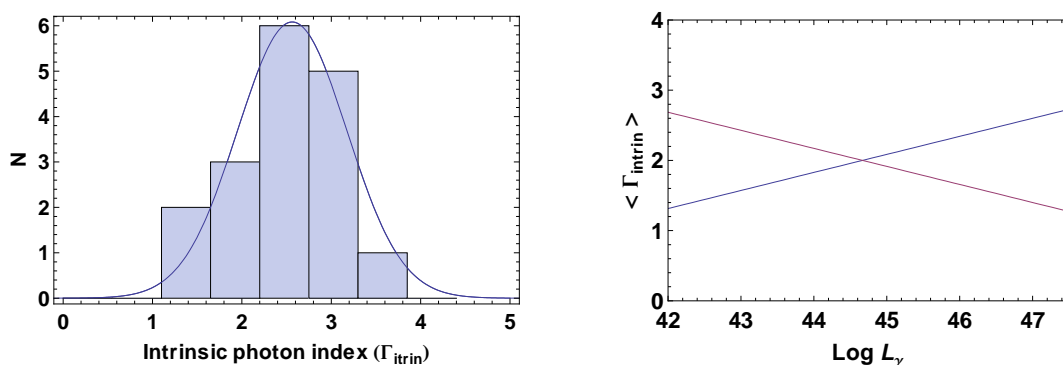
Figure 6.2: *Left*: The distribution of the intrinsic photon index, of VHE-detected blazars (see Table 6.1); curve is the Gaussian fit. *Right*: The dependence of the intrinsic photon index (Γ_{intrin}) distribution, to the logarithm of the intrinsic luminosity ($Log[L_\gamma]$) at 400 GeV, used for the simulations (see text). The functional shape of the Γ_{intrin} distribution is still the same as in the left panel. However mean intrinsic spectral index of the SID, $< \Gamma_{intrin} >$ is related to the $Log[L_\gamma]$. The line with negative slope ($< \Gamma_{intrin} > \propto \frac{1}{Log[L_\gamma]}$.) is consistent with the so called "blazar sequence", where as the line with positive slope tests exactly the opposite relation, i.e $< \Gamma_{intrin} > \propto Log[L_\gamma]$.

It has been suggested in some unification schemes, such as the so called "blazar sequence" (see Fossati *et al.* (1998)), that there might be an intrinsic correlation between the synchrotron peak frequency (as well as the so called "inverse Compton" peak) and the

bolometric luminosity (or intrinsic power) of blazars. This relation, when translated to a VHE band-luminosity (in *log* units) versus intrinsic VHE spectral index, is analogous to an inverse relation between these quantities. By virtue of a true VHE blazar sample we might be able to test if such a relation is in fact true, by measuring a deviation from the expected spectral-softening trend with redshift. This relation is shown in the right panel of Figure 6.2, with a line with the negative slope, and is used for the simulations corresponding to the second column of the results figures in Section 6.1.3. The inverse relation, i.e. the intrinsic VHE spectral index being directly proportional to the VHE band-luminosity (in *log* units), is also tested with the simulations, represented by the line with the positive slope (Figure 6.2, right panel), corresponding to the third column in the results figures in Section 6.1.3.

Thus in all, the two density-evolution functions(a flat and a positive evolution), the three kind of LFs (soft-SPL, hard-SPL, and the BPL), and the three intrinsic-SIDs, give $2 \times 3 \times 3 = 18$ different simulations of the parent blazar sample. The possibility of a peculiarity in the properties of the parent blazar sample, to result in the observed trend (or the lack of) in the true blazar sample is explored (using simulations) in the following sections.

6.1.1.4 Bias due to detector and selection

The attenuated spectrum has to be compared with the detector sensitivity curves to determine which of the simulated sources would be bright enough to be detected in VHE energies. The integral flux sensitivity (figure 4.1, right panel) for the HESS array of IACTs can be used as a typical detector-sensitivity for the current generation of instruments. Other instruments such as MAGIC and VERITAS have a different flux sensitivity, as well as threshold energies. In this work the HESS sensitivity above $200 \, \text{GeV}$ is adopted as the required integral flux level for detection. Thus, for the simulated blazars, an EBL-attenuated integral flux above $200 \, \text{GeV}$, greater than $10^{-12} \, \text{cm}^{-2} \, \text{s}^{-1}$ is considered as detectable at a 5σ level, in $\approx 50 \, \text{hours}$ of observations, using the current generation of IACTs. A few caveats are in order. Firstly, note the shape of the HESS integral-flux-sensitivity considered here (figure 4.1, right panel), and the fact that the curve is derived for a crab like spectrum, i.e. for photon index: $\Gamma = 2.6$. Since the sensitivity curve has a steep dependence on energy, hard spectrum sources will be easier to detect as compared to softer sources. Though, a spectrum that is much harder than 2.5, would correspond to a much lower normalization at $200 \, \text{GeV}$, and it would actually fall below the sensitivity of the instruments at the lower energies, and for the higher energies it will not be detected over a sufficiently wide energy range to give a measurable photon index at $0.4 \, \text{TeV}$, the energy at which I compare all spectra. On the other hand a softer spectra would correspond to a much higher normalization of the differential energy spectrum, which will result in most photons being detected at a narrow energy range at lower energies making it difficult to

derive a spectral index. These issues are discussed later in section 6.1.4.1.

Secondly, the actual blazar sample is derived from measurements taken by a number of instruments, and there might be subtle differences in the VHE-blazar sample detected using a single instrument. This might be critical for blazars that are close to the detection criteria specified above. This effect is expected to be negligible, once a sizable VHE-blazar sample is available to us. The simulations should thus be more or less free from this subtle effect.

6.1.2 Simulating parent blazar samples

The parent blazar samples as defined by the three functions, namely the DE, the LF, and the intrinsic SID are generated using Monte Carlo simulations using the various functional forms as described, in Section 6.1.1.1. The EBL-extinction corrected flux for each simulated blazar, is used to select blazars that can be detected with the current IACT installations. The simulations were done in two rounds.

For a particular source defined by its luminosity, L, its intrinsic spectral index Γ_i and its redshift z the flux reaching earth is calculated as follows. Since the Doppler factor is assumed to be unity, the luminosity is an unbeamed luminosity which gets transmitted isotropically from the source. Thus the flux at $400\,\text{GeV}$ that would reach earth if there were no EBL extinction is given by $F_{0.4TeV} = L/(4\pi d_l^2)$, where $d_l = d_l(z)$ is the luminosity distance of a source at z. The spectrum that would be obtained without EBL extinction would thus have a slope of Γ_i and a normalization at 0.4TeV equal to $F_{0.4TeV}$, i.e. $(dN/dE)_i = F_{0.4TeV}(E/0.4TeV)^{-\Gamma_i}$, where E is the photon energy. This spectrum is multiplied by the EBL extinction function $e^{-\tau(E)}$ which is also a function of photon energy to get actual observable spectrum at earth, $(dN/dE)_{obs} = (dN/dE)_i \times e^{-\tau(E)}$. This function is integrated from $0.2\,\text{TeV}$ to ∞ to get the required integral flux above $200\,\text{GeV}$. If the integral flux is higher than $10^{-12}/cm^2/s$ the corresponding source is counted as a detectable source.

6.1.2.1 Set I: $Log[L_{\gamma,400GeV}] \geqslant 42.0$

The first set was used to test if the initial values used for the for all eighteen permutations of parameter values, were able to generate a detected sample that adequately spanned the diagnostic plane, with no limit on the parent size. Thus the normalization of the LF was adjusted using trial and error, while fixing the minimum luminosity, and the break energy. The diagnostic plane defined by the observed spectral index of sample of detectable blazars versus the redshift was used for this test. Any observed deviation in this diagnostic plane between the simulated detected sample and the true VHE blazars, might result, for example, from a deviation between the parameters of the simulated LFs and the true LF of the blazar parent population. The initial values were - a limiting luminosity

($Log[L_{\gamma,400GeV}] \geqslant 42.0$), and a break energy ($log[E_b] = 43.0$) for the BPL LF. The size of the parent sample was made as big as necessary to have at least 10^3 detections. This was achieved by repeating the simulations with a coarse sampling of the normalization of the LF.

The first round of simulations are shown in Figure 6.3 and Figure 6.5. The results are given in an observed-spectral-index versus redshift representation; the first set, Figure 6.3 corresponds to a flat DE (i.e. no evolution of number density of blazars with z), whereas the second set, Figure 6.5 corresponds to the positive DE as shown in Figure 6.1, right panel. The two other dimensions of the simulated parent sample, i.e. the LF and the intrinsic SID, correspond to the rows and columns respectively, in both figures. The first and second row in both figures, correspond to a hard-SPL luminosity function (slope = 36, as in the left panel of Figure 6.1) and a soft-SPL (slope = 185) luminosity function, respectively. The third row correspond to a BPL LF, with the hard and soft components taking the same values for the slopes as the individual SPLs, described before. The first column (in both figures) correspond to the Γ_{intrin} distribution as per the true VHE blazar sample (see Figure 6.2, left panel); where as the second and third columns correspond to the luminosity dependent Γ_{intrin} distributions, for the two slopes as shown in Figure 6.2, right panel.

6.1.2.2   Set II: *Parent sample size* $< 10^4$

In the second set of simulations, the parameter values were modified to study how these influenced the distribution of the detected subsample in the diagnostic plane, while making some restriction on the parameter values. The restrictions were designed such that they resulted in samples that satisfy the following three conditions - (1) a parent sample size restricted to 10^4 sources, (2) have $\sim 10^3$ detections, and (3) have a "good" coverage over the entire redshift range. The first restriction was due to the belief that blazars constitute a very small fraction of the AGN population. The second restriction was based on the assumption that many blazars are indeed detectable in ≈ 50 hours deep observations, but haven't actually been detected, due to the limitations of the current generation of IACTs. The last restriction is imposed to reflect the observational evidence that the true VHE-blazars sample covers this entire simulated z-range.

The parameters of the LF ($Log[L_{\gamma,400GeV}]$, and E_b for the BPL form) was modified such that the parent sample size was limited to 10^4 sources, while giving at least ≈ 2000 detections. For the SPL only the former parameter is free and needed to be modified. A coarse sampling of the $Log[L_{\gamma,400GeV}]$, and E_b for the BPL form were done to converge to the required values. To scale the results of the simulation down, a subsample 200 blazars were randomly extracted from the ≈ 2000 detections. This allows a better comparison against the small sized true VHE-blazar sample.

To accomplish the objectives of Set II, the the final parameters used for the LFs

were as follows. The same functional form for the hard-SPL was retained as it already satisfied all the conditions mentioned above. The minimum luminosity of the soft-SPL was increased to $10^{44}\,\mathrm{erg\,s}^{-1}$, i.e. $Log[L_{\gamma,400GeV}] \geqslant 44.0$, with the same slope. Though in principle the slope could be hardened, while increasing the luminosity by a smaller value; we refrained, since we intended to explore two extreme limits for the slope as denoted by the hard-SPL and the soft-SPL, and see how the other parameters need to be adjusted to get results consistent with the observations. For the BPL on the other hand, a more dominant harder component was required, hence both the minimum luminosity and the break-energy needed adjustment. The new BPL LF thus had $Log[L_{\gamma,400GeV}] \geqslant 42.5$ with the break-energy, $E_b = 43.25$. With these parameters the simulations were repeated, and out of the ≈ 2000 detections obtained, samples of ≈ 200 were extracted for all permutations; the results are shown in Figures 6.6 and 6.7, for a flat DE and a positive DE, respectively. We elucidate some interesting points below.

6.1.3   Results

The primary detection criteria, namely an integral flux above $200\,\mathrm{GeV}$, greater than $10^{-12}\,\mathrm{cm}^{-2}\,\mathrm{s}^{-1}$, selects the detectable VHE blazars, for each set of simulated parent sample defined by a unique combination of the three simulation parameters. If the true parent sample is analogous to the simulated parent sample, these samples of detectable VHE blazars are thus the results we can expect if a flat sky survey is done using the current generation of IACTs, for $50\,\mathrm{hours}$ deep exposures.

6.1.3.1   Simulation Set I

Considering the simulations for the flat DE first (see 6.1.2.1), we see a clear row-wise segregation of the results, i.e. in the LF parameter. In the individual rows, the columns are also qualitatively different. Thus a cursory glance convinces us that the two parameters, viz. the LF and the Γ_{intrin} distribution, play a fundamental role in characterizing the Γ_{obs} versus z, distribution of the detected VHE sources if the simulations represent the true parent blazar sample. There are some noteworthy details in Figure 6.3 - Firstly, the top row has a dense coverage over the entire redshift range, and seems to have a tight correlation in the Γ_{obs} versus z plane.

Secondly, the hard-LF needed the smallest parent sample size (10^4 blazars) for the required minimum number of possible VHE detections. The parent sample size needed to be increased by ten times for the soft LF, and by five times for the BPL, for roughly $\sim 10^3$ detections. Even then, the redshift range of the detected sources remains restricted to a much lower value than the simulation limit of z $= 0.25$, especially for the soft LF. Since the true blazar sample seems to cover this z-range rather uniformly, we can conclude that both the soft-SPL and the BPL LFs cannot represent the parent sample, at least not
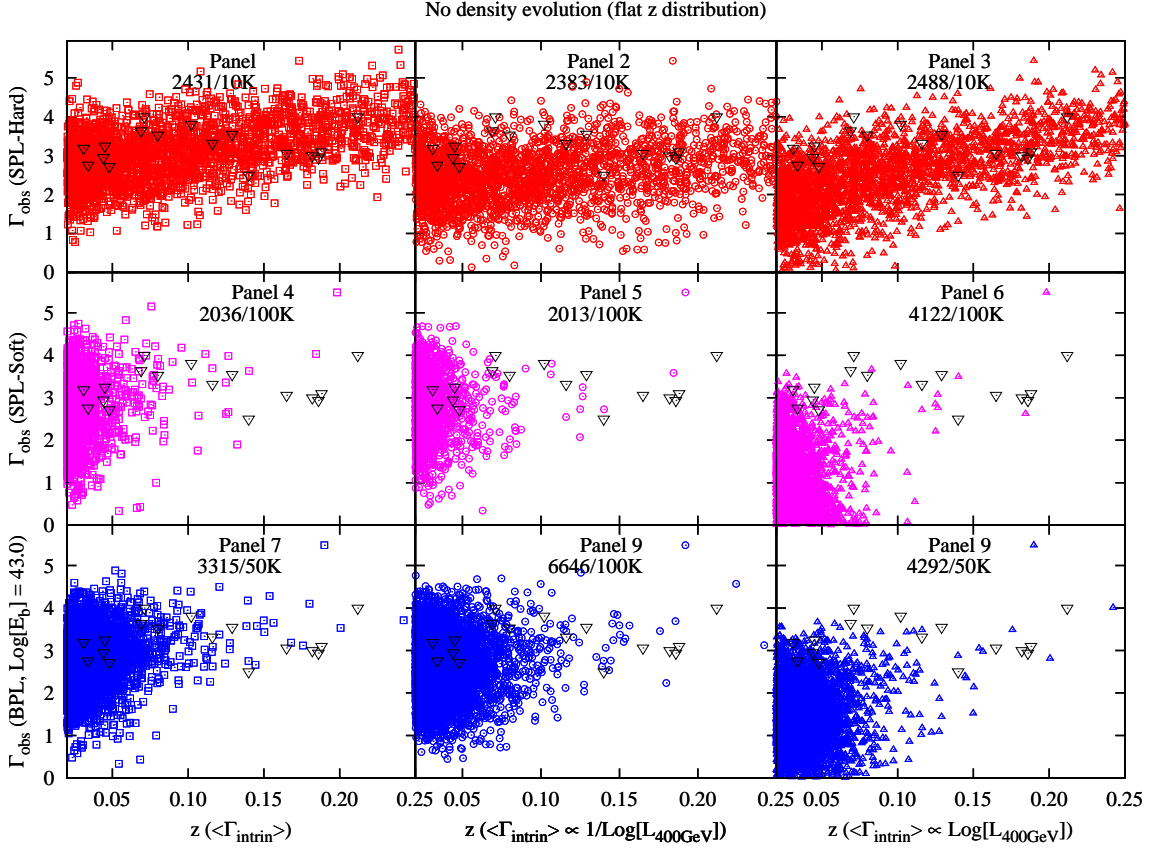
Figure 6.3: Results of simulation for parent blazar samples with a flat DE function. Each panel shows the observed spectral index (Γ_{obs}), versus the redshift. Each panel corresponds to a simulated parent sample, with the given LF (for each particular row), and a particular functional form for the intrinsic spectral index (Γ_{intrin}), as the columns. The numbers in each panel, give the number of detectable sources over the total number of sources for each simulation. The LFs have $Log[L_{\gamma,400GeV}] \geqslant 42.0$, and the Γ_{intrin} distributions are as discussed in the text. The black downwards pointing triangles are the true VHE blazar sample.

with the same characteristic minimum luminosity and break energy as used in this set of simulations. The top row, the hard-SPL LF, could be nearer to the true parent sample, as it gives $> 2 \times 10^3$ detections for a comparably modest parent sample size of 10^4, while covering the entire redshift range, for the same limiting minimum luminosity.

With the same ratio of the parent sample size between row 2 and 3 (i.e. soft-SPL and BPL), the number of detections for panels 6 and 9 (luminosity dependent SID) is much more than panels 4 and 7 (SID as in the true VHE sample). Though the extent in z-distribution seems the same for both pairs. This indicates a luminosity dependence of the SID might offset the low detection level for a soft-LF or a BPL-LF.

Thirdly, a more subtle difference is that, there is a softening trend with redshift for all, except for the middle column. This effect is most clearly visible in the top row. In Figure 6.4, left panel, the mean Γ_{obs} in redshift bins is plotted for all panels. Clear softening is visible for panels 1, 2 and 3, whereas others are rather difficult to follow due
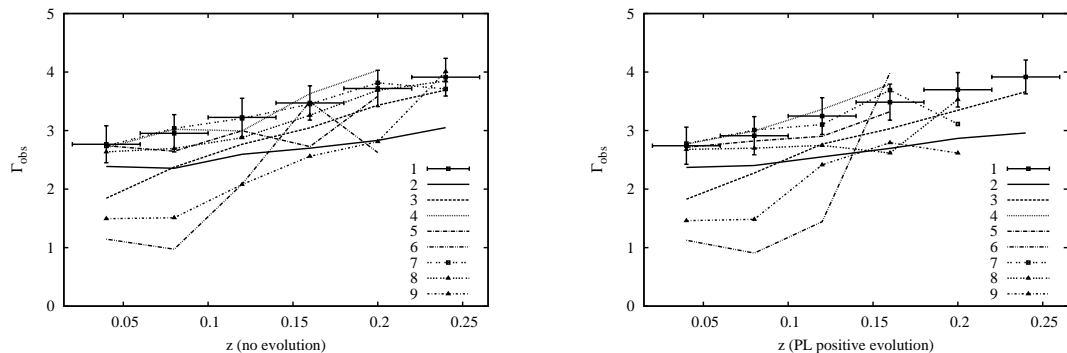
Figure 6.4: The mean of the Γ_{obs} in redshift bins of width 0.04, for the various panels, for a flat DE (**Left**), and for the positive DE considered (**Right**); labels correspond to the respective numbered panels in Figure 6.3. A softening trend with redshift is seen for plots marked 1,2 and 3; but poor statistics in the simulation results does not allow to discern this trend in others. Also note that the plot marked 2, corresponding to panel 2 in the Figures 6.3 and 6.5, shows only a slight softening trend compared to plots labeled 1 and 3.

to lack of statistics in higher redshift bins. Panel 2 lacks a softening trend with redshift, similar to the one seen in the true VHE blazar sample. This could either reflect a true correlation in the parent population properties, in terms of $< \Gamma_{intrin} >$ and the luminosity, or could be due to some bias - either in the selection, and/or the detector characteristics. This point will be discussed in detail later in section 6.1.4.1. The rightmost column in comparison to the leftmost column, especially panel-3 compared to panel-1, shows that the softening trend is even more pronounced for the right-most column. Thus comparing all three columns suggests that a correlation in the luminosity and the SID (via. $< \Gamma_{intrin} >$), could in principle enhance or suppress the softening tend with z, expected due to EBL absorption.

The fourth point to note is that the third row corresponding to the BPL LF, seem to have been dominated by the soft component, from its close resemblance to the second row. Thus to have a suitable coverage in redshift, the parent sample could have a higher minimum luminosity, or have a more dominating hard component (i.e. higher break luminosity); alternatively the soft component needs to be much harder.

Considering Figure 6.5, the simulations for a positive DE; and comparing it to Figure 6.3, suggests that there little qualitative difference in the resulting samples obtained from a flat DE and a positive DE of the form chosen here. Keeping the same values for the combination of LFs and the SIDs in this round of simulations. All the points discussed above for the flat DE qualitatively hold true for a positive DE. A look at the number of detections, however, shows that a positive DE would in general result in a smaller sample of blazars that can be detected at VHE, for the same parent size. This is obviously expected since a positive DE means more blazars at higher z, which suffer greater attenuation due to the EBL, and hence only a smaller fraction from the parent sample are bright enough to be detected. This effect in detection ratio, is however not possible to ascertain without
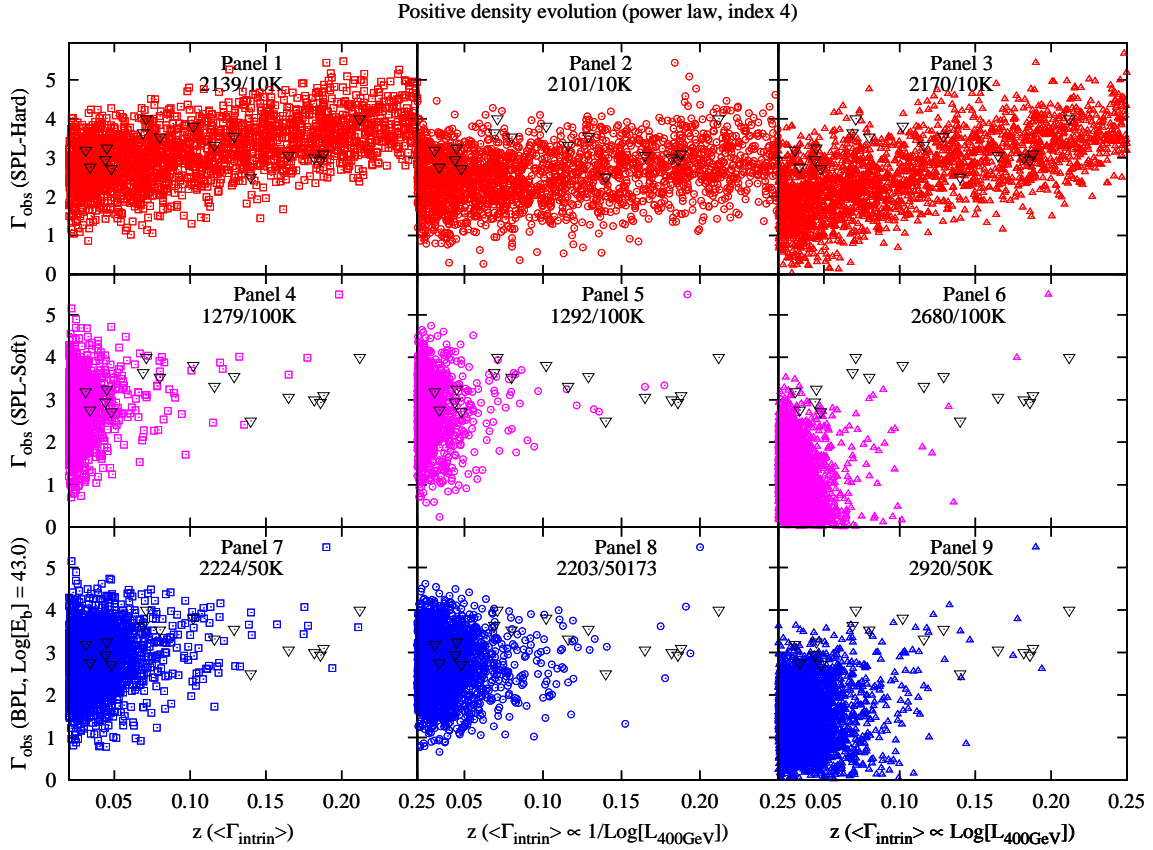
Figure 6.5: Results of simulation for parent blazar samples with a positive DE function, as shown in Figure 6.1, right panel. For a description of the rows and columns see text and Figure 6.3.

the knowledge of actual number counts in this z-range.

6.1.3.2 Simulation Set II

For the second set of simulations (see 6.1.2.2 for the simulation criteria, and figures 6.6, & 6.7 for results): firstly, it is evident that the small number of detections displayed (roughly the same in all panels), cover the entire redshift range, except in panel 4 (Figure 6.6), and the bottom row of the same figure. However, the same panels in Figure 6.7 show that the entire redshift range is more or less well covered, except for panel 8. This is interesting, since this is the only combination where a detectable difference appears due to a difference in the DE parameter.

Secondly, the density of detected sources is higher at lower redshifts for the second and third rows. This is no surprise since flux goes as $1/d^2$, where d is distance to the source, and the attenuation also goes up with redshift - which would make a substantial fraction of blazars too faint, putting those below the detection threshold. Strangely however, for the hard-SPL case (top row), shows very little decrease in the number of detected blazars at higher redshifts, making this a clear observational signature for this particular LF.
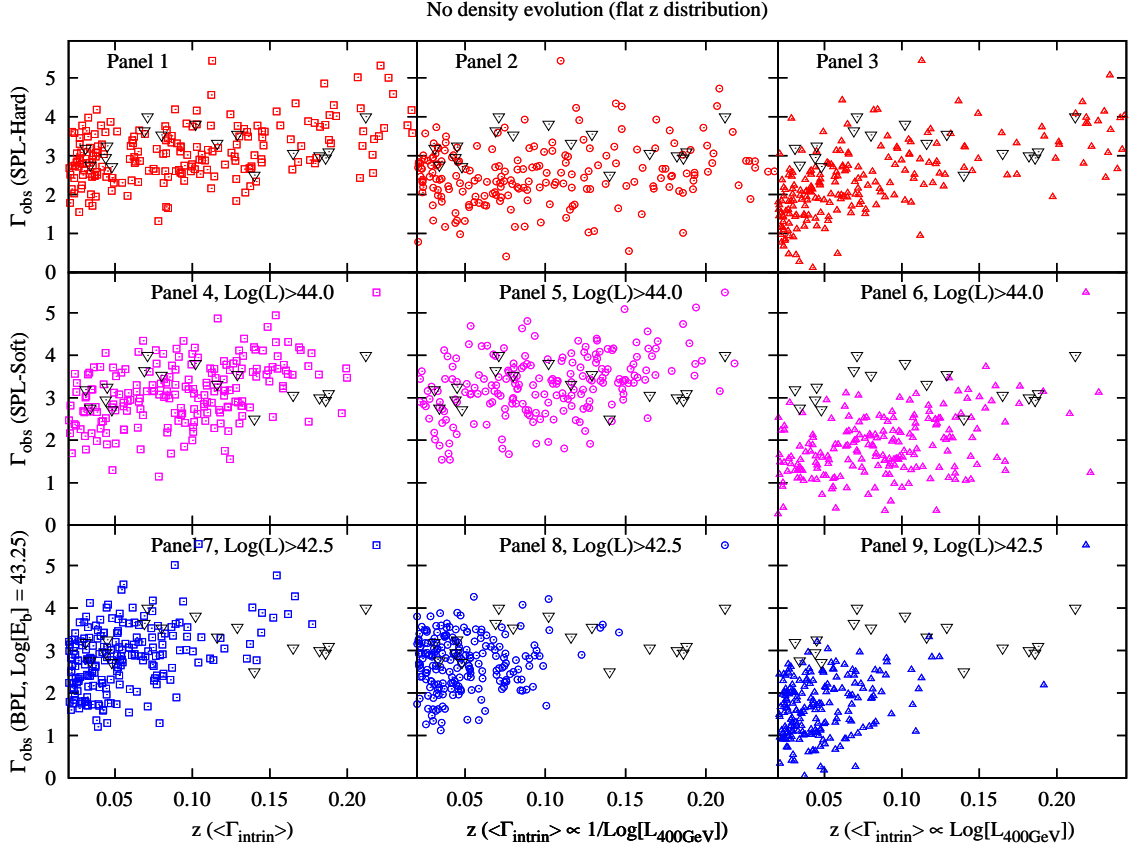
Figure 6.6: VHE detectable sample, of size approximately 200, extracted randomly from the results of the second round of simulations, are shown for a flat DE function. This round of simulations was done with adjusted parameters ($Log[L_{\gamma,400GeV}]$, and E_b for the BPL form) of the LFs, so as to have the detectable subsample, cover the entire simulated z-range, more or less uniformly, as well as limit the parent sample size to 10^4, giving $\approx$ 2000 detectable sources. This was done, since the true VHE blazar sample, Table 6.1, seems to cover the shown redshift range more or less uniformly, up to z = 0.212, and to narrow down the valid ranges for the parent-samples parameter space. The black downwards pointing triangles are the true VHE blazar sample.

Thirdly, as in the first set of simulations, the middle column with the SID having the relation - $<\Gamma_{intrin}>$ inversely proportional to $Log[L_{\gamma,400GeV}]$, is the only panel which shows hardly any spectral-softening trend with redshift, where as all the other columns show a clear sign of a spectral-softening. Thus, this is also a clear observational signature that can be obtained for this particular functional form for the SID. A much steeper slope than the one considered here, would in principle negate or even reverse the softening trend we expect due to EBL absorption. To ascertain this however, any instrumental effect has to be corrected for. If such a trend (or rather, the lack of a softening trend) still remained afterwards, it could be construed as a strong indication of the "blazar-sequence".

Lastly for the third column corresponding to the relation - $<\Gamma_{intrin}>$ directly proportional to $Log[L_{\gamma,400GeV}]$, it is seen that the real blazars and the simulations do not match very well (especially panel 6 and 9). The simulations give much harder $<\Gamma_{obs}>$ in general than the real blazars. To offset this the relation of the corresponding intrinsic SED
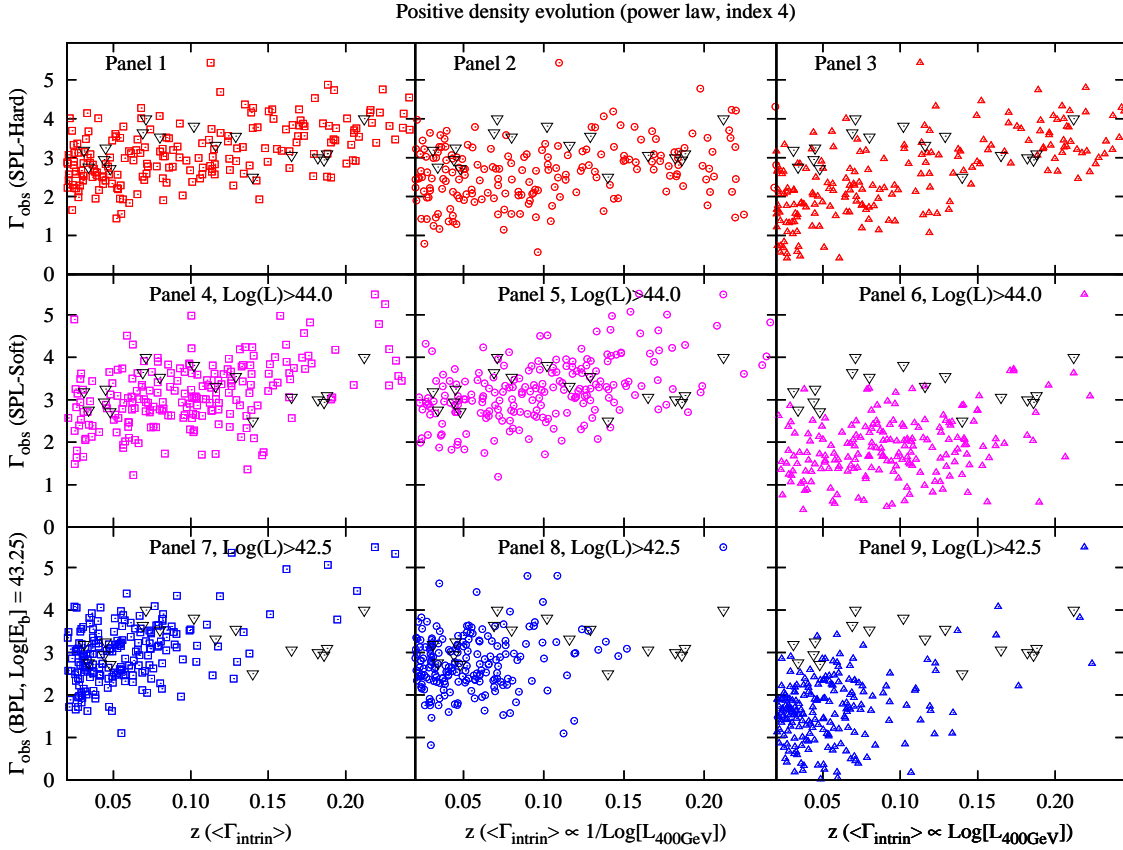
Figure 6.7: Same as Figure 6.6, but for a positive DE function.

(figure 6.2, right panel) could be made more softer, but softer sources would need to be more luminous to have the same ratio of detected sources to the parent sample size. For panel 6 and 9 the LF is already shifted to give brighter sources ($Log[L_{\gamma,400GeV}] > 44.0$), and is inconsistent with the values from the true VHE sources. Therefore I do not apply such a correction to the intrinsic SID in the corresponding simulations.

6.1.4 Discussion

From the previous section, the first set of simulations, indicates that a hard-SPL (or hard component dominated BPL) LF is the most likely blazar LF. This is due to two reasons. One is the generally accepted idea that blazars form a small ($\approx 10\%$) fraction of the AGN parent population, implying a small size for the parent sample. The second, is the fact that we have a VHE blazar sample, obtained from only selective pointed observations, which nonetheless seems to cover the considered redshift range, rather well. This hints that the truly VHE-detectable blazar sample could be much larger, and has not been discovered due to lack of deep enough observations.

The second set of simulations indicate that indeed deviations in the parameters of the parent blazar sample can influence the observed blazar sample. In effect it is seen that

for certain values of the LFs, both a hard and a soft SPL can give detected VHE-blazar samples that cover the entire simulated redshift range. However for a soft LF, to limit the parent sample size to a reasonable number, the over-all luminosity of the sample needed to be very high (i.e the minimum luminosity criterion was: $Log[L_{\gamma,400GeV}] \geqslant 44.0$). This is in direct contradiction to the values calculated from the true sample (see table 6.1), and hence such a soft LF is not acceptable. The effect of DE and SID is less dominant on the observations compared to the LF. However if the true LF follows a BPL form, a positive DE is able to better reproduce the observations that a flat DE.

A softening trend in the Γ_{obs} versus z diagnostic plane due to EBL attenuation, can in principle be suppressed for a unique form of the SID distribution. The SID of the form $< \Gamma_{intrin} > \propto \frac{1}{Log[L_{\gamma}]}$ results in such a suppressed trend. This corresponds to a VHE blazar sample that has harder spectrum for the brighter sources. This is consistent with the "blazar-sequence" which says that blazars evolve with redshift, and more luminous blazars have the peaks at lower energies. An inverse-Compton peak at a lower energy implies that the VHE regime samples the spectra far from the IC peak, and hence will be fainter and softer. Whereas an IC peak near to the VHE regime implies a harder and brighter VHE spectra. EBL attenuation causes fluxes to be fainter and softer, but this effect will be negated if the blazars detected at higher redshifts have harder intrinsic spectral indices. Which will be the case since at high redshifts only the brighter (and hence harder) blazars will be detected.

A reverse relation between the Γ_{intrin} distribution and the $Log[L_{\gamma}]$ (i.e. an intrinsic SID of the form: $< \Gamma_{intrin} > \propto Log[L_{\gamma}]$) results in samples that are much harder (except for the hard LF) than what's suggested by the true VHE sample. Thus such a relation can only hold if the LF of the VHE blazars is reasonably hard.

It should be noted that, the simulations presented here explore but part of the parameter space for the parent blazar sample, and the simplifying assumptions give a tractable approximation for interpreting future VHE-blazar samples. As observations add more VHE-blazars, a clearer picture will surface, and a more restrictive and/or detailed parametrization would only then, be useful.

Since the true-VHE-blazar sample is obtained from observations with different instruments. It is necessary to to rule out any bias the sample suffers due to specific characteristics of the detectors.

6.1.4.1   Bias due to detector characteristics

In this work, the primary detection criterion is an integral-flux threshold at a fixed energy, approximately applicable to all major current generation detectors, viz. H.E.S.S., MAGIC and VERITAS and CTA. The first two - H.E.S.S. and VERITAS have similar energy ranges and sensitivities, where as MAGIC has a lower minimum energy threshold, but is slightly

less sensitive in the overlapping mid-energy range. The energy chosen to characterize
the instrumental sensitivity lies in the overlapping range. As pointed out earlier, the
sensitivity curves used (as shown in Figure 4.1) are for a crab like spectra for the HESS
array of IACTs. For sources with spectral indices near the crab spectral index ≈ 2.6, this
criterion holds very well for the given hours of observation and the required significance for
detection. However, for spectra much harder or softer than the crab spectra, the different
detectors would give different response, mostly due to the difference in the energy range
covered. For instance, the MAGIC telescope has a lower minimum energy threshold but
its sensitivity is not comparable to the HESS sensitivity at higher energies. Thus MAGIC
might still be able to detect much softer sources that have most of their photons in the
$\leqslant 200$ GeV energy range, which might not be detected using H.E.S.S. or VERITAS. While
hard sources that have low flux levels might be detected, only with H.E.S.S. and VERITAS
but not with MAGIC. To a first order, whether a source with spectral-slope much different
from the crab slope will be detected or not, can be determined by calculating the number of
photons a particular instrument can detect (in its detection energy range) in the required
50 hours of observations. This number is proportional to the effective detection area of
the instrument, which in turns depends on the zenith angle of observations, and also the
photon energy. A cut on the detected photon count can be used as an additional detection
criterion. This will be a stricter and more realistic detection criteria, letting us in principle
extract instrument specific samples of detections from simulated parent samples.
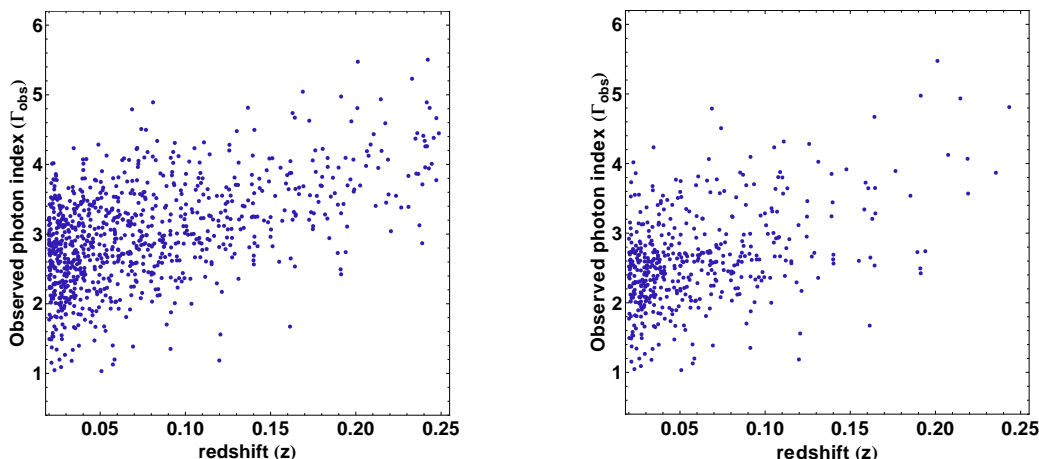
Figure 6.8: ***Left***: A subsample of blazars that pass the primary detectability criterion, for the
BPL LF (approximately same as Figure 6.1, left panel). ***Right***: Remaining blazars from the left
panel after applying additional criterion of at least 10^3 photons to be detected from softer sources
$(\Gamma_{obs} > 2.75)$, in 50 hours of observation at $20°$ zenith angle, with HESS.

To illustrate the instrumental effect on the results of the simulations described in
the previous two subsections, the following test was done on a sample extracted from the
sources that already satisfied the primary selection criterion on the integral flux, figure 6.8,
left panel. The instrument chosen was the HESS array of IACTs, and the sample was for
a BPL LF, with the SID corresponding to the Gaussian SID in figure 6.2, left panel. For a

HESS like array, soft spectra might create problems. Thus for $\Gamma_{obs} > 2.75$, the approximate number of detected-photons was calculated for a 50 hour deep exposure with HESS at an average zenith angle of 20°, like so: (*number of photons*) $= I(> 200\,GeV) \times A_{Eff} \times t_{obs}$, where $I(> 200GeV)$ is the integral flux above 200 GeV, A_{Eff} is the effective area at the given zenith angle, and t_{obs} is the observed time (50 hours), taken in the appropriate units. Though the sensitivity plot shown in the right panel of figure 4.1, required a minimum of 10 photons (for integral fluxes in the higher energies), we use a requirement of a minimum of 1000 photons to be detected above 200 GeV, so that a well measured spectrum can be derived for each source. The effective area given in Aharonian *et al.* (2006c) were used for this purpose. The results of this secondary selection criterion are shown in Figure 6.8, right panel. It is clear that a number of soft sources fail this criterion and are filtered out in the right panel, but the spectral softening trend seen in the left panel still clearly remains. Thus qualitatively we can conclude that though the detector limitation reduces the number of detections, it has no strong systematic effect and an observable trend would still remain. However, this would only be visible with a significantly higher number of VHE detections at z $\gtrsim$ 0.15 than currently available to us. Thus the current lack of trend in the true VHE blazar sample cannot be attributed solely due to instrumental effects.

This conclusion would presumably be valid for the VERITAS array, but for the MAGIC array only sources that are harder and at the same time fainter, could possibly cause deviations from the results presented here. An analogous secondary detection criterion could be constructed for MAGIC, but since most faint sources are detected only if they are relatively nearby, a spectral-softening trend at high redshift would not be affected.

6.1.5 Conclusion

MonteCarlo simulations were used to generate a number of parent samples of blazars with specific forms for the LF, the DE and the SID. The subsample of these which had fluxes detectable with the current generation of VHE instruments was extracted. This extracted subsample of the simulated blazars should If the true VHE blazars are consistent

A number of parent populations of blazars were generated by MonteCarlo simulations of the chosen functional forms for the LF, the DE and the SID. Form each parent sample the sources which had fluxes (corrected for EBL extinction) that are detectable with the current generation of VHE instruments were extracted. The simulation size was chosen so as to render a synthetic VHE blazar sample (SVBS) that is roughly 10 times as big as the true VHE blazar sample (TVBS). This SVBS should in principle be the parent sample from which the TVBS comes from. If the TVBS is not consistent with a particular rendering of the SVBS, this SVBS as well as the corresponding combination of LF, DE and SID for the parent blazar sample (PBS) can be ruled out.

By using this scheme, I conclude that:

(1) The true VHE-blazar sample is consistent with a synthetic VHE-blazar sample that shows a clear spectral softening with redshift (Panel 1 in figures 6.6 and 6.7); therefore *the lack of a distinct softening trend in the TVBS is attributed to its small size, that does not allow to test a spectral trend, due to bias in the observations.* Thus a correlated hardening in the intrinsic source spectra with increasing z, cannot be concluded due to this lack of a softening trend.

(2) The simulations suggest that *a powerlaw form of the LF for the parent blazar sample will have a hard slope.* A steep LF, requires very luminous sources to yield samples covering the high redshifts, which is inconsistent with the available data. A broken powerlaw LF would need a dominating hard component to be consistent with observations.

(3) Combining a hard LF, with specific forms for the intrinsic SID distribution gives SVBSs that are consistent with the TVBS, that show clear features in the Γ_{obs} versus z plane.

        i. *A SID with the relation corresponding to the blazar sequence gives no spectral softening with redshift.*

        ii. *A SID with the opposite relation shows a more pronounced softening trend* than the previous one as well as the SID distribution following the true sample.
A larger TVBS is required to confirm these possibilities.

(4) *The effect of a DE cannot be distinguished, unless the LF is actually much steeper* than the hard-LF considered here, *in which case a positive DE is required* to account for the blazars detected at high redshifts.

6.2   Can cosmological parameters be constrained using EBL extinction?

Measuring cosmological parameters is usually done in one of the two following ways - (1) using standard candles as cosmological probes, and (2) precision measurements the cosmic microwave background (CMB). Recent results using a combination of such strategies has succeeded in measuring the values of cosmological parameters with a high degree of precision. Using the attenuation of the VHE spectra of extragalactic sources, an independent constrain on some of the cosmological parameters such as the Hubble constant (H_o), the cosmological density parameter for matter (Ω_m) and dark energy (Ω_Λ), can be made.

For sources at non-negligible redshifts (z $\geq$ 0.2), the changes in the photon density which directly influences the attenuation-level, depends on cosmology. The optical-depths' dependence on cosmology come from two terms in its calculation - (1) the proper photon-density of the EBL, which depends on the cosmological volume, and (2) the integration along the line-of-sight, which has a dl/dz term - a function of the cosmological parameters (Hubble constant - H(z), Ω_m and Ω_Λ, implicitly assuming a dark energy and matter

dominated cosmology). The first factor is taken into account in the models used to derive the EBL density. The dependence on the second factor can be used in principle to trace the cosmological evolution via the VHE-flux extinction in blazars. This requires a model of the intrinsic spectra of the γ-ray sources, and a model of the EBL photon-density. In Blanch & Martinez (2005), the authors explored the possibility of using the γ-ray horizon (GRH, defined as the VHE photon energy at which the extinction equals e, i.e. a 1 e-fold factor) as a measurement tool for probing cosmology. However the GRH will lie beyond the energy ranges that VHE instruments can probe, for sources with very small and very large redshifts. Furthermore for very nearby blazars the GRH will be at high VHE energies where the intrinsic blazar spectra is difficult to constrain, due to possible cutoffs from Klein-Nishina effects. We use a different parameter to circumvent these issues, and test the possibility of discerning a change in the cosmology via EBL extinction.

6.2.1 EBL-extinction parameter relevant for cosmology

VHE γ-rays are absorbed in the inter-galactic medium via pair-production mechanism, from photon-photon scattering on the extragalactic photon field. The optical depth due to pair production from the $\gamma_{CIB} + \gamma_{VHE} \rightarrow e^- + e^-$ interaction is given by:

$$(6.1) \quad \tau(E_o, z_s) = \sigma_T \int_0^{z_s} dz \frac{dl}{dz} \int_{\epsilon_{min}}^{\epsilon_{max}} d\epsilon \{(1+z)^3 \times\ n_\epsilon \left(\frac{\epsilon}{1+z} \right) \sigma_{\gamma\gamma}[s = 2E_o(1+z)\epsilon] \}$$

where E_o is the observed γ-ray photon energy from blazar at $z = z_s$, $n_\epsilon(\epsilon, z)$ is the co-moving EBL density, and $\sigma_{\gamma\gamma}[s]$ is the $\gamma - \gamma$ interaction cross-section (integrated over all angles) as a function of the center of mass energy, and σ_T is the Thomson cross-section. The cosmological parameters go into the expression dl/dz as:

$$(6.2) \qquad \frac{dl}{dz} = \frac{c}{H_o(1+z)\sqrt{\Omega_m(1+z)^3 + \Omega_\lambda}}$$

where H_o is the Hubble constant at $z = 0$ and Ω_m, Ω_Λ are the matter and dark-energy density parameters respectively. This expression is assuming ΛCDM cosmology, and neglecting the radiation density Ω_r.

To derive constrains on the parameters H_o, Ω_m and Ω_Λ, it is necessary to have an estimate on the uncertainty in the EBL density and the intrinsic blazar spectra. A set of attenuation curves for sources at various redshifts is shown in figure 6.9a for the EBL model taken from Aharonian *et al.* (2006b). This EBL model is based on reasonable assumptions on the intrinsic spectrum of blazars and are realistic upper limits on the EBL photon density. Franceschini *et al.* (2008) on the other hand can be considered as a theoretical lower limit. A comparison of the attenuation for a $0.4\,\mathrm{TeV}$ γ-ray photon from various source redshifts calculated using these two EBL models is shown in figure 6.9b. This can be considered as the uncertainty in the parametrization of the EBL density. To
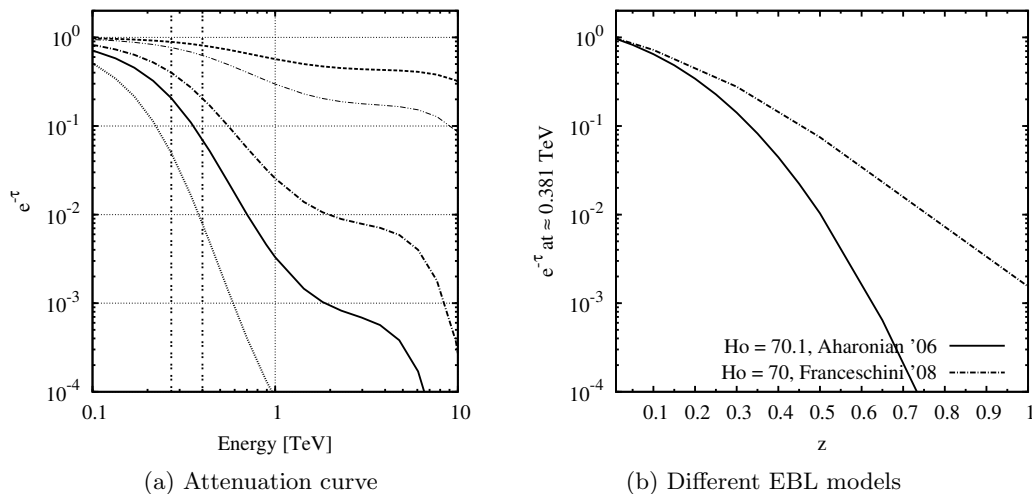
(a) Attenuation curve

(b) Different EBL models

Figure 6.9: ***left:*** The attenuation as a function of the observed γ-ray energy for a number of redshifts. Top-most dashed curve is for z = 0.05, below which are curves for z = 0.1, 0.25, 0.35 and 0.5. ***right:*** Comparison of two different EBL models. The solid line is for the EBL upper limits derived from observations of VHE-blazars (used in the work presented here), and the dashed-dotted line is for an EBL model derived from theoretical models combined with direct source (contributing to the EBL) observations.

derive meaningful cosmological constrains this uncertainty in the EBL has to be resolved eventually. Apart from direct measurements that are problematic due to strong foreground contamination (see Hauser & Dwek (2001) for review) the only viable method is through VHE observation of more blazars at higher redshifts. This is a definite possibility in the near future since new IACT instruments are currently under construction (H.E.S.S. 2) that would increase the sensitivity in the VHE regime enable us to probe deeper in z. Future experiments like CTA and AGIS will further increase this capability. This combined with Fermi will help constrain the intrinsic spectrum of blazars. Under this assumption we can start out with any one EBL model as a prototype to study possible constrains on the cosmological parameters. Since we expect the EBL density to be resolved with VHE observations I take the current upper limits derived in Aharonian *et al.* (2006b) as the prototype for this study.

To proceed with my estimate the measurable parameter that should be used as the proxy to probe cosmology needs to be established. This parameter will obviously be a function of the attenuation, which is a directly measurable quantity. The criteria that this proxy-parameter should satisfy are the following: (1) it should have good dynamic range, (2) should also be clearly measurably over a sufficiently large z ($z = 0.5$), and (3) it should be least affected by systematic uncertainties in the EBL density as well as intrinsic VHE parameters. Since blazar spectra will get steeper with z (due to EBL absorption), as per the second criterion, the extinction parameter should be measurable with IACTs at around ($< 1 TeV$) where the instruments are most sensitive. To make sure that we get a good dynamic range, energies lower than ≈ 0.25 TeV should be avoided (see figure 6.9b). These requirements rule out using the gamma-ray horizon since it easily

exceeds this range ($0.25\,\mathrm{TeV} < E < 1.0\,\mathrm{TeV}$) for very low and high redshifts. Thus the attenuation measured at an intermediate energy of $0.4\,\mathrm{TeV}$, i.e. $\eta(E_o, z) \equiv \exp[-\tau(E_o, z)]$ (where τ is the optical depth to a γ-ray with energy $E_o = 0.4\,\mathrm{TeV}$, for a source redshift of z) satisfies all our criteria. Furthermore, note that the attenuation between $0.27\,\mathrm{TeV}$ and $1\,\mathrm{TeV}$ is approximately a linear relation, in $\log(\eta)$-$\log(E)$ representation; thus a powerlaw intrinsic spectra will produce a powerlaw observed spectra. This will be useful to reduce the systematics on the intrinsic spectral parameters (such as the hardest possible intrinsic-spectra, and turn-offs), by looking at a large VHE-sample in the future.

6.2.2 Sensitivity of the extinction parameter within the uncertainties in H_o, Ω_m and Ω_Λ

To test the sensitivity of $\eta(0.4TeV, z)$ within the range of the uncertainty in the parameters, H_o, Ω_m and Ω_Λ, I calculated the dispersion in $\eta(0.4TeV, z)$ versus redshift. I assume for now that there is no uncertainty on the EBL density, and the measurement error on $\eta(0.4TeV, z)$ is very small. I proceed as follows: keeping two of the cosmological parameters fixed, the third one was assigned three possible values (i.e. the measurement of the varied parameter, from WMAP5, $\pm$ the 3σ error on this value) one after the other. The values obtained for $\eta(0.4TeV, z)$ for each case was compared. The WMAP5 values were taken from `http://lambda.gsfc.nasa.gov/product/map/current/params/lcdm_sz_lens_wmap5_bao_snall.cfm`). This was repeated for all three parameters. The resulting dispersion in $\eta(0.4TeV, z)$ scaled to the attenuation calculated at the measured values of all three parameters ($H_o = 70.1\,\mathrm{km/s/Mpc}$, $\Omega_m = 0.279$ and $\Omega_\Lambda = 0.721$) is shown in figures 6.10a, 6.10b and 6.10c. As seen, H_o and Ω_m show a bigger effect on $\eta(0.4TeV, z)$, than Ω_Λ, with $\approx 10\%$, 5% and 2.5% effect at a redshift of 0.5 for the three parameters respectively.

To see the effect of a measurement uncertainty on $\eta(0.4TeV, z)$, I defined a relative sensitivity parameter $s(p)$ as a function of the fractional change in $\eta(0.4TeV, z)$ times the inverse of the error on the measurement of $\eta(0.4TeV, z)$, i.e.

$$(6.3) \qquad s(p) = \frac{\Delta\eta_{\delta p}(0.4TeV, z)}{\eta_p(0.4TeV, z)} \times [\eta_{Err}(0.4TeV, z)]^{-1}$$

- where $\Delta\eta_{\delta p}(0.4TeV, z) = \eta_{p\pm\delta p}(0.4TeV, z) - \eta_p(0.4TeV, z)$; $\eta_{Err}(0.4TeV, z)$ is the measurement error which we varied linearly between arbitrarily chosen values of 5% at $z = 0.05$ to 15% at $z = 1.0$. The measured cosmological parameter and the measurement error is denoted by the subscripts, $p\pm\delta p$. The errors of 5% and 10% on $\eta_p(0.4TeV, z)$ was based on the assumption that the larger attenuation at higher z will result in lower measured VHE fluxes. This will increase the larger statistical errors on the measured flux, and thus the error on $\eta_p(0.4TeV, z)$ will also increase with z. Of course this is based on the assumption that the uncertainty in the EBL is negligible.

(a) H_o

(b) Ω_m

(c) Ω_Λ

(d) Sensitivity
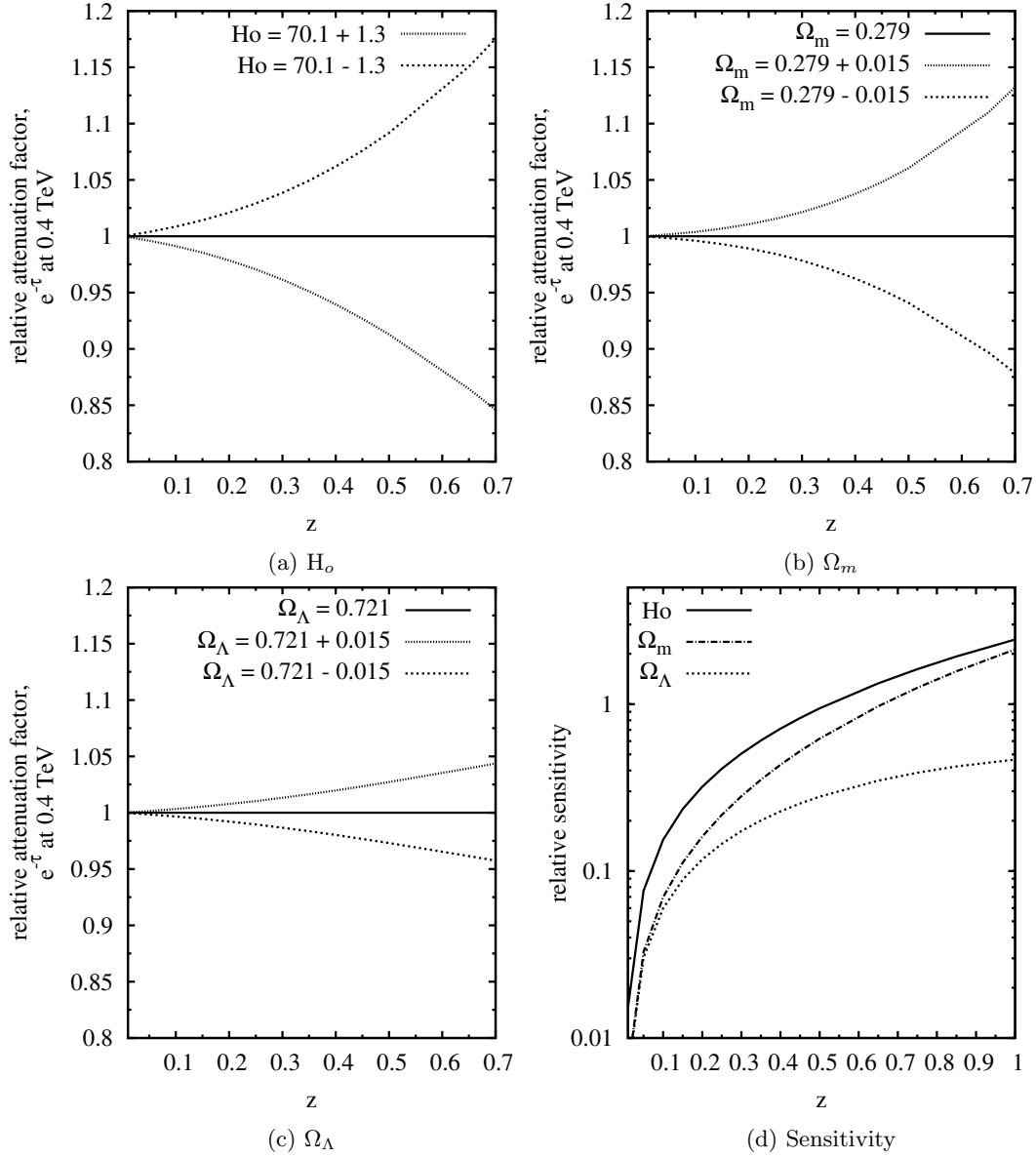
Figure 6.10: The change in attenuation factor with redshift (for a particular cosmology, defined by the three cosmological parameters used here), relative to the cosmology defined by $H_o = 70.1$ km/s/Mpc, $\Omega_m = 0.279$, and $\Omega_\Lambda = 0.721$ (horizontal line). The effect of variation due to errors in the known value of: H_o (***top-left***), Ω_m(***top-right***), and Ω_Λ(***bottom-left***). ***Bottom-right:*** The relative sensitivity, 's' (see text) of the parameter $\eta(0.4 TeV, z)$, to changes in each cosmological parameter, with redshift is shown.

We see that the sensitivity for the various parameters (see figure 6.10d) vary similarly with z, though to a different degree in all three. It should be noted that the sensitivity increases rapidly at low redshifts, and continues to steadily rise at large z. Thus this method has potential to probe the cosmology to the largest redshift that can be reached with IACT experiments.

6.2.3 Conclusion

All this hinges on the assumption that the EBL is essentially known. That might be possible in the future, however at this point the sensitivity of EBL measurements to cosmology has to be compared to the present uncertainties in EBL. As mentioned earlier in this section, we can approximate this uncertainty to be the order of the difference in two plausible EBL models that give maximum difference in attenuation. For our purpose here, I choose the Franceschini *et al.* (2008) and Aharonian *et al.* (2006b) shown in figure 6.9b as the rough indication of the EBL uncertainty as it stands now. For a source redshift of 0.5, the extinction computed by these two models for photon energy of 0.4 TeV is different by a factor of almost 10. This is an order of magnitude larger than the effect of the uncertainty in the cosmological factor, on the extinction (considering a particular EBL). This means that the uncertainty in the EBL needs to be brought down by an order of magnitude, before the uncertainties in the cosmological parameters can be constrained using this method. In the near future, this uncertainty in EBL will be much reduced by a combination of satellite and future IACT instruments, making studies shown above feasible. For now, it should be stressed that this method would provide an independent measurements on these cosmological parameters.

Conversely, since the error on the EBL extinction due the error on cosmological parametes is small compared to the uncertainty on the EBL density - the effect of cosmological uncertainty in the EBL extinction can be safely neglected.

6.3 EBL evolution

The EBL photon density changes with redshift, since it the the integrated starlight light from $z = \infty$ to $z = z_0$. This is referred to as the evolution of the EBL. In contrast the cosmological evolution of EBL is the change in number density due to the expansion of the universe. For VHE blazars The EBL evolution is usually ignored since the relevant redshifts are small ($z < 0.25$), making the effect negligible. However with the future experiments it will be possible to detect blazars with redshift > 0.5. In this section taking one of the recent EBL models, Franceschini *et al.* (2008), the regime where this assumption fails is explored quantitatively. This effect is compared to the effects discussed in the previous section.

In Franceschini *et al.* (2008) a the z-dependant optical depth is provided. If the EBL density at $z = 0$ is denoted by $n(\epsilon)_{z=0}$ - the evolution in the EBL can be ignored by calculating the optical depth at various z, with the $n(\epsilon)_{z=0}$ as the comoving EBL density. The proper density used in the optical dept calculation would then be $[n(\epsilon)_{z=0} \times (1+z)^3]$. In figure 6.12 the extinction as function of z, is shown for 0.4 TeV (color lines) and 0.1 TeV photons (gray lines), for EBL versions with and without evolution. For comparison the

Aharonian *et al.* (2006b) which does not consider EBL evolution is shown (only for 0.4 TeV), which is very similar to the non evolving Franceschini-2008 EBL. In the inset
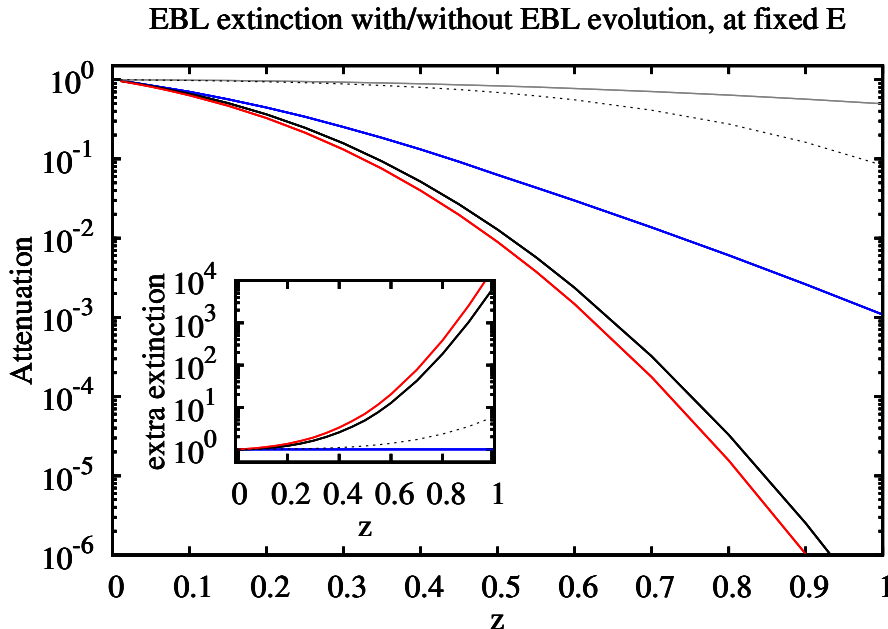

Figure 6.11: The blue/black line is the extinction of 0.4 TeV photons with/without EBL evolution according to the Franceschini-2008 model. The red line is for the Aharonian-2006 model which has no EBL evolution. The gray lines are for photons of 0.1 TeV, solid line is with evolutions and dotted line is without. The inset is the ratio of extinction for non evolving models to the evolving model of the same energy. The inset shows the extra extinction factor when ignoring evolution.

the ratio of the extinction of the non-evolving EBL to the evolving EBL is shown. This is the factor by which we would overshoot the extinction by not taking EBL-evolution into account.

Considering the curves for the 0.4 TeV photons, it is clear that neglecting the evolution below $z = 0.5$ results in a factor of ≈ 5 in the extinction correction. This factor increases rapidly to ≈ 10 at $z = 0.6$ and $\approx 10^4$ at $z = 1$. Comparing the 0.1 TeV to 0.4 TeV curves it is evident that this factor has a steep energy dependence. Thus for spectra measured at energies above a few hundred GeV, EBL-evolution should be taken into account for sources with $z > 0.5$.

Comparing to the fractional change in extinction within the errors on cosmological parameters (see figure 6.10 a, b and c), it is clear that the effect of EBL-density evolution is overwhelmingly large. Thus the effect of cosmological uncertainties is again found to be negligible compared to the redshift evolution of the EBL density.

Furthermore the redshift at which we can no longer ignore the redshift-evolution of the EBL strongly depends on the VHE energy of the measurement in question. As a rule of thumb EBL evolution cannot be ignored even for γ-ray energies > 0.4 TeV, for $z > 0.5$.

6.4 Uncertainty in EBL models

Estimation of the EBL extinction of VHE spectra has a uncertainty due to the uncertainty in any EBL model. One way of quantifying this uncertainty can be done by taking the range of extinction values all viable models give, as shown before in section 6.2, see figure 6.9b. Another way would be to take a particular model that constructs the EBL density at various redshifts from taking different realizations of the contributing components, and interpret the different resulting EBLs as the range of the uncertainty. Such a model is given in Kneiske *et al.* (2002) and Kneiske *et al.* (2004), where different star formation rates (SFR) and the UV escape fraction are considered and a number of EBL realizations are constructed corresponding to different proportions of the contributing components.

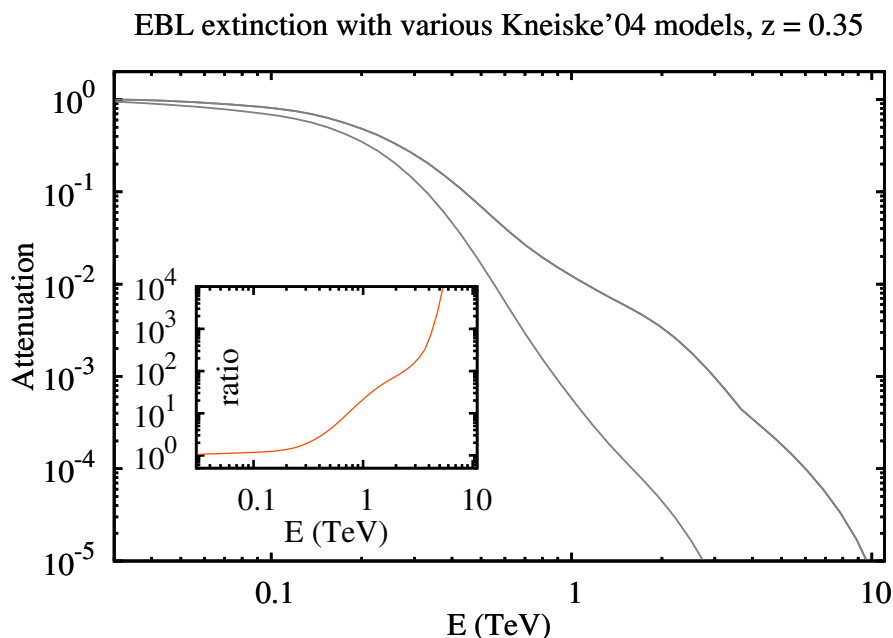### EBL extinction with various Kneiske'04 models, z = 0.35

Figure 6.12: The maximum and minimum EBL extinction for the EBL models in Kneiske *et al.* (2004), versus energy is shown for a source redshift of 0.35. Inset shows the ratio between these two extremes, in other word the effective error due to the different uncertainty in the modelling.

There are six such EBL realizations that are given by the authors, denoted as - (1) best-fit model, (2) warm-dust model, (3) low-IR model, (4) low-SFR model, (5) stellar-UV model, and (6) high-stellar-UV model. To associate an uncertainty to this method of calculating the EBL, I take the minimum and maximum optical depth provided by these 6 models for a range of energies, at a particular redshift. I chose the redshift to be 0.35, the resulting range of attenuation values are shown in figure 6.12. Thus the gray curves show the range of EBL extinction or in other words the error on the extinction versus the γ-ray photon energy for a source at $z = 0.35$. the factor by which the VHE flux of a source can be off given that these are the uncertainties is shown in the figure inset. For the given redshift within these error on the EBL the flux can be different by a factor of ≈ 10 at 1 TeV and to over a factor of 10^4 at 5 TeV. This is much larger than the typical

systematic error of $\approx 20\%$ on the differential flux measured by VHE instruments.

Therefore it is concluded that the uncertainty in the amount of EBL extinction will be the largest source of error in any physical model used to describe the VHE emission of extragalactic sources.

Part IV

Summary and Outlook

7.1 Thesis Summary

In this work two ways to identify flares in blazars were explored with the intention of using the flares to trigger HESS and discover distant blazars. The methods were to monitor blazars in the optical wavelength using ATOM, described in chapter 3; and to use flare information in the GeV band from γ-ray satellites, described in chapter 4. To achieve the former, a robot software was written for the ATOM instrument, which executed a nightly observation schedule. This software was installed in late 2006 and has been operational since. ATOM was used to monitor blazars chosen from a GeV catalog, namely the 3rd EGRET catalog and later the bright FGST sources as well. Apart from triggering HESS, the long term optical measurements from ATOM were compared to the FGST, GeV measurements for the list of blazars from the *FGST monitored sources*. For the 10 sources compared, a dichotomy was found in the flux$_{optical}$-flux$_{GeV}$ plane. Source had either bright in optical but dim in GeV, or were dim in optical while being bright in GeV. This dichotomy was also valid for the z of these sources - with the optically bright sources (dim in GeV) with low redshifts ($z < 0.2$), and the optically dim sources (bright in GeV) at higher redshifts ($z > 0.35$), This relation cannot be trivially explained due to the inverse square relation of flux with distance. Furthermore some sources showed a clear correlation in the fluxes in the two bands, while some sources had no clear correlation. According to the SSC scenario those sources which showed correlation might be the ones which are shining in the optical and GeV bands due to emission from the same particle population, whereas this would not be true for the sources which do not show this correlation.

A specific case for optical-TeV correlation was found for the HBL PKS 2155-304, in a MWL campaign, Aharonian *et al.* (2009). In section 3.3 the probability of getting such a correlation by chance was tested. The effect of measurement errors on the quantification of the *Pearson's r* was evaluated. It was found that the high correlation seen in this data set was consistent with a true physical correlation, though the effect of having this by chance cannot be completely ruled out due to the high duty cycle of this source.

In chapter 4 the second scheme to discover distant VHE sources by follow up observations of GeV flares was described. This uses the GeV brightness as a proxy for VHE brightness. The extrapolation of GeV spectra to TeV energies with EBL extinction correction was found to be a reliable estimate for the true VHE brightness. Comparison

with archival non-simultaneous GeV-TeV data, as well as truly simultaneous data on two sources, PKS 2155-304 and 3C 66A demonstarted that within the uncertainties in the EBL level, this estimate is in overall agreement with the measured VHE spectra. The same is done in much more detail for PKS 1510-089 in chapter 5. For GeV spectra that show a clear break, as in the case of PKS 2155-304 this estimate is not expected to hold, and the same is demonstrated in this work. Using the GeV spectrum as the intrinsic source spectrum estimates for the z of a 4 blazars is made which do not have a secure z measurements. These should be considered as upper limits to the z, as the extrapolation from GeV to TeV is done assuming there is no break in the spectrum.

In chapter 5 the HESS observations of two blazars triggered from optical and GeV flares is reported. The observations on PKS 1510-089 was triggered the first time (in March 2009) from flares in both the GeV and optical wavebands, and on the second instance (April 2009) from a GeV flare. The data taken during these observations suffered from hardware problems and bad weather. The analysis of the data resulted in the VHE detection of this source during the 3-day period coinciding with the March'09 GeV flare. The analysis done using the *Heidelberg wobble-chain analysis* with *soft-cuts* gave a detection at a 4.8σ level. This detection was confirmed with a cross-check using the *model++* analysis which is known to have better background suppression resulting in better sensitivity, to yield a 8.5σ level detection. As is customary for cross-check analysis within the HESS collaboration, this cross-check was done by another member of the collaboration using a different analysis pipeline[1]. This corresponds to 7.9σ after taking *trial factors* into account. From the analysis done in this work a VHE spectra was constructed between 220 GeV and 320 GeV. Furthermore the FGST data on this source was analyzed, and the GeV spectrum was extracted. The March'09 GeV flare period FGST spectrum was roughly a factor 6 higher that the 14 month average FGST spectrum. The spectral shape for both the spectra was compatible within statistical errors. A powerlaw spectrum convolved with EBL extinction was used as a model for the entire γ-ray data (from 200 MeV till 320 GeV). Four different models corresponding to four different EBL models were fit to the γ-ray data, using a Markov-chain Monte Carlo code developed in this work. The likelihood ratio test showed that all four models fit the data to approximately the same goodness. This was because the errors on the VHE data is rather high due to photon counts, and all the models are constrained mostly from the GeV data which is free from EBL extinction, and hence identical for all fit-models. Constaints on the EBL level from a similar FGST-HESS combined data set (from a source at similar redshift) can only be possible is the source has a much harder spectra which would result in a VHE spectra that is more precise as well as covers a wider energy range.

In section 5.4 the analysis of the HESS data on 3C 279 is presented. Observations on this source was triggered in January'09 from a GeV flare, while it was also above the ATOM trigger threshold. The analysis of the January'09 data did not give a detection.

---

[1]The model++ cross-check was done by HESS member Mathieu deNaurois, *LPNHE, Paris*

Combining this data with the previously taken data on this source also did not result in a detection. Upperlimits on the VHE integral flux were given.

In the first part of chapter 6 various parametrization for the luminosity-function (LF), density evolution (DE) and intrinsic spectral index distribution (SID) for the parent sample from which the true VHE blazar sample could be derived, are checked. Monte Carlo simulations were done taking different forms for the LF, DE and SID to generate parent blazar samples. From these samples, the sub sample of sources that could be detected with current VHE instruments were extracted as the parent VHE blazar sample. This required a comparison of the EBL absorbed VHE spectra to the instrument sensitivity of the current instruments. The parent VHE samples that gave good coverage in the range of redshifts over which the true sources are distributed, and were also compatible with the true VHE sample implied that the corresponding parametrization of the LF, DE, and SID were indeed viable. Comparing the true VHE blazar sample to the synthetic parent VHE blazar sample led to the following conclusions. The lack of a spectral softening with increasing z in the observed sample is compatible with a parent sample that shows a clear softening - therefore a lack of spectral softening could be simply due to a selection effect. This selection effect comes into play since the detections resulted from observing only a carefully selected list of sources rather than a sky survey. Thus a spectral correlation with z, e.g. and progressively hardening SID with z, is not necessary to explain the observed trend. It is found that soft-LFs can be ruled out to be incompatible with observations, and no strong effect due to either a positive DE or no-DE can be distinguished.

In section 6.2 the sensitivity of the EBL extinction to the uncertainty in the cosmological parameters was examined. It was concluded that the uncertainty in the cosmological parametes is very small compared to the uncertainty on the EBL density. Therefore the effect of cosmological uncertainty in the EBL extinction can be neglected. In sections 6.3 it is found that even for low γ-ray energies of 0.4 TeV for sources at $z \approx 0.5$ or higher, the evolution of the EBL photon density with redshift has to be taken into account for calculating the extinction correctly. In section 6.4 it is shown that the systematic errors on fluxes measured with VHE instruments is also negligible compared to the uncertainty in the current understanding of the EBL modelling. Thus the VHE measurements and therefore the physical models of VHE emission of extragalactic sources at $z \gtrsim 0.3$ will be limited due to the current uncertainty in the EBL extinction.

7.2 Outlook

In this study it was found that even though a blazar at a high z of 0.36 was detected, no constraints on the EBL could be made, as this detection was almost at the sensitivity limit of HESS. The extremely soft spectra resulted in its detection in a very narrow VHE range, and the low photon numbers resulted in large errors on the spectrum. In section 7.2.1 I estimate which characteristics of future detectors would be most useful to get a better spectral measurement of distant blazars.

The possibility of have sky surveys with future instruments is discussed in section 7.2.2.

7.2.1 Probing EBL density and evolution with CTA

VHE flux of blazars at $z > 0.3$ will be substantially attenuated due to the EBL. Furthermore the steep energy dependence of the extinction, will make the spectrum very soft. VHE instruments currently have the best sensitivity at ~ 1 TeV, with a low energy threshold at ~ 100 GeV (except for MAGIC). To make precise spectral measurement of faint and soft spectrum from distant blazars, an increase in sensitivity as well as a reduction in the energy threshold will be helpful. While a greater sensitivity means shorter observations are necessary for detecting a given flux level, lower threshold would help extracting a spectra over a wider energy range. In the following exercise the overall improvement on the measured spectra, by an improvement on these two instrument characteristics is tested. The planned Cherenkov Telescope Array (CTA)Doro (2009); Martinez (2008) is used as a template for future experiments.

(1) For this exercise I first construct a synthetic intrinsic blazar spectra as follows. The synthetic spectra is made of three parts, covering three bands in energy - first part is below 0.5 TeV, second part is from 0.5 TeV till 1 TeV, and the last part is above 1 TeV. The individual parts and the normalization were chosen like so -

(i) For the highest energy part (> 1 TeV) - the actual VHE spectra of Mrk 421 measured with HESS, for a high state in 2004 Aharonian *et al.* (2005c) was adopted. This spectrum was corrected for the EBL absorption (using the EBL in Aharonian *et al.* (2006b)) to get the corresponding intrinsic spectra.

(ii) For the part form 0.5 TeV till 1 TeV, a powerlaw with $\Gamma = 2$ was chosen, and initially normalized to the Mrk 421 spectrum above at 1 TeV.

(iii) For the part below 0.5 TeV a powerlaw with slope $\Gamma = 1.57$ was taken (the average slope for this source from the 3EG catalog), and again initially normalized to the $\Gamma = 2$ powerlaw above at 0.5 TeV.

(2) To account for the facts that - the 2004 HESS measurements were one of the highest flux recorded for Mkn 421, and that the farthest blazar that has a measured spectrum is at $z \approx 0.25$, I adjusted the normalization of the spectral shape found above

in the following way. Assuming a source at $z = 0.5$ the new normalization was found such that - the energy times integral flux ($E \times F(> E)$) including the correction for EBL attenuation was at a level just detectable by the present generation of Cherenkov Instruments (see figure 7.2.1 for the EBL corrected, i.e. observed version of this, the red spectrum marked '$z = 0.5$, no evolution'). The EBL corrected version of this new normalization turned out to be approximately an order of magnitude fainter than the value in Aharonian *et al.* (2005c), corrected for the inverse square distance dependence of the flux and for the EBL correction, applied for a source at $z = 0.5$. This hypothetical spectra is used as a generic intrinsic blazar spectra, is made of bits that are from true measurements of a blazar (except for the middle part which is purely artificial, to get a smooth turn off between the 3EG value and the HESS spectrum) and scaled down in brightness.

(3) With the normalization fixed at this value, the corresponding spectrum taking EBL evolution into account was also obtained. For this a generic fudge factor was applied to the EBL optical depth calculation. Recall from section 2.4 that the comoving EBL photon density has a factor of $(1 + z')^3$. This was changed to $(1 + z')^{(3-f_{EVO})}$ with $f_{EVO} = 1.2$. This mimics the evolution in EBL density to a close approximation. This spectrum is labeled as '$z = 0.5$, evolution' in figure 7.2.1.

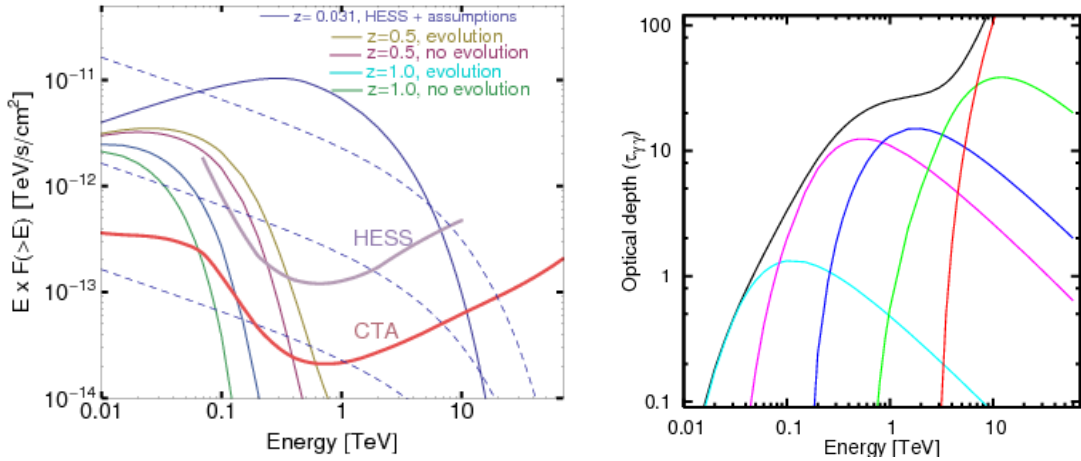(4) The exercise was repeated for $z = 1.0$, both with/without EBL-evolution.

Figure 7.1: **Left:** Synthetic spectra derived from actual measurements of Mkn 421, shown after EBL absorption at the redshift of Mkn 421 ($z = 0.031$), $z = 0.5$, and $z = 1$. Also shown are the approximate sensitivities of HESS and CTA. The dashed lines are, from top to bottom the 10%, 1% and 0.1% crab $E \times F(> E)$ values. **Right:** The optical depth for a source at $z = 1$, and the contributions of various wavebands of the EBL to the relevant γ-ray energy ranges. The black line is the total optical depth. The curves in cyan, magenta, blue, green, and red show the contribution to $\tau_{\gamma\gamma}$ from the EBL wavelength ranges between $0.1\mu m$ to $0.5\mu m$, $0.5\mu m$ to $2.5\mu m$, $2.5\mu m$ to $10\mu m$, $10\mu m$ to $50\mu m$, and $50\mu m$ to $250\mu m$ respectively.

Results and Discussion

It is clear (see figure 7.2.1) that the relevant energy range corresponds to the EBL in the range $0.1 \ \mu m \leqslant \lambda \leqslant 2.5 \ \mu m$. It should also be pointed out that the greater sensitivity envisaged for CTA at energies $\gtrsim 1 \ \text{TeV}$ will help to detect many more faint-blazars in the nearby universe. This would hopefully give us enough spectral measurements to study nearby blazars in more detail and give us enough statistics to answer questions about the intrinsic blazar spectra for at least the nearby ones that do not suffer much attenuation due to the EBL.

The situation for this hypothetical blazar at $z = 0.5$ measured with a current generation instrument like HESS, is clearly similar to the actual measurements obtained in this work on the quasar PKS 1510-089 - resulting in a spectrum that is only detected over a narrow energy range between $\gtrsim 100 \ \text{GeV}$ and $\approx 400 \ \text{GeV}$. The situation with CTA will be much better, since the larger sensitivity will result in a very precise measurement of the spectra. The lower energy threshold will also be vastly improved giving measurements over a wider range. The gain in the high energy is not substantial, since the spectrum decreases sharply with energy.

If this source were at $z = 1.0$, it will only be measurable with CTA - in the energy range $< \sim 0.2 \ \text{GeV}$. This is possible due to the greater overall sensitivity of CTA and its much lower energy threshold. It should be noted that the highest energy over which this source will be measured with CTA is much lower than the energy range over which it has the best sensitivity.

Thus for EBL studies what counts really is the lower energy threshold. The relevant EBL range is from $0.1 \mu m$ to $\sim 1 \mu m$, which is the range over which limits on the EBL level can be made.

7.2.2 Survey potential for next generation instruments

While current generation of instruments have clearly established the field and proved the techniques of IACT for VHE astronomy, their capabilities are limited due to a small field-of-view (FOV), and low sensitivity, which requires typically $\sim 50 \ \text{hours}$ of observation, to detect a single source. Exception to the second limitation exist e.g. PKS 2155-304, Mrk 421 and Mrk 501, which are perennially bright sources of VHE γ-rays; but source like 1ES 1101-232 and 3C 279, have eluded detection except during exceptionally bright flares. The small FOV and of present instruments combined with the requirement for deep observations, prevent IACT experiments from being able to operate in a scanning mode to do an all sky survey which is necessary for an unbiased population study, to observationally confirm the issues discussed in this work.

This would be a challenge to the planned next generation instruments, which are being designed to increase the sensitivity by at least an order of magnitude. These might operate in a survey mode. The increase in sensitivity is achieved with an increase in the

effective area of the instruments, which is achieved by distributing a number of medium-size ($\gtrsim 10\,\mathrm{m}$ primary) IACTs over a large surface area. To increase sensitivity to lower energies, the entire array can be subdivided into smaller sub-arrays with a central IACT with a large-size ($\gtrsim 25\,\mathrm{m}$ primary).

The cost and technical complications for increasing the FOV of individual instruments can be daunting, still, the future arrays can be operated in a scanning mode, by using special triggering electronics and observation strategies. For instance the electronic triggers could be designed, so that the sub-arrays of ~ 5 telescopes would have their own dedicated trigger mechanism, allowing them to act as independent array of IACTs that can be used for different pointings than the rest of the array. Multiple such sub-arrays can look at adjacent angular areas in the sky to cover roughly $n \times (f^\circ)^2$ angular area on the sky at the same time (where n is the number of sub-arrays, and f° is the FOV of each sub-array). This way a large effective FOV can be achieved that can be the operating mode for a part of the total observing time, and could be used to make a survey of portions of the sky if not the entire sky. Of course for making a whole sky survey two such complementary arrays would be required to be constructed in the northern and southern hemispheres.

Even with an increased sensitivities and an operating mode described above, to get a desired flux-limited sample of blazars, it might take a lot of observing hours. While it is necessary to get such a sample, and the scientific outcome would be well worth it; a *pseudo-survey* could alternatively be carried out to get a VHE-blazar sample, by pointed observations of a selection of candidate VHE blazars. This can be accomplished by starting out with a flux limited blazar sample in another waveband, e.g. a radio survey or an optical survey, and select all blazars in multiple patches in the sky of reasonable angular area. Such a selection of candidates for VHE observations would (almost always) be complete by virtue of the parent sample that was used, and selecting different regions of the sky would assure that the final results could be averaged and in principle be considered isotropic. These few regions could then be given deep pointed exposures of around $50\,\mathrm{hours}$ and an approximate (and fairly complete) VHE-flux limited sample could be constructed. This method can in fact, also be used by current generation of instruments, though it will yield far better results when performed with the planned future experiments like the CTA and AGIS (Buckley *et al.* 2008), using these observing strategy.

Overall, with the planned future generation of Cherenkov arrays, this field is set to take another quantum leap in unravelling the VHE universe as well as the EBL.

HESS *runs* on PKS 1510-089 and 3C 279

The columns are as follows - serial number, run number, number of telescopes participating in the run, the telescope pattern[1] identifying the telescopes in the run, the run start time, the duration of the run, and the event rate during the run.

Table A.1: **The HESS run log on PKS 1510-089.**

Sl.	Run	Tels.	Tel. Pattern	Start time (Date UT)	Duration (min.)	Event Rate (Hz)
1	50346	4	30	2009-03-20 23:11:51	28.1	153.8
2	50347	4	30	2009-03-20 23:42:27	12.3	161.5
3	50360	4	30	2009-03-21 23:01:15	28.1	152.2
4	50361	4	30	2009-03-21 23:31:34	28.1	167.0
5	50362	4	30	2009-03-22 00:01:53	28.1	186.8
6	50363	4	30	2009-03-22 00:32:22	28.1	192.9
7	50375	3	14	2009-03-22 23:01:27	4.6	118.7
8	50376	3	14	2009-03-22 23:13:26	28.1	122.4
9	50377	3	14	2009-03-22 23:43:59	28.1	122.8
10	50378	3	14	2009-03-23 00:14:11	28.1	129.1
11	50379	3	14	2009-03-23 00:44:20	28.1	134.7
12	50380	3	14	2009-03-23 01:14:30	28.1	131.0
13	50402	4	30	2009-03-24 00:54:38	3.1	56.4
14	50403	4	30	2009-03-24 01:54:28	28.1	195.2
15	50404	4	30	2009-03-24 02:24:46	22.1	191.6
16	50421	3	14	2009-03-25 00:33:26	28.1	110.7
17	50422	3	14	2009-03-25 01:03:47	10.2	81.0
18	50424	3	14	2009-03-25 02:44:26	9.1	81.5
19	50459	4	30	2009-03-26 00:57:20	28.1	158.4

---

[1]Each telescope is given identification as CT_i with the index running from 1 to 4. The pattern is defined as $\sum 2^i$, over all telescopes taking part in the run.

Table A.1 – . . . concluded from previous page, run log on PKS 1510-089

Sl.	Run	Tels.	Tel. Pattern	Start time (Date UT)	Duration (min.)	Event Rate (Hz)
20	50460	4	30	2009-03-26 01:27:34	28.1	161.1
21	50461	4	30	2009-03-26 01:57:57	28.1	160.9
22	50482	4	30	2009-03-27 01:11:58	28.1	179.6
23	50483	4	30	2009-03-27 01:42:31	28.1	182.7
24	50484	4	30	2009-03-27 02:12:50	28.1	183.2
25	50485	4	30	2009-03-27 02:45:06	28.1	181.7
26	50486	4	30	2009-03-27 03:15:31	28.1	172.8
27	50505	3	28	2009-03-28 00:12:40	28.2	124.7
28	50506	3	28	2009-03-28 00:43:01	0.2	166.5
29	50507	3	28	2009-03-28 01:27:37	0.9	125.6
30	50508	2	12	2009-03-28 01:37:14	28.1	79.0
31	50509	2	12	2009-03-28 02:07:30	28.1	79.2
32	50510	2	12	2009-03-28 02:37:54	28.1	77.0
33	50533	4	30	2009-03-29 00:38:13	28.1	74.2
34	50534	3	14	2009-03-29 01:20:33	28.1	83.9
35	50535	3	14	2009-03-29 01:50:54	28.1	82.2
36	50536	3	14	2009-03-29 02:24:33	28.1	86.6
37	50597	3	14	2009-04-01 00:03:50	28.1	122.7
38	50598	3	14	2009-04-01 00:34:15	28.1	124.6
39	50620	3	14	2009-04-02 00:31:10	28.1	121.8
40	50621	3	14	2009-04-02 01:01:36	11.0	122.1
41	51066	3	28	2009-04-27 22:52:31	28.1	131.6
42	51067	3	28	2009-04-27 23:22:43	28.1	132.2
43	51068	3	28	2009-04-27 23:52:53	28.1	132.9
44	51069	3	28	2009-04-28 00:23:12	28.1	131.6
45	51088	3	28	2009-04-28 22:34:28	28.1	129.3
46	51089	3	28	2009-04-28 23:04:48	28.1	130.4
47	51090	3	28	2009-04-28 23:35:03	28.1	127.7
48	51091	3	28	2009-04-29 00:05:36	28.1	130.6

All the HESS runs taken on 3C 279 are given in the table on the following page.

Table A.2: **The HESS run log on 3C 279.**

Sl.	Run	Tels.	Tel. Pattern	Start time (Date UT)	Duration (min.)	Event Rate (Hz)
1	36779	4	30	2007-01-18 02:10:53	28.1	236.3
2	36780	4	30	2007-01-18 02:41:03	16.7	248.1
3	36805	4	30	2007-01-19 02:23:33	28.1	249.1
4	36832	4	30	2007-01-20 02:18:45	10.7	237.8
5	36864	4	30	2007-01-21 02:10:40	28.1	242.5
6	36865	4	30	2007-01-21 02:41:01	19.5	255.0
7	44201	4	30	2008-02-05 02:13:48	28.1	198.0
8	49997	4	30	2009-01-24 00:56:14	28.1	165.1
9	49998	4	30	2009-01-24 01:27:27	28.1	182.8
10	49999	4	30	2009-01-24 01:59:27	28.1	191.3
11	50031	4	30	2009-01-26 01:55:13	0.6	32.2
12	50038	4	30	2009-01-27 02:36:48	28.1	205.4
13	50048	4	30	2009-01-28 01:34:00	2.6	131.7
14	50049	4	30	2009-01-28 02:12:09	28.1	201.3
15	50050	4	30	2009-01-28 02:42:29	25.7	205.4
16	50089	4	30	2009-01-30 01:04:47	28.1	176.7
17	50090	4	30	2009-01-30 01:35:10	3.9	154.3
18	50091	4	30	2009-01-30 02:20:30	3.1	195.2
19	50092	3	14	2009-01-30 02:29:39	2.7	126.6
20	50093	3	14	2009-01-30 02:38:24	22.2	134.2

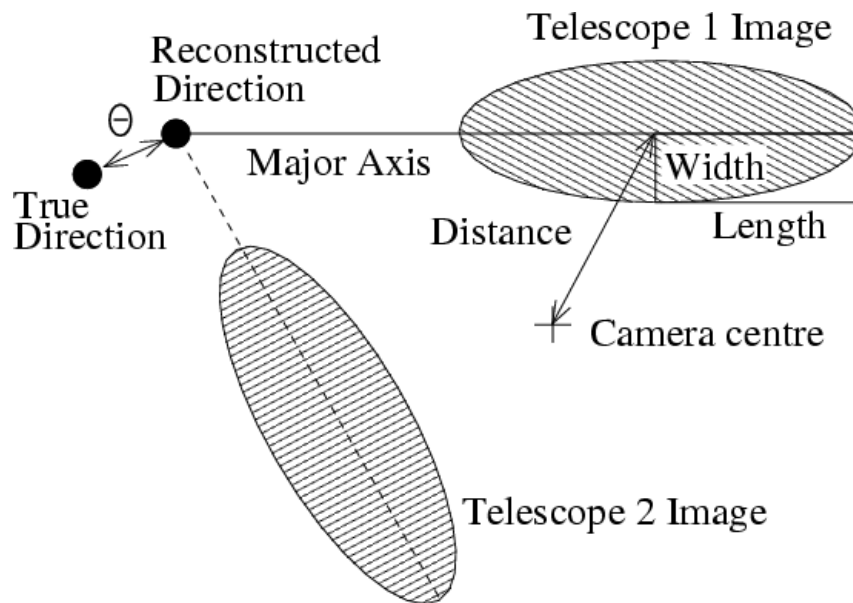# Hillas parameters and shape-cuts

Hillas Parameters

Figure B.1: The basic Hillas parameter illustrated on the camera plane.

Shape-cuts for γ-hadron discrimination

Table B.1: The four selection-cuts used for the hillas-style analysis of HESS data.

Cut type (name)	Optimization flux & Γ (crab-flux & phot-index)	Size max (p.e.)	θ^2_{cut} max (degrees^2)	MRSL max (σ)	MRSW max (σ)	Distance max (degrees)
soft	0.01 & 5.0	40	0.02	1.3	0.9	2.0
standard	0.1 & 2.6	80	0.0125	2.0	0.9	2.0
hard	0.01 & 2.0	200	0.01	2.0	0.7	2.0
loose	1 & 3.0	40	0.04	2.0	1.2	2.0

Energy resolution for soft-cuts

Soft-cuts are designed to give higher significances for soft spectrum sources. This is achieved with a lower *Size* cut that results in a lower energy threshold. The energy-resolution defined as $(E_r - E_t)/E_t$, where E_r is the reconstructed photon energy and E_t is the true photon energy. This parameter defines the systematic error on the energy reconstruction. The functional shape is shown here.
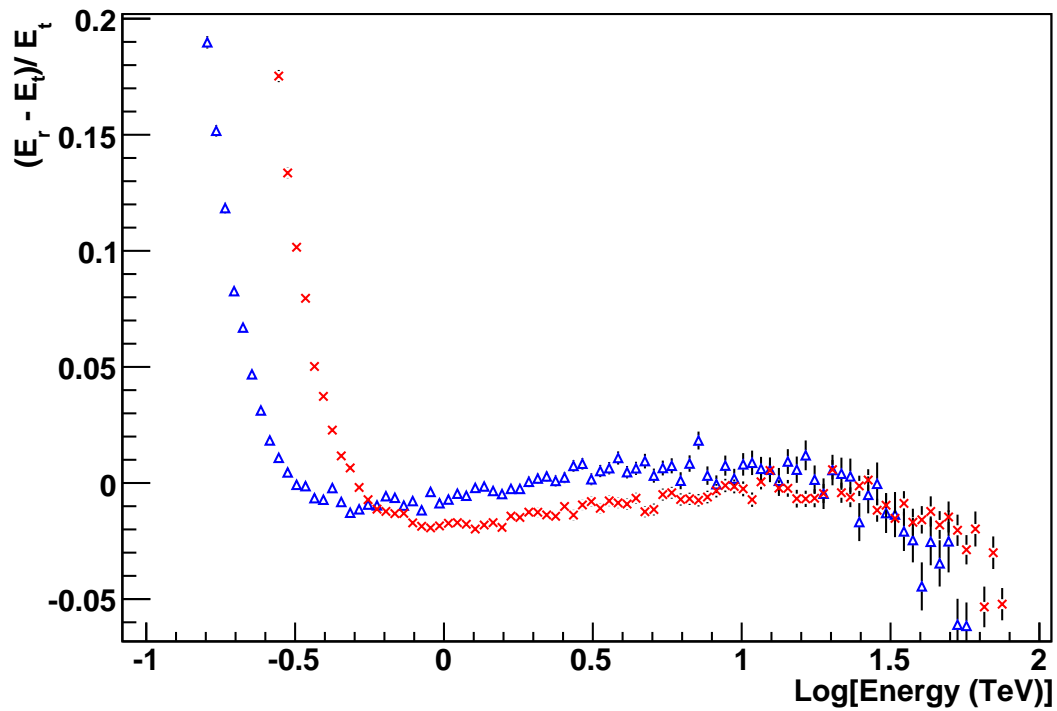
Figure B.2: The energy resolution versus energy, for soft-cuts ("soft_north_1b" configuration) for offset angle of 0.5°. Blue points are for 20° zenith angle and the red points are for 40° zenith angle.

Bibliography

Abdo, A. A., Ackermann, M., Ajello, M, *et al.* . 2009a. Bright AGN source list from the first three months of Fermi LAT all-sky survey. *ApJ*, **700**, 597.

Abdo, A. A., Ackermann, M., Ajello, M, *et al.* . 2009b. VERITAS Discovery of >200 GeV Gamma-Ray Emission from the Intermediate-Frequency-Peaked BL Lacertae Object W Comae. *PRL*, **102**, 181101.

Acciari, V. A., Aliu, E., Beilicke, M, *et al.* . 2008. VERITAS Discovery of >200 GeV Gamma-Ray Emission from the Intermediate-Frequency-Peaked BL Lacertae Object W Comae. *ApJ*, **684**, L73. (Ac08).

Acero, F., Aharonian, F., Akhperjanian, A. G., *et al.* . 2009. Detection of gamma rays from a starburst galaxy. *Science express*, **326**, 1080.

Aharonian, F., Akhperjanian, A., Barrio, J, *et al.* . 2001. The TEV Energy Spectrum of Markarian 501 Measured with the Stereoscopic Telescope System of HEGRA during 1998 and 1999. *ApJ*, **546**, 898. (Ah01).

Aharonian, F., Akhperjanian, A., Beilicke, M., *et al.* . 2002. Variations of the TeV energy spectrum at different flux levels of Mkn 421 observed with the HEGRA system of Cherenkov telescopes. *A&A*, **393**, 89. (Ah02).

Aharonian, F., Akhperjanian, A., Aye, K.-M., *et al.* . 2005a. Discovery of VHE gamma rays from PKS 2005-489. *A&A*, **436**, L17. (Ah05a).

Aharonian, F., Akhperjanian, A., Aye, K.-M., *et al.* . 2005b. H.E.S.S. observations of PKS 2155-304. *A&A*, **430**, 865. (Ah05b).

Aharonian, F., Akhperjanian, A., Aye, K.-M., *et al.* . 2005c. Observations of Mrk 421 with HESS at large zenith angles. *A&A*, **437**, 95.

Aharonian, F., Akhperjanian, A.G., Bazer-Bachi, A.R., *et al.* . 2006a. Evidence for VHE γ-ray emission from the distant BL Lac PG 1553+113. *A&A*, **448**, L19–L23.

Aharonian, F., Akhperjanian, A.G., Bazer-Bachi, A.R., *et al.* . 2006b. A low level of extragalactic background light as revealed by γ-rays from blazars. *Nat*, **440**, 1018. (Ah06b).

Aharonian, F., Akhperjanian, A. G., Bazer-Bachi, A. R., *et al.* . 2006c. Observation of the Crab nebula with H.E.S.S. *A&A*, **457**, 899.

Aharonian, F., Akhperjanian, A., Bazer-Bachi, A. R., *et al.* . 2007a. Detection of VHE gamma-ray emission from the distant blazar 1ES1101-232 with HESS and broadband characterisation. *A&A*, **470**, 475. (Ah07b).

Aharonian, F., Akhperjanian, A., Barres de Almeida, U., *et al.* . 2007b. Discovery of VHE -rays from the distant BL Lacertae 1ES 0347-121. *A&A*, **473**, L25. (Ah07c).

Aharonian, F., Akhperjanian, A. G., Barres de Almeida, U., *et al.* . 2007c. New constraints on the mid-IR EBL from the HESS discovery of VHE -rays from 1ES 0229+200. *A&A*, **475**, L9. (Ah07a).

Aharonian, F., Akhperjanian, A. G., Anton, G., *et al.* . 2009. Simultaneous observations of PKS 2155304 with HESS, Fermi, RXTE, and ATOM: spectral energy distributions and variability in a low state. *ApJ*, **696**, L150.

Aharonian, F. A. 2004. *Very high energy cosmic gamma radiation.* World Scientific.

Albert, J., Aliu, E., Anderhub, H., *et al.* . 2006a. Discovery of Very High Energy Gamma Rays from 1ES 1218+30.4. *ApJ*, **642**, L119. (Al06c).

Albert, J., Aliu, E., Anderhub, H., *et al.* . 2006b. Discovery of Very High Energy -Rays from Markarian 180 Triggered by an Optical Outburst. *ApJ*, **648**, L105. (Al06a).

Albert, J., Aliu, E., Anderhub, H., *et al.* . 2006c. Observation of Very High Energy Gamma-Ray Emission from the Active Galactic Nucleus 1ES 1959+650 Using the MAGIC Telescope. *ApJ*, **639**, 761. (Al06b).

Albert, J., Aliu, E., Anderhub, H., *et al.* . 2007a. Discovery of Very High Energy -Ray Emission from the Low-Frequency-peaked BL Lacertae Object BL Lacertae. *ApJ*, **666**, L17. (Al07b).

Albert, J., Aliu, E., Anderhub, H., *et al.* . 2007b. Discovery of Very High Energy -Rays from 1ES 1011+496 at z = 0.212. *ApJ*, **667**. (Al07c).

Albert, J., Aliu, E., Anderhub, H., *et al.* . 2007c. Observation of Very High Energy -Rays from the AGN 1ES 2344+514 in a Low Emission State with the MAGIC Telescope. *ApJ*, **662**, 892. (Al07a).

Albert, J., Aliu, E., Anderhub, H., *et al.* . 2008. Very-High-Energy Gamma Rays from a Distant Quasar: How Transparent Is the Universe? *Science*, **320**.

Beckmann, V., Engels, D., Bade, N., & Wucknitz, O. 2003. The HRX-BL Lac sample - Evolution of BL Lac objects. *A&A*, **401**, 927.

Behera, B., & Wagner, S. J. 2008. Catching blazars in the act! GLAST triggers for TeV observation of blazars. *AIPC*, **1085**. proceedings of "Heidelberg International Symposium on High Energy Gamma-Ray Astronomy", held in Heidelberg, 7-11 July 2008, submitted to AIP Conference Proceedings.

Bennett, A. S. 1962. The revised 3C catalogue of radio sources. *MmRAS*, **68**, 163B.

Berge, D., Funk, S., & Hinton, J. 2007. *A & A*, **466**, 1219.

Bertin, E., & Arnouts, S. 1996. *A & AS*, **117**, 393.

Bessel, M. S. 1990. UBVRI passband. *PASP*, **102**, 1181.

Blanch, O., & Martinez, M. 2005. *Astroparticle Physics*, **23**, 588, 598, 608.

Böttcher, M. 2005. A Hadronic Synchrotron Mirror Model for the "Orphan" TeV Flare in 1ES 1959+650. *ApJ*, **621**, 176.

Böttcher, M., Reimer, A., & Marscher, A. P. 2009. Implications of the very High Energy Gamma-Ray Detection of the Quasar 3C279. *ApJ*, **703**, 1168B.

Buckley, J., Coppi, P., Digel, S., *et al.* . 2008. The Advanced Gamma-ray Imaging System (AGIS)Science Highlights. *AIP Conf. Proc.*, **1085**. Proceedings of the 4th International Meeting on High Energy Gamma-Ray Astronom.

Casandjian, Jean-Marc, & Grenier, Isabelle A. 2008. A Revised Catalogue of EGRET Gamma-ray Sources. *A&A*, **489**, 849.

Ciprini, S., & the Fermi Large Area Telescope Collaboration. 2009. Fermi-LAT detection of another rapid GeV flare from the blazar PKS 1510-089. *ATel*, **1897**.

Ciprini, S., Chaty, S., & Fermi LAT collaboration. 2009. Fermi LAT detections of increasing gamma ray activity of blazar 3C 279. *ATel*, **1864**.

Coppi, P. S., & Blandford, R. D. 1990. Reaction rates and energy distributions for elementary processes in relativistic pair plasmas. *MNRAS*, **245**, 453.

Costamante, L., & Ghisellini, G. 2002. TeV candidate BL Lac objects. *A&A*, **384**, 56.

Cutini, S., Hays, E., & the Fermi Large Area Telescope Collaboration. 2009. *ATel*, **2033**.

D'Ammando, F., Bulgarelli, A., Vercellone, S., *et al.* . 2008. AGILE detection of a gamma-ray source coincident with Blazar PKS 1510-08. *ATel*, **1436**.

D'Ammando, F., Pucella, G., Raiteri, C. M., *et al.* . 2009a. AGILE detection of a rapid gamma-ray flare from the blazar PKS 1510-089 during the GASP-WEBT monitoring. *arXiv:0909.3484v1 [astro-ph.HE]*.

D'Ammando, F., Bulgarelli, A., Vercellone, S., *et al.* . 2009b. AGILE detection of the flaring gamma-ray blazar PKS 1510-089. *ATel*, **1957**.

de Naurois, M., & Rolland, L. 2009. A high performance likelihood reconstruction of gamma-rays for Imaging Atmospheric Cherenkov Telescopes. *Astroparticle Physics*, **32**, 231.

Dermer, C. D., & Schlickeiser, R. 1993. *ApJ*, **416**, 458.

Dermer, C. D., Sturner, S. J., & Schlickeiser, R. 1997. Nonthermal Compton and Synchrotron Processes in the Jets of Active Galactic Nuclei. *ApJS*, **109**, 103.

Doro, M. 2009. CTA - A Project for a New Generation of Cherenkov Telescopes. *arXiv:0908.1410v1 [astro-ph.IM]*.

Dwek, E., & Krennrich, F. 2005. Simultaneous constraints on the spectrum of the EBL and the intrinsic TeV spectra of Mrk 421, Mrk 501 and H1426+428. *ApJ*, **618**, 657.

Edge, D. O., Shakeshaft, J. R., McAdam, W. B., Baldwin, J. E., & Archer, S. 1959. A survey of radio sources at a frequency of 159 Mc/s. *MmRAS*, **68**, 37E.

Ekers, J. A. 1969. The Parkes catalogue of radio sources, declination zone +20 to -90. *AuJPAS*, **7**, 1E.

Elisa Prandini, Daniela Dorner, Nijil Mankuzhiyil, *et al.* . 2009. A new upper limit on the redshift of PG 1553+113 from observations with the MAGIC Telescope. *arXiv:0907.0157v1 [astro-ph.HE]*. Contribution to the 31st ICRC, Lodz, Poland, July 2009.

Elvis, M., Maccacaro, T., Wilson, A. S., *et al.* . 1978. Seyfert galaxies as X-ray sources. *MNRAS*, **183**, 129E.

Elvis, M, Wilkes, B. J., C., McDowell J., *et al.* . 1994. Atlas of quasar energy distribution. *ApJS*, **95**, 1.

Fegan, S. J., Sanchez, D., & Collaboration, Fermi LAT. 2009. Fermi observations of TeV-selected AGN. *arXiv:0910.4881v1 [astro-ph.HE]*.

Fermi, E. 1949. *Physical Review*, **75**, 1169.

Fossati, G., Maraschi, L., Celotti, A., Comastri, A., & Ghisellini, G. 1998. A unifying view of the spectral energy distributions of blazars. *MNRAS*, **299**, 433.

Fossati, G., Buckley, J. H., Bond, I. H., Bradbury, S. M., *et al.* . 2008. Multiwavelength Observations of Markarian 421 in 2001 March: An Unprecedented View on the X-Ray/TeV Correlated Variability. *ApJ*, **677**, 906.

Franceschini, A., Rodighiero, G., & Vaccari, M. 2008. Extragalactic optical-infrared background radiation, its time evolution and the cosmic photon-photon opacity. *A&A*, **487**, 837.

Ghisellini, G., Maraschi, L., & Dondi, L. 1996. Diagnostics of Inverse-Compton models for the -ray emission of 3C 279 and MKN 421. *A&AS*, **120**, 503.

Gilmore, R., Madau, P., Primack, J. R., *et al.* . 2009. GeV gamma-ray attenuation and the high redshift UV background. *MNRAS*, **399**, 1694.

Giommi, P., & Padovani, P. 1994. BL Lac Reunification. *MNRAS*, **268**, 61.

Gould, R. J., & Schréder, G. 1966. Opacity of the Universe to High-Energy Photons. *Phys. Rev. Lett.*, **16**, 252.

Hartman, R. C., Bertsch, D. L., Bloom, S. D., *et al.* . 1999. *ApJS*, **123**, 79.

Hasinger, G., Miyaji, T., & Schmidt, M. 2005. Luminosity-dependent evolution of soft X-ray selected AGN. New Chandra and XMM-Newton surveys. *A&A*, **441**, 417.

Hauser, M. G., & Dwek, E. 2001. The Cosmic Infrared Background: Measurements and Implications. *ARA&A*, **39**, 249.

Heitler, W. 1960. *The Quantum Theory of Radiation*. Oxford Press, London.

Hewitt, A., & Burbidge, G. 1993. **87**, 451.

Hinton, J. 2004. *New. Astron. Review*, **48**, 331.

Hofmann, W., Jung, I., Konopelko, A., *et al.* . 1999. Comparison of techniques to reconstruct VHE gamma-ray showers from multiple stereoscopic Cherenkov images. *Astropart. Phys.*, **12**, 135.

Hofmann, W. on behalf of the HESS collaboration, & Fegan, S. on behalf of the Fermi-LAT collaboration. 2009. H.E.S.S. and Fermi-LAT discovery of VHE and HE emission from blazar 1ES 0414+009. *The Astronomer's Telegram, #2293*.

Homan, D. C., Ojha, R., Wardle, J. F. C., *et al.* . 2001. *ApJ*, **549**, 840.

Homan, D. C., Wardle, J. F. C., Cheung, C. C., *et al.* . 2002. PKS 1510-089: A Head-On View Of A Relativistic Jet. *ApJ*, **580**, 742.

Horan, D., Badran, H. M., Bond, I. H., *et al.* . 2002. Detection of the BL Lacertae Object H1426+428 at TeV Gamma-Ray Energies. *ApJ*, **571**, 753. (Ho02).

Imran, A., & Krennrich, F. 2007. Detecting a unique EBL signature with TeV gamma rays. *arXiv:0708.3104v11*. Contribution to the 30st ICRC, Mexico, 2008.

Kneiske, T. M., Mannheim, K., & Hartmann, D. H. 2002. Implications of cosmological gamma-ray absorption. I. evolution of the metagalactic radiation field. *A&A*, **386**, 1.

Kneiske, T. M., Bretz, T., Mannheim, K., & Hartmann, D. H. 2004. Implications of cosmological gamma-ray absorption. II. Modification of gamma-ray spectra. *A&A*, **413**, 807.

Krawczynski, H. 2008. http://jelley.wustl.edu/multiwave/spectrum/.

Krawczynski, H., Hughes, S. B., Horan, D., *et al.* . 2004. Multiwavelength Observations of Strong Flares from the TeV Blazar 1ES 1959+650. *ApJ*, **601**, 151.

Krennrich, F., & VERITAS Collaboration. 2003. Hourly Spectral Variability of Mrk 421. *Under the auspices of the International Union of Pure and Applied Physics (IUPAP). Editors: T. Kajita, Y. Asaoka, A. Kawachi, Y. Matsubara and M. Sasaki, p.2603*, 2603. Proceedings of the 28th International Cosmic Ray Conference. July 31-August 7, 2003. Trukuba, Japan.

Krennrich, F., Bond, I. H., Bradbury, S. M., *et al.* . 2002. Discovery of Spectral Variability of Markarian 421 at TeV Energies. *ApJ*, **575**, L9.

Krimm, H. A., Barthelmy, S. D., Baumgartner, W., *et al.* . 2009. Swift/BAT detects a hard X-ray outburst from PKS 1510-089. *ATel*, **1963**.

Larionov, V. M., Villata, M., Raiteri, C. M., *et al.* . 2009. Optical historical maximum of the blazar PKS 1510-08 observed by the GASP. *ATel*, **1990**.

Lemoine-Goumard, M., Degrange, B., & Tluczykont, M. 2006. Selection and 3D-Reconstruction of Gamma-Ray-induced Air Showers with a Stereoscopic System of Atmospheric Cherenkov Telescopes. *Astropart. Phys.*, **85**, 195.

Li, T.-P., & Ma, Y.-Q. 1983. *ApJ*, **272**, 317.

Malkan, M. A., & Stecker, F. W. 1998. *ApJ*, **496**, 13.

Mannheim, K. 1993. *A&A*, **269**, 67.

Mannheim, K., & Biermann, P. L. 1992. Gamma-ray flaring of 3C 279 - A proton-initiated cascade in the jet? *A&A*, **253L**, 21.

Mannheim, K., Biermann, P. L., & Kruells, W. M. 1991. A novel mechanism for nonthermal X-ray emission. *A&A*, **251**, 723.

Maraschi, L., Ghisellini, G., & Celotti, A. 1992. *ApJ*, **397**, L5.

Martinez, M. 2008. Towards the ground-based gamma-ray observatory CTA. *AIP Conf. Proc.*, **1085**. Proceedings of the 4th International Meeting on High Energy Gamma-Ray Astronom.

Mastichiadis, A., & Kirk, J. G. 1997. Variability in the synchrotron self-Compton model of blazar emission. *A&A*, **320**, 19.

Mattox, J. R., Hartman, R. C., & Reimer, O. 2001. A quantitative evaluation of potential radio identifications for 3EG EGRET sources. *ApJS*, **135**, 155.

Matute, I., LaFranca, F., Pozzi, F., *et al.* . 2006. Active galactic nuclei in the mid-IR. Evolution and contribution to the cosmic infrared background. *A&A*, **451**, 443.

Mazin, D., & Raue, M. 2007. *A&A*, **471**, 439.

Mazin, D., Lindfors, E., Berger, K., *et al.* . 2009. Discovery of Very High Energy gamma-rays from the blazar S5 0716+714. *arXiv:0907.0366v1 [astro-ph.CO]*. Contribution to the 31st ICRC, Lodz, Poland, July 2009.

Mink, D.J. 2005. *ADASS XV*.

Mücke, A., & Protheroe, R. J. 2001. *Astroparticle Physics*, **15**, 121.

Mücke, A., Protheroe, R. J., Engel, R., Rachen, J. P., & Stanev, T. 2003. BL Lac objects in the synchrotron proton blazar model. *Astroparticle Physics*, **18**, 593.

Nandikotkur, G., Jahoda, K. M., Hartman, R. C., *et al.* . 2007. *ApJ*, **657**, 706.

Nikishov, A. I. 1962. *Sov. Phys. J. Exp. Theor. Phys.*, **14**, 393.

of VHE -rays from the high-frequency-peaked BL Lacertae object RGB J0152+017, Discovery. 2008. Aharonian, F. and Akhperjanian, A. G. and Barres de Almeida, U. and others. *A&A*, **481**, L103. (Ah08).

Ohm, Stefan, van Eldik, Christopher, & Egberts, Kathrin. 2009. Gamma-Hadron Separation in Very-High-Energy gamma-ray astronomy using a multivariate analysis method. *Astroparticle Physics*, **31**, 383.

Ong, Rene A., & the VERITAS Collaboration. 2009a. Discovery of VHE Gamma-Ray Emission from the Fermi-LAT Source 1ES 0502+675. *The Astronomer's Telegram, #2301*. Rene A. Ong (UCLA) for the VERITAS Collaboration.

Ong, Rene A., & the VERITAS Collaboration. 2009b. Discovery of VHE Gamma-Ray Emission from the Fermi-LAT Source PKS 1424+240. *The Astronomer's Telegram, #2084*. Rene A. Ong (UCLA) for the VERITAS Collaboration.

Padovani, P., Giommi, P., Landt, H., & Perlman, E. S. 2007. The Deep X-Ray Radio Blazar Survey. III. Radio Number Counts, Evolutionary Properties, and Luminosity Function of Blazars. *ApJ*, **662**, 182.

Persic, M., & de Angelis, A. 2008. Intergalactic absorption and blazar -ray spectra. *A&A*, **483**, 1.

Pohl, M., & Schlickeiser, R. 2000. *A&A*, **354**, 395.

Primack, J. R., Bullock, J. S., & Somerville, R. S. 2001. Probing galaxy formation with high energy gamma-rays. *AIP Conf. Proc.*, **558**, 463. High Energy Gamma-Ray Astronomy.

Primack, J. R., Bullock, J. S., & Somerville, R. S. 2005. Observational Gamma-ray Cosmology. *AIP Conf. Proc.*, **745**, 23. 2nd International Symposium on High Energy Gamma-Ray Astronomy.

Pucella, G., D'Ammando, F., Tavani, M., *et al.* . 2009. AGILE detection of a persistent and very intense gamma-ray flaring state of the blazar PKS 1510-089. *ATel*, **1968**.

Rector, T. A., Stocke, J. T., Perlman, E. S., *et al.* . 2000. The Properties of the X-Ray-selected EMSS Sample of BL Lacertae Objects. *Astronmical Journal*, **120**, 1626.

Reimer, A., Böttcher, M., & Postnikov, S. 2005. Neutrino Emission in the Hadronic Synchrotron Mirror Model: The "Orphan" TeV Flare from 1ES 1959+650. *ApJ*, **630**, 186.

Reyes, L. C. 2009. *arXiv:0907.5175v1 [astro-ph.HE]*. Proceedings of the 31st International Cosmic Ray Conference, Lodz, July 7-15 2009.

Rieger, F. M., & Duffy, P. 2004. *ApJ*, **617**, 155.

Rieger, F. M., Bosch-Ramon, V., & Duffy, P. 2007. *Ap&SS*, **309**, 119.

Salamon, M. H., & Stecker, F. W. 1998. Absorption of High-Energy Gamma Rays by Interactions with Extragalactic Starlight Photons at High Redshifts and the High-Energy Gamma-Ray Background. *ApJ*, **493**, 547.

Schmidt, M. 1963. 3C 273 : A Star-Like Object with Large Red-Shift. *Nature*, **197**, 1040S.

Seyfert, Carl K. 1943. Nuclear Emission in Spiral Nebulae. *ApJ*, **97**, 28S.

Shu., Frank H. 1991. *The physics of Astrophysics - Volume I, Radiation.* University Science books, Mill valley, California.

Sikora, M., Begelman, M. C., & Rees, M. J. 1994. Nuclear Emission in Spiral Nebulae. *ApJ*, **421**, 153.

Stecker, F. W. 1969. The Cosmic Gamma-Ray Spectrum from Secondary-Particle Production in the Metagalaxy. *ApJ*, **157**, 507.

Stecker, F. W., de Jager, O. C., & Salamon, M. H. 1992. *ApJ*, **390**, L49.

Stecker, F. W., Malkan, M. A., & Scully, S. T. 2006. Intergalactic Photon Spectra from the Far-IR to the UV Lyman Limit for $0 < z < 6$ and the Optical Depth of the Universe to High-Energy Gamma Rays. *ApJ*, **648**, 774.

Stern, B. E., & Poutanen, J. 2008. *MNRAS*, **383**, 1695.

Stickel, M., Fried, J. W., Kuehr, H., Padovani, P., & Urry, C. M. 1991. The complete sample of 1 Jansky BL Lacertae objects. I - Summary properties. *ApJ*, **374**, 431.

Stockman, H. S., Moore, R. L., & Angel, J. R. P. 1984. The complete sample of 1 Jansky BL Lacertae objects. I - Summary properties. *ApJ*, **279**, 485.

Tavecchio, Fabrizio, Maraschi, Laura, & Ghisellini, Gabriele. 1998. Constraints on the physical parameters of TeV blazars. *ApJ*, **509**, 608.

Teshima, M. 2009. MAGIC observes very high energy gamma ray emission from PKS 1424 +240. *The Astronomer's Telegram, #2098*.

Teshima, M., Prandini, E., Bock, R., *et al.* . 2007. Discovery of Very High Energy Gamma-Rays from the Distant Flat Spectrum Radio Quasar 3C 279 with the MAGIC Telescope. *arXiv:0709.1475v1 [astro-ph].* proceedings of the 30th International Cosmic Ray Conference, Merida, July 2007.

Tramacere, Andrea, & the Fermi Large Area Telescope Collaboration. 2008. Fermi LAT observations of the PKS 1510-089 outburst. *ATel*, **1743**.

Ueda, Y., Akiyama, M., Ohta, K., & Miyaji, T. 2003. Cosmological Evolution of the Hard X-Ray Active Galactic Nucleus Luminosity Function and the Origin of the Hard X-Ray Background. *ApJ*, **598**, 886.

Urry, C. Megan, & Padovani, Paolo. 1995. Unified schemes for radio-loud AGN. *PASP*, **107**, 803.

Vercellone, S., D'Ammando, F., Pucella, G., Tavani, M., *et al.* . 2009. AGILE detection of a persistent and very intense gamma-ray flaring state of the blazar PKS 1510-089. *ATel*, **1976**.

Veron-Cetty, M. P., & Veron, P. 2006. Quasars and Active Galactic Nuclei (12th Ed.). *A&A*, **455**, 773.

Villata, M., Raiteri, C. M., Larionov, V. M., *et al.* . 2009. Optical and near-IR brightening of the blazar PKS 1510-08 observed by the GASP. *ATel*, **1988**.

Wagner, R., *et al.* . 2008. Scientific Highlights from Observations of Active Galactic Nuclei with the MAGIC Telescope. proceedings of "Heidelberg International Symposium on High Energy Gamma-Ray Astronomy", held in Heidelberg, 7-11 July 2008, submitted to AIP Conference Proceedings.

Wagner, S. J. 2006. Fast flares of blazars during gamma-ray observations. Optical - gamma-ray correlations. *A&AS*, **120**, 495.

Wagner, S. J., & Witzel, A. 1995. Intraday variability in quasars and BL Lac objects. *Annu. Rev. Astron. Asrophys.*, **33**, 163.

Zacharias, ., *et al.* . 2004. *AJ*, **127**, 3043.

Acknowledgments